UNIVERSIDAD DE CHILE
FACULTAD DE CIENCIAS FÍSICAS Y MATEMÁTICAS
DEPARTAMENTO DE INGENIERÍA ELÉCTRICA

PERFORMANCE ANALYSIS OF THE WEIGHTED LEAST-SQUARES AND MAXIMUM LIKELIHOOD ESTIMATORS IN THE JOINT ESTIMATION OF SOURCE FLUX AND BACKGROUND

TESIS PARA OPTAR AL GRADO DE
MAGÍSTER EN CIENCIAS DE LA INGENIERÍA, MENCIÓN ELÉCTRICA

MEMORIA PARA OPTAR AL TÍTULO DE
INGENIERO CIVIL ELÉCTRICO

MARIO LORENZO VICUÑA ÁLVAREZ

PROFESOR GUÍA:
JORGE SILVA SÁNCHEZ

PROFESOR CO-GUÍA:
RENÉ MÉNDEZ BUSSARD

MIEMBROS DE LA COMISIÓN:
MARCOS ORCHARD CONCHA
FRANCISCO FÖRSTER BURÓN

SANTIAGO DE CHILE
2022

RESUMEN
TESIS PARA OPTAR AL GRADO DE
MAGÍSTER EN CIENCIAS DE LA INGENIERÍA ELÉCTRICA
MEMORIA PARA OPTAR AL TÍTULO DE
INGENIERO CIVIL ELÉCTRICO
POR: MARIO LORENZO VICUÑA ÁLVAREZ
FECHA: 2022
PROF. GUÍA: JORGE SILVA SÁNCHEZ
PROF. CO-GUÍA: RENÉ MÉNDEZ BUSSARD

ANÁLISIS DE DESEMPEÑO DE LOS ESTIMADORES MÍNIMOS CUADRADOS PONDERADOS Y MÁXIMA VEROSIMILITUD PARA LA ESTIMACIÓN CONJUNTA DE FLUJO Y RUIDO CELESTE

El presente trabajo de tesis estudia los posibles beneficios de realizar inferencia simultánea al estimar el brillo de una fuente puntual en el cielo y el ruido de fondo que rodea dicha señal, y cómo este esquema de estimación conjunta se ve fortalecido al incluir tanta información como sea posible, en forma de pixeles de una imagen. La primera parte de este análisis se sustenta en límites fundamentales formulados en teoría de estimación paramétrica, la clásica Cota de Cramér-Rao, para mostrar cómo el uso de información permite, hasta cierto punto, el desacople de los estimados, lo que conlleva posibles niveles de precisión comparables al caso de inferir cada parámetro de manera separada, con conocimiento del otro. Este comportamiento es presentado a lo largo de un amplio rango de condiciones observacionales y objetos diferentes.

Para la segunda parte the este trabajo se extienden resultados previos sobre estimadores implícitos, desarrollando un marco matemático que permite acotar los momentos de estimadores multidimensionles definidos implícitamente mediante algún problema de optimización. Diferentes formas y variantes del estimador de Mínimos Cuadrados Ponderados se desarrollan y emplean para validar estos resultados matemáticos, los cuales permiten mostrar que el desempeño del estimador de Máxima Verosimilitud se aproxima estrechamente a los límites fundamentales de precisión, de manera consistente. Además, se explora el uso potencial de estos resultados como método de validación para la implementación de algoritmos de estimación.

RESUMEN
TESIS PARA OPTAR AL GRADO DE
MAGÍSTER EN CIENCIAS DE LA INGENIERÍA ELÉCTRICA
MEMORIA PARA OPTAR AL TÍTULO DE
INGENIERO CIVIL ELÉCTRICO
POR: MARIO LORENZO VICUÑA ÁLVAREZ
FECHA: 2022
PROF. GUÍA: JORGE SILVA SÁNCHEZ
PROF. CO-GUÍA: RENÉ MÉNDEZ BUSSARD

PERFORMANCE ANALYSIS OF THE WEIGHTED LEAST-SQUARES AND MAXIMUM LIKELIHOOD ESTIMATORS IN THE JOINT ESTIMATION OF SOURCE FLUX AND BACKGROUND

This thesis studies the possible benefits of simultaneous inference when estimating the brightness of a point source in the sky and the background that the signal is embedded into, and how this joint estimation scheme is empowered by including as much information, in the form of image pixels, as possible. The first part of this analysis resorts to fundamental limits of parametric estimation theory, the classic Cramér-Rao Bound, to show how the incorporation of information allows the estimates to decouple from each other to some extent, leading to precision levels comparable of those of separate inference of one quantity with knowledge of the other. Such behavior emerges for a wide range of observational configurations and objects.

For the second part of the thesis, previous work on implicit estimators is extended as a new mathematical framework to allow bounding the momenta of multidimensional estimators defined implicitly through some optimization problem. Different flavors of the Weighted Least-Squares estimator allow us to validate these mathematical tools, which are then employed to show that the Maximum Likelihood estimator approaches the fundamental precision limits tightly and consistently. Moreover, potential use of these mathematical tools as a mean for validation of the implementation of an estimation algorithm is explored.

Para mi familia, Balto y Amaru

Agradecimientos

Es menester agradecer antes que a nadie más a mis padres, sin quienes no solo esta tesis no hubiera sido posible, sino que toda mi formación escolar, profesional y personal, cuanto menos. Toda su labor y apoyo como padres ha definido en gran medida mi estructura valórica y posibilitado un montón de oportunidades, entre las cuales quisiera destacar ante todo la educación y a valorarla en todo su espectro, sobretodo el humano.

Lo anterior me gustaría extenderlo también a mis abuelos, quienes hicieron lo mismo por sus hijos. Aprovecho también de agradecer a mi tío Lorenzo a quien esta instancia lo hace tan orgulloso como a mis papás.

Siguiendo con la familia no podía dejar fuera a mi hermana Fran, que tuvo que sufrir mis infinitas verborreas beauchefianas más que nadie, además de ofrecer esa complicidad de hermanos, en especial en estos últimos años.

Agradezco también a los miembros del IDS. A los profesores Jorge, Marcos y René por la oportunidad de esta experiencia formativa (irónicamente tan íntimamente relacionada a la astronomía), compartir sus singulares experiencias, perspectivas y consejos; y sobretodo por su paciencia. A mis compañeros Mauricio, Don Tapir, y Sebi y Miguel, con quienes incluso desde el día uno en la facultad tuve el (a veces dudoso) honor de compartir paso por esta facultad.

A las tertulias, amigos que aún frente a los años o la inmensa distancia han mantenido sus brazos abiertos. Kudos para César-sama, Pepe, Abarca, Nachín, Thomas, Beto y Furanky.

De la misma manera, no puedo olvidar mencionar a otros compañeros de carrera, como los *brrxitos* y los de "*lisensiatura*", con quienes compartí mera erudición, buenas comidas, buenas cervezas y terribles "noches" de Terraria.

Quería también hacer una mención especial a la Frau Pascale y al Herr Zúñiga.

Y en general, a todas las personas que apararecen o podrían haber aparecido en estos agradecimientos por su indiscutible pero tácita huella en mi educación: *gracias por tanto, perdón por tan poco.*

Table of Contents

List of Tables **vii**

List of Figures **viii**

1 Introduction **1**
1.1 Motivation . . . 1
1.2 Assumptions . . . 2
1.3 Objectives . . . 2
1.3.1 Main Objectives . . . 2
1.3.2 Specific Objectives . . . 2
1.4 Structure . . . 3

List of Acronyms **4**

2 Preliminaries and Background **6**
2.1 The Joint Source Flux and Background Estimation Problem . . . 6
2.2 The Cramér-Rao Lower Bound . . . 8
2.3 Sufficient Statistics . . . 10
2.4 Related Work . . . 11

3 Finding Performance Bounds for high-dimensional Implicit Estimators **13**

4 Cramér-Rao Lower Bound for Joint Source Flux and Background Estimation **17**
4.1 The Cramér-Rao Bounds under different Pixel Selection Schemes . . . 20
4.2 Effect of Device Resolution on Cramér-Rao Lower Bounds . . . 26
4.3 MVUE and its Achievability . . . 30

5 WLS Estimator for Joint Source Flux and Background Estimation **34**
5.1 Numerical Analysis . . . 35
5.1.1 Effect of Weight Selection . . . 35
5.1.2 Aperture Analysis . . . 43
5.1.3 Further Remarks . . . 47
5.2 Bounding the Performance of the SWLS Estimator . . . 50
5.2.1 SWLS as a non-linear Estimator . . . 51
5.2.2 Numerical Analysis . . . 52

6 ML Estimator for Joint Source Flux and Background Estimation **56**
6.1 Numerical Analysis . . . 57
6.1.1 Bias Bounds . . . 57
6.1.2 Variance Bounds . . . 58
6.1.3 Empirical Performance . . . 60
6.2 Using the Bounds as an Implementation-Validation Tool . . . 63

7 Conclusions and Future Work **65**

Bibliography **68**

Annex A Proof: Bounding the Performance of a high-dimensional Implicit Estimator **71**
A.1 Bias Bounds . . . 73
A.2 Variance Bounds . . . 74
A.3 First- and Second-Order Derivatives for τ_J . . . 75

Annex B Proof: Cramér-Rao Lower Bounds for the Joint Estimation Problem of Flux and Background **81**

Annex C Proof: WLS Estimator for the Joint Estimation Problem of Flux and Background **85**

Annex D Proof: Theoretic Bounds for the SWLS Estimator in the Joint Estimation of Flux and Background **91**

Annex E Proof: Theoretic Bounds for the ML Estimator in the Joint Estimation of Flux and Background **97**

List of Tables

7.1 Main conclusions per chapter. 67

List of Figures

4.1 Quantified PSF, $g_i(x_c)$, and its permutation, which is employed for the random selection scheme. . . . 20
4.2 Fisher matrix elements and its determinant for different selection schemes. . . . 21
4.3 Performance bounds for joint source flux and background estimation under different pixel selection schemes. For the upper-left and -right graphics, a solid line is used for the bounds for the joint estimation problem, σ_m^2 and $\sigma_{\tilde{B}}^2$, and a dashed line for the corresponding one-dimensional bounds, $\sigma_{m,1D}^2$ and $\sigma_{\tilde{B},1D}$. The black dashed line on the lower-left and -right graphics indicates a 5% discrepancy. . . . 23
4.4 Off-diagonal element of $I_{\boldsymbol{\theta}}^{-1}$ for different selections schemes. . . . 25
4.5 SNR for different selection schemes as more pixels are included. . . . 25
4.6 Performance bounds (top) and discrepancies (bottom) for joint source flux and background estimation for different observational scenarios, under an aperture pixel selection scheme. . . . 26
4.7 Off-diagonal element of $\mathcal{I}_{\boldsymbol{\theta}}^{-1}$ for different observational scenarios, under an aperture pixel selection scheme. . . . 26
4.8 SNR for different observational scenarios, under an aperture pixel selection scheme. 27
4.9 Performance bounds (top) and discrepancies (bottom) for joint source flux and background estimation for different centering configurations, as functions of pixel size Δx. . . . 28
4.10 Off-diagonal element of $\mathcal{I}_{\boldsymbol{\theta}}^{-1}$ for different centering configurations, as a function of pixel size Δx. . . . 28
4.11 Performance bounds (top) and discrepancies (bottom) for joint source flux and background estimation for different centering configurations, as functions of pixel size Δx, $FWHM = 0.5''$. . . . 29
4.12 Performance bounds (top) and discrepancies (bottom) for joint source flux and background estimation for different centering configurations, as functions of pixel size Δx, $FWHM = 1.5''$. . . . 30
4.13 Performance bounds (top) and discrepancies (bottom) for joint source flux and background estimation for different source brightness, as functions of pixel size Δx. 30
4.14 Off-diagonal element of $\mathcal{I}_{\boldsymbol{\theta}}^{-1}$ for different source brightness, as a function of pixel size Δx. . . . 31
4.15 Performance bounds (top) and discrepancies (bottom) for joint source flux and background estimation for different sky conditions, as functions of pixel size Δx. . . 31
4.16 Off-diagonal element of $\mathcal{I}_{\boldsymbol{\theta}}^{-1}$ for different sky conditions, as a function of pixel size Δx. . . . 32

5.1 Performance discrepancies, as functions of pixel size Δx, for joint source flux and background estimation corresponding to the Least-Squares estimator for different source brightness. . . . 36
5.2 Relative biases, as functions of pixel size Δx, for joint source flux and background estimation corresponding to the Least-Squares estimator for different source brightness. . . . 37
5.3 Performance discrepancies, as functions of pixel size Δx, for joint source flux and background estimation corresponding to the Weighted Least-Squares estimator with weights chosen over the grid $\mathcal{G}_{\tilde{F}}$, for $\tilde{F} = 1080$ photo-e$^-$. . . . 37
5.4 Performance discrepancies, as functions of pixel size Δx, for joint source flux and background estimation corresponding to the Weighted Least-Squares estimator with weights chosen over the grid $\mathcal{G}_{\tilde{F}}$, for $\tilde{F} = 20004$ photo-e$^-$. . . . 38
5.5 Performance discrepancies, as functions of pixel size Δx, for joint source flux and background estimation corresponding to the Weighted Least-Squares estimator with weights chosen such that $\tilde{f} = c \cdot \tilde{F}, c > 0.$, for $\tilde{F} = 1080$ photo-e$^-$. . . . 38
5.6 Performance discrepancies, as functions of pixel size Δx, for joint source flux and background estimation corresponding to the Weighted Least-Squares estimator with weights chosen such that $\tilde{f} = c \cdot \tilde{F}, c > 0.$, for $\tilde{F} = 20004$ photo-e$^-$. . . . 39
5.7 Performance discrepancies, as functions of pixel size Δx, for joint source flux and background estimation corresponding to the Weighted Least-Squares estimator with weights chosen over the grid $\mathcal{G}_{\tilde{B}}$, for $\tilde{F} = 1080$ photo-e$^-$. . . . 39
5.8 Performance discrepancies, as functions of pixel size Δx, for joint source flux and background estimation corresponding to the Weighted Least-Squares estimator with weights chosen over the grid $\mathcal{G}_{\tilde{B}}$, for $\tilde{F} = 20004$ photo-e$^-$. . . . 40
5.9 Performance discrepancies, as functions of pixel size Δx, for joint source flux and background estimation corresponding to the Weighted Least-Squares estimator with weights chosen such that $\tilde{b} = c \cdot \tilde{B}, c > 0.$, for $\tilde{F} = 1080$ photo-e$^-$. . . . 40
5.10 Performance discrepancies, as functions of pixel size Δx, for joint source flux and background estimation corresponding to the Weighted Least-Squares estimator with weights chosen such that $\tilde{b} = c \cdot \tilde{B}, c > 0.$, for $\tilde{F} = 20004$ photo-e$^-$. . . . 41
5.11 Performance comparison between LS estimator and UWLS estimator for different source brightness. $FWHM = 0.5$ arcsec. . . . 41
5.12 Performance comparison between LS estimator and UWLS estimator for different source brightness. $FWHM = 1.5$ arcsec. . . . 41
5.13 Performance discrepancies, as functions of pixel size Δx, for joint source flux and background estimation corresponding to adaptive versions of the WLS estimator for different source brightness. . . . 43
5.14 Relative biases, as functions of pixel size Δx, for joint source flux and background estimation corresponding to adaptive versions of the WLS estimator for different source brightness. . . . 43
5.15 Relative biases for different apertures corresponding to the adaptive WLS estimators for different source brightness. . . . 45
5.16 Performance discrepancies for different apertures corresponding to the adaptive WLS estimators for different source brightness. . . . 45
5.17 Performance discrepancies with respect to σ_m^{max} (left) and $\sigma_{\tilde{B}}^{max}$ (right) for different apertures corresponding to the adaptive WLS estimators for different source brightness. . . . 45

5.18 Covariances of the SWLS and IWLS estimators and their comparison with their Cramér-Rao counterpart, under different apertures and source brightness. 46
5.19 Performance discrepancies with respect to σ_m^{max} (left) and $\sigma_{\tilde{B}}^{max}$ (right) for different apertures corresponding to the adaptive WLS estimators for different sources with $FWHM = 0.5$ [arcsec]. 47
5.20 Performance discrepancies with respect to σ_m^{max} (left) and $\sigma_{\tilde{B}}^{max}$ (right) for different apertures corresponding to the adaptive WLS estimators for different sources with $FWHM = 1.5$ [arcsec]. 47
5.21 Relative biases obtained by adaptive WLS estimators for different sources with $FWHM = 0.5$ [arcsec]. 48
5.22 Relative biases obtained by adaptive WLS estimators for different sources with $FWHM = 1.0$ [arcsec]. 49
5.23 Relative biases obtained by adaptive WLS estimators for different sources with $FWHM = 1.5$ [arcsec]. 49
5.24 Performance discrepancies obtained by adaptive WLS estimators for different sources with $FWHM = 0.5$ [arcsec]. 50
5.25 Bias bounds for joint source flux (left) and background (right) estimation under different observational scenarios, for an aperture selection scheme. 52
5.26 Variance bounds for joint source flux (left) and background (right) estimation for the considered base case, under an aperture selection scheme. 53
5.27 Performance discrepancies of the SWLS estimator for joint source flux (left) and background (right) estimation for different observational scenarios, under an aperture selection scheme. Dashed-dotted-, dashed- and solid lines denote the lower bound, the upper bound and the empirical variance estimate, respectively. 53
5.28 SWLS estimates distribution for the baseline scenario using different aperture diameters. Blue markers denote the pairs $(\hat{\tilde{F}}, \hat{\tilde{B}})$, orange marker is used for the ground truth value and green marker denotes the sample means. On the bottom-left corner of each graph the sample Pearson correlation coefficient is displayed. Estimates in each graph are obtained from the same sample set. 54

6.1 Bias bounds for joint source flux (left) and background (right) estimation for different observational scenarios, under an aperture selection scheme. 58
6.2 Performance discrepancies between $\sigma^2_{ML,\tilde{F}}$ (left), $\sigma^2_{ML,\tilde{B}}$ (right) and their respective Cramér-Rao bounds, for different observational scenarios, under an aperture selection scheme. 59
6.3 Length of the bounding intervals, $2\beta_{ML,j}$ for $j \in \{1, 2\}$ for different observational scenarios, under an aperture selection scheme. 60
6.4 Relative biases for joint source flux (left) and background (right) estimation for different observational scenarios, under an aperture selection scheme. Solid lines denote the corresponding bounds as given by equation (3.5) while dotted lines are employed for empirical bias estimates. 60
6.5 Variance bounds of the ML estimator for joint source flux (left) and background (right) estimation for different observational scenarios, under an aperture selection scheme. Dashed-dotted-, dashed- and solid lines denote the lower bound, the upper bound and the empirical variance estimate, respectively. 61

6.6 Performance discrepancies of the ML estimator for joint source flux (left) and background (right) estimation for different observational scenarios, under an aperture selection scheme. Dashed-dotted-, dashed- and solid lines denote the lower bound, the upper bound and the empirical variance estimate, respectively. 61
6.7 ML estimates distribution for the baseline scenario using different aperture diameters. Blue markers denote the pairs $(\hat{\tilde{F}}, \hat{\tilde{B}})$, orange marker is used for the ground truth value and green marker denotes the sample means. On the bottom-left corner of each graph the sample Pearson correlation coefficient is displayed. Estimates in each graph are obtained from the same sample set. 62
6.8 Upper bounds for the ML estimates' variances for different implementations of the algorithm. 63
6.9 Empirical performances for different implementations of the ML estimator. 64

Chapter 1

Introduction

1.1 Motivation

In astronomy, one of the key properties to be determined from an object is its brightness. Such parameter allows to perform meticulous analyses on some of its physical properties, such as mass, metallicity and age, and to characterize its evolutionary phase on an Hertzsprung-Russell diagram [Carroll and Ostlie, 2014]. The field of asteroseismology relies on the fluctuation of brightness to study, among other things, the internal composition of stars [Handberg et al., 2021] or stellar dynamics [Diago, 2010].

As light sources in the celestial sphere are not isolated, their observation conveys additional light flux from adjacent objects, instrumental noise and sky background, among other phenomena. Therefore, isolating the target and sky background estimation are broadly recognized as critical steps to achieve precise characterization of an object's flux. To cope with those nuisances, classic approaches rely on aperture methods based on SNR maximization [Howell, 1989], which perform source separation, background inference and photometry in three different and sequential stages [Bertin, E. and Arnouts, S., 1996]. Consequently, the notion of an optimal aperture emerges, beyond which the photometric precision seems to deteriorate as exposure area increases [Naylor, 1998].

Nevertheless, regarding the inference of flux and background (that is, not taking into account the problem of identifying and separating different objects within the field of view), the Data Processing Inequality [Cover and Thomas, 2006] suggests that this sequential estimation process, in which the background estimate is taken as an input of a subsequent photometry algorithm may be a sub-optimal approach, as pixels carrying information about the source's flux also include light coming from background. Therefore, both estimates may benefit from simultaneous inference, as more background-containing pixels are incorporated in its estimation, and the precision gain for that parameter should allow better performance for the source's flux itself.

Simultaneous estimation has been already explored in the astronomical literature, with promising results: from concurrent source detection and background estimation [Guglielmetti et al., 2009, Guglielmetti, 2010] to background inference, photometry and astrometry performed at the same time [Gai et al., 2017]. However the effect of pixel selection has not been thoroughly studied.

This thesis offers some insights in this direction. The relevance of this kind of analysis permeates to related topics such as non-circular aperture shapes (naturally determined by the shape of the detector pixels) or limited apertures [Bickerton and Lupton, 2013].

This thesis assesses this problematic both from fundamental principles based on the Cramér-Rao Bound, which has already been studied in a comprehensive manner in astronomy [Mendez et al., 2013, Mendez et al., 2014]; and from actual achievability with practical implementations of estimators, which already have been proved to be optimal (or near-optimal) for astrometry [Espinosa et al., 2018], with similar results to those presented here.

1.2 Assumptions

Most of this work accounts for the following hypothesis:

- The studied objects are isolated from other similar light sources. That is, inside the observing device's field of view, the measured light comes either from the target source itself or from background.
- Other effects such as zodiacal light or pixel bleeding will not be taken into account. We will assume such effects as not present at all or have been properly managed, and that such cleansing will not have significant effects on our results.
- We consider point sources only, which are assumed to be fully characterizable by a position point in the sky, a function that determines how its light spreads over the observing instrument, and evidently its brightness. For this work, complete and precise knowledge on both location and spreading profile is assumed.

1.3 Objectives

1.3.1 Main Objectives

From a methodological standpoint, part of this thesis aims to the mathematical development of bounds on the statistical performance of implicit estimators, which solve some optimization problem over a high-dimensional space. We also aim to study the problem of joint estimation of source flux and background in astronomy from a theoretical perspective, by means of Cramér-Rao's theory and the characterization of the problem's fundamental limits for precision. Finally, we evaluate some practical solutions for the posed inference problem by assessing the optimality of some classic estimators.

1.3.2 Specific Objectives

The specific objectives of this work are the following:

- Develop a formal and succint generalization of the performance bounds for implicitly defined estimators in the case of an arbitrary number of dimensions or parameters.
- Perform a quantitative analysis of the Cramér-Rao performance bounds and how they evolve as functions of different phenomenological and decision-related conditions, this to support

the idea of using as much information (pixels) as possible when performing simultaneous inference.

- Implementation and analysis of the Maximum Likelihood (ML) estimator and different flavors of the Weighted Least-Squares (WLS) estimator; and assess their optimality relative to fundamental limits.
- Design and implement an adequate estimator for experimental validation of the developed mathematical tools.
- Explore the potential use of our results as a well-founded mean to validate -and discriminate between- different implementations of an estimation algorithm.

1.4 Structure

The structure of the rest of the document is as follows:

- Section 2 introduces the formal definition of the inference problem studied along this work, followed by some important results on parameter estimation and a brief review of previous works that served as inspiration both theoretic- and methodologic-wise.
- Section 3 presents the mathematical tools developed in this work by merging and extending previous results discussed in Section 2.4. This framework allows to place bounds on the performance of multidimensional implicit estimators and constitutes one of the cornerstones of the analysis carried out in following sections.
- Section 4 explores the fundamental limits of the problem of joint estimation of flux and background for point sources. Starting with further specification of the phenomenological model and common assumptions in photometry studies. We analyze the effect of decision over the inference scheme and usage of information on the Cramér-Rao Bounds for different observational scenarios.
- Once theoretical bounds have been characterised, Section 5 examines their achievability by means of practical estimators, specifically different flavors of the Weighted Least-Squares estimator. By adequate selection of the weights we study closed-form expressions for the estimators to assess its optimality, as well as non-closed ones, defined implicitly by an optimization problem. This allows us to put into test and verify the mathematical tools developed in Section 3.
- After experimental validation of our bounding strategy, Section 6 focuses on another classical estimation mechanism: the Maximum Likelihood estimator. We study its optimality with respect to the Cramér-Rao Bounds and possible uses of the results of Section 3 as a way to assess proper implementation of an estimator.
- Section 7 presents the conclusions on this work and some of the possible guidelines for future directions.

Acronyms

ADU Analog to Digital Unit. 18, 20, 35, 52, 58

AWLS Adaptive Weighted Least-Squares. 42, 44

CCD Charge-Coupled Device. 6, 18, 44

CRLB Cramér-Rao Lower Bound. 8–10, 17, 19, 22, 27, 32, 44, 49, 53, 61, 64, 67

FWHM Full-Width at Half-Maximum. 17, 40, 46, 48, 63

IWLS Iterative Weighted Least-Squares. x, 42, 44, 46, 48

LHS Left-hand Side. 9, 32

LS Least-Squares. ix, 11, 36, 40, 41, 47

MAP Maximum A Posteriori. 66

ML Maximum Likelihood. vi, x, xi, 3, 11, 33, 56–67, 97, 99, 102

MSE Mean Squared Error. 8, 9, 23, 29, 31

MVUE Minimal Variance Unbiased Estimator. v, 9–11, 19, 30, 32

PRF Pixel Response Function. 20, 48

PSF Point Spread Function. 6, 7, 17, 20, 21, 24, 36, 40, 47, 48, 54, 58, 60, 62, 66

RHS Right-hand Side. 32

RON Read-out Noise. 18

SNR Signal to Noise Ratio. 1, 11, 19, 25, 65

SWLS Stochastic Weighted Least-Squares. v, vi, x, 42, 44, 46, 48, 50, 51, 53, 54, 59, 62, 67, 91, 93, 96

TESS Transiting Exoplanet Survey Satellite. 8

UWLS Uninformed Weighted Least-Squares. ix, 40, 41, 47

WLS Weighted Least-Squares. v, vi, ix, x, 3, 11, 33–36, 38, 42, 43, 45, 47–50, 57, 65, 67, 85, 89, 91, 93

Chapter 2

Preliminaries and Background

In this section, the formal context and notation of this work is given: the basic setting of the problem is introduced in Section 2.1, followed by some background on parameter estimation shown in Sections 2.2 and 2.3.

2.1 The Joint Source Flux and Background Estimation Problem

The main inference problem posed in this work is that of estimating the brightness of a point source and the expected background noise to be measured by the instrument, which includes open-sky photon emissions and noise from the instrument itself. A point source imaged with a one-dimensional CCD array[1] is parameterized by the pair $(x_c, \tilde{F}) \in \mathbb{R} \times \mathbb{R}^+$, where x_c denotes the relative position of the point source in the array, measured in arcseconds, and $\tilde{F}$ corresponds to the source's brightness measured in photo-e^-. These two parameters induce a probability distribution $\mu_{x_c,\tilde{F}}$ over the sample space $\mathbb{R} \times \mathbb{R}^+ = \mathbb{X}$. A point source represented by a point on $\mathbb{X}$ translates into a nominal brightness profile in the device, which can be expressed by:

$$\tilde{F}_{x_c,\tilde{F}}(x) = \tilde{F} \cdot \phi(x - x_c, \sigma), \tag{2.1}$$

where $\phi(x - x_c, \sigma)$ denotes the one-dimensional Point Spread Function (PSF), which determines the light distribution coming from the point source over the array, parameterized by its width σ (measured in arcseconds), and therefore the quality of the observing site [Mendez et al., 2013, Mendez et al., 2014].

As ground-based observation model let's consider that a photon integrating device (such as CCDs) measures a vector $\mathbf{I} = [I_1, \ldots, I_n]^\intercal$, where $I_i \in \mathbb{N}$ corresponds to the photon count measured by the i^{th} pixel in the device. Each one of these measurements I_i is modelled as an independent Poisson random variable driven by the *total expected* flux $\lambda_i(x_c, \tilde{F})$, given by:

[1] The analysis can be extended to the two-dimensinal case [Mendez et al., 2013].

$$\lambda_i(x_c, \tilde{F}) = \mathbb{E}\{I_i\} = \tilde{F}_i(x_c, \tilde{F}) + \tilde{B}_i, \quad \forall i = 1, \ldots, n, \tag{2.2}$$

where $\tilde{F}_i(x_c, \tilde{F})$ denotes the source's flux profile proportion spread along the i^{th} pixel and $\tilde{B}_i$ denotes the (*expected*) additive background noise coming from external sources other than the observed point source itself, such as photon emissions coming from the open-sky and the noise of the instrument itself (read-out noise and dark-current [Janesick, 2001, Howell, 2006, Janesick, 2007, McLean, 2008]).

The way the expected pixel flux $\tilde{F}_i(x_c, \tilde{F})$ relates to the source's profile is by quantization of the latter. That relation can be expressed through equations (2.3) and (2.4):

$$\tilde{F}_i(x_c, \tilde{F}) = \tilde{F} \cdot g_i(x_c), \quad \forall i = 1, \ldots, n, \tag{2.3}$$

$$g_i(x_c) = \int_{x_i - \frac{\Delta x}{2}}^{x_i + \frac{\Delta x}{2}} \phi(x - x_c, \sigma) dx, \quad \forall i = 1, \ldots, n. \tag{2.4}$$

In equation (2.4), x_i denotes the relative position of the i^{th} pixel's center projected into the sky, while $\forall i = 1, \ldots, n-1, \Delta x = x_{i+1} - x_i$ denotes the array resolution or pixel size. Both quantities are measured in arcseconds. Note that, for $g_i(x_c)$ to be a dimensionless quantity, the point spread function ϕ shall take values measured in arcsec^{-1}. Though not strictly necessary for the analysis in future sections, a basic assumption is that of good coverage of the studied object [Lobos et al., 2015, Espinosa et al., 2018], in the sense that given its relative position x_c:

$$\sum_{i=1}^{n} g_i(x_c) \approx \sum_{i \in \mathbb{Z}} g_i(x_c) = \int_{-\infty}^{\infty} \phi(x - x_c, \sigma) = 1. \tag{2.5}$$

Satisfying the assumption shown in equation (2.5) should lead to consistent and more precise estimations, as will be shown later in Sections 5 and 6.

Assuming absolutely precise knowledge of the source's PSF and position x_c, the inference problem studied is that of estimating the expected flux parameters $\tilde{F}$ and $\tilde{B}_i$. Nevertheless, the dimensionality of this estimation problem can be reduced considerably under the assumption of *homogeneous background*, which states that $\tilde{B}_i = \tilde{B}, \forall i = 1, \ldots, n$. Note that the *background* $\tilde{B}$ corresponds to background flux per pixel and not to a quantity spread along the instrument, it is therefore measured in photo-e^-/pixel. Such an assumption is commonly used for the photometry estimation problem [Lindegren, 2008, Gai et al., 2017]. That allows to rewrite $\lambda_i(x_c, \tilde{F})$ as:

$$\lambda_i(x_c, \tilde{F}) = \mathbb{E}\{I_i\} = \tilde{F} \cdot g_i(x_c) + \tilde{B}, \quad \forall i = 1, \ldots, n. \tag{2.6}$$

The independence relation $I_i \perp\!\!\!\perp I_j, i \neq j$ allows to write the *likelihood* (joint probability function) of the observation vector $\mathbf{I}$, given source parameters $(x_c, \tilde{F})$ and background $\tilde{B}$, as:

$$
\begin{aligned}
L(\mathbf{I}; x_c, \tilde{F}, \tilde{B}) &= p(\mathbf{I}|x_c, \tilde{F}, \tilde{B}) \\
&= \prod_{i=1}^{n} \frac{e^{-\lambda_i(x_c,\tilde{F})} \cdot \lambda_i^{I_i}(x_c, \tilde{F})}{I_i!} \\
&= \prod_{i=1}^{n} \frac{e^{-\left(\tilde{F}\cdot g_i(x_c)+\tilde{B}\right)} \cdot \left(\tilde{F} \cdot g_i(x_c) + \tilde{B}\right)^{I_i}}{I_i!}.
\end{aligned}
\tag{2.7}
$$

It is worth noting that despite $\tilde{F}$ and $\tilde{B}$ being measured in units of counts (or photo-e$^-$) both quantities take values in $\mathbb{R}^+$. The main reason behind this is that both variables combine both the count rates over time and the fixed integration (or imaging) time t. More formally, each observation I_i is a *Counting Process*, or *Poisson Process* [Ross, 1996] whose increments $I_i = N(t)$ distribute as a Poisson random variable with parameter $\lambda_i' t = \lambda_i$, where λ_i' denotes the count rate of the process in units of photo-e$^-$/sec. Though it is possible to focus the problem on estimating the count rate itself (see, for example, the data products developed by the TESS Data for Asteroseismology group [Handberg et al., 2021]), and similar results to those shown in this work may be found, it is not the current focus nor our approach to the problem.

More formally, the posed estimation task is that of finding a parameter vector $\hat{\boldsymbol{\theta}} = (\hat{\tilde{F}}, \hat{\tilde{B}})$ that accounts as a prescription (or statistics) that allows to infer the underlying parameters $(\tilde{F}, \tilde{B})$ from $\mathbf{I}$. The estimations $(\hat{\tilde{F}}, \hat{\tilde{B}})$ are then given by a decision rule $\tau(\mathbf{I}) : \mathbb{N}^n \to \boldsymbol{\Theta} = \mathbb{R}^+ \times \mathbb{R}^+$ so that $(\hat{\tilde{F}}, \hat{\tilde{B}}) \equiv \tau(\mathbf{I})$.

2.2 The Cramér-Rao Lower Bound

The celebrated Cramér-Rao Lower Bound (CRLB) [Rao, 1945, Cramér, 1946] offers a performance bound on the expected variance (estimation error) of the family of unbiased estimators. More precisely, let $\{I_i\}_{i=1}^n$ be a collection of independent observations, whose probability density (or mass) function $L(\cdot; \boldsymbol{\theta})$ is induced by a parameter vector $\boldsymbol{\theta} = (\theta_1, \ldots, \theta_m) \in \boldsymbol{\Theta}, m \in \mathbb{N}$ over a parameter space $\boldsymbol{\Theta}$ (typically $\boldsymbol{\Theta} = \mathbb{R}^m$). The objective of an estimation problem is to find a parameter vector $\hat{\boldsymbol{\theta}} \in \boldsymbol{\Theta}$ called estimator. Hopefully, $\hat{\boldsymbol{\theta}}$ shall be *unbiased*[2], so that the absolute error in the limit equals 0, and have low variance, in order to achieve the lowest Mean Squared Error (MSE). To illustrate this [Kay, 1993], in a one-dimensional estimation problem, let $b(\hat{\theta})$ be the estimator's bias, then

$$
b(\hat{\theta}) = \mathbb{E}\{\hat{\theta}\} - \theta = 0. \tag{2.8}
$$

Then, the MSE can be expressed as

[2]In the sense that $\mathbb{E}\{\hat{\boldsymbol{\theta}}\} = \boldsymbol{\theta}$.

$$
\begin{aligned}
MSE(\hat{\theta}) &= \mathbb{E}\left\{\left(\hat{\theta}-\theta\right)^2\right\} \\
&= Var(\hat{\theta}) - \left(E\{\hat{\theta}-\theta\}\right)^2 \\
&= Var(\hat{\theta}) - b^2(\hat{\theta}) \\
&= Var(\hat{\theta}).
\end{aligned} \tag{2.9}
$$

Because of this, an unbiased estimator that is *optimal* in terms of the MSE is often referred to as the Minimal Variance Unbiased Estimator (MVUE).

Given the relevance that the concept of variance has in usual estimation problems, it is fortunate that the CRLB offers performance bounds in terms of variance, which are given under some regularity conditions. Furthermore, it allows (under certain conditions, which are not always satisfied[3]) to formulate the estimator that achieves said bound, which will naturally be the MVUE. The CRLB in its vector form is stated as follows:

Theorem 2.1 (Cramér-Rao Lower Bound) *Let $\boldsymbol{\theta} = \{\theta_1, \ldots, \theta_m\}, m \in \mathbb{N}$ be a collection of parameters over a parameter space $\boldsymbol{\Theta}$, which induces a probability distribution $L(\mathbf{I}; \boldsymbol{\theta})$ on an observation space $\mathbb{O}$ such that the following **regularity condition** is satisfied:*

$$
\mathbb{E}_{\mathbb{I}\sim L(\mathbf{I};\boldsymbol{\theta})}\left\{\frac{\partial \ln L(\mathbf{I};\boldsymbol{\theta})}{\partial \theta_i}\right\} = 0, \quad \forall i \in \{1,\ldots,m\}, \forall \boldsymbol{\theta} \in \boldsymbol{\Theta}. \tag{2.10}
$$

Then, any unbiased estimator $\hat{\boldsymbol{\theta}}$ of $\boldsymbol{\theta}$, given by a decision rule $\tau : \mathbb{N}^n \to \boldsymbol{\Theta}, \hat{\boldsymbol{\theta}} \equiv \tau(\mathbf{I})$, has a covariance matrix $\mathbf{C}_{\hat{\boldsymbol{\theta}}}$ that satisfies:

$$
\mathbf{C}_{\hat{\boldsymbol{\theta}}} - \mathcal{I}_{\boldsymbol{\theta}}^{-1} \succeq \mathbf{0}, \tag{2.11}
$$

where $\succeq \mathbf{0}$ denotes that the matrix on the LHS is positive semi-definite and $\mathcal{I}_{\boldsymbol{\theta}} \in \mathcal{M}^{m\times m}$ denotes the Fisher Information Matrix, which is defined by:

$$
[\mathcal{I}_{\boldsymbol{\theta}}]_{(i,j)} = -\mathbb{E}_{\mathbf{I}\sim L(\mathbf{I};\boldsymbol{\theta})}\left\{\frac{\partial^2 \ln L(\mathbf{I};\boldsymbol{\theta})}{\partial\theta_i \partial\theta_j}\right\} = \mathbb{E}_{\mathbf{I}\sim L(\mathbf{I};\boldsymbol{\theta})}\left\{\frac{\partial \ln L(\mathbf{I};\boldsymbol{\theta})}{\partial\theta_i}\cdot\frac{\partial \ln L(\mathbf{I};\boldsymbol{\theta})}{\partial\theta_j}\right\}, \quad \forall i,j \in \{1,\ldots,m\}. \tag{2.12}
$$

Moreover, if there exists some function $\mathbf{h} : \mathbb{O} \to \boldsymbol{\Theta}$ such that

$$
\frac{\partial \ln L(\mathbf{I};\boldsymbol{\theta})}{\partial \theta_i} = \left[\mathcal{I}_{\boldsymbol{\theta}}(\mathbf{h}(\mathbf{I}) - \boldsymbol{\theta})\right]_i, \quad \forall i \in \{1,\ldots,m\}, \tag{2.13}
$$

[3]This does not mean that there's no MVUE, but that the MVUE's (co)variance does not achieve the bounds.

then the MVUE is given by $\hat{\boldsymbol{\theta}} = \mathbf{h}(\mathbf{I})$*, and its covariance matrix is* $\mathcal{I}_{\boldsymbol{\theta}}^{-1}$*.*

From Theorem 2.1, it follows that for any unbiased estimator:

$$Var(\hat{\theta}_i) = [\mathbf{C}_{\hat{\boldsymbol{\theta}}}]_{(i,i)} \geq [\mathcal{I}_{\boldsymbol{\theta}}^{-1}]_{(i,i)}, \quad \forall i \in \{1, \ldots, m\}. \tag{2.14}$$

Though Theorem 2.1 does not assert the existence of an estimator that achieves the CRLB, it is still possible to find the MVUE. To do so, one can resort to *sufficient statistics theory* [Kay, 1993].

2.3 Sufficient Statistics

When the decomposition presented in Theorem 2.1 through equation (2.13) can not be satisfied, there's no such an estimator that attains the CRLB. Nevertheless, it is still possible to find the MVUE, that is a function (or decision rule) $\tau^*(\mathbf{I})$ in the space of functions from $\mathbb{O}$ to $\boldsymbol{\Theta} \subseteq \mathbb{R}^m$ that are unbiased such that, for any other function $\tau(\mathbf{I})$ in the same space:

$$Var(\tau_i(\mathbf{I})) \geq Var(\tau_i^*(\mathbf{I})) > [\mathcal{I}_{\boldsymbol{\theta}}^{-1}]_{(i,i)}, \quad \forall i \in \{1, \ldots, m\}. \tag{2.15}$$

Theory on sufficient statistics offers some useful theorems and tools to find such and estimator. More formally, a *statistic* $T(\mathbf{I})$ is a random variable, function of a sample vector whose probability function is parameterized by a parameter vector $\boldsymbol{\theta}$, *i.e.*, $\mathbf{I} \sim p(\mathbf{I}|\boldsymbol{\theta})$.

$T(\mathbf{I})$ is said to be *sufficient* if new observations $\mathbf{I}$, conditioned on a realization of T, become independent from $\boldsymbol{\theta}$. This notion is formalized through the Neyman-Fisher Factorization Theorem (see Theorem 2.2), which also allows to find such an statistic.

Theorem 2.2 (Neyman-Fisher Factorization Theorem) *If the probability function of a random variable* $\mathbf{I}$*,* $p(\mathbf{I}|\boldsymbol{\theta})$*, can be written as:*

$$p(\mathbf{I}|\boldsymbol{\theta}) = g(T(\mathbf{I}), \boldsymbol{\theta}) \cdot h(\mathbf{I}), \tag{2.16}$$

being g *some function that depends on* $\mathbf{I}$ *only through* T*, and* h *a function of* $\mathbf{I}$ *only; then* $T(\mathbf{I})$ *is a* ***sufficient statistic*** *for* $\boldsymbol{\theta}$*. Conversely, if* $T(\mathbf{I})$ *is a sufficient statistic for* $\boldsymbol{\theta}$*, the likelihood of the observations,* $p(\mathbf{I}|\boldsymbol{\theta})$ *can be factorized as in equation (2.16).*

It is important to note that Theorem 2.2 does not guarantees the existence of such an statistic for a given likelihood function, only a property it satisfies if it exists.

If a sufficient statistic for $\boldsymbol{\theta}$ is found, the Rao-Blackwell-Lehmann-Scheffe (RBLS) Theorem [Levy, 2008] allows to find the MVUE from that statistic.

Theorem 2.3 (Rao-Blackwell-Lehmann-Scheffe Theorem) *Let* $\check{\boldsymbol{\theta}}$ *be an unbiased estimator of* $\boldsymbol{\theta}$

and $T(\mathbf{I})$ a sufficient statistic for $\boldsymbol{\theta}$, then its conditional expectation $\hat{\boldsymbol{\theta}} \equiv \mathbb{E}_{\mathbf{I}\sim p(\mathbf{I}|\boldsymbol{\theta})}\{\check{\boldsymbol{\theta}}|T(\mathbf{I})\}$ is

1. *a valid estimator for $\boldsymbol{\theta}$ (*i.e.*, not explicitly dependent on $\boldsymbol{\theta}$)*
2. *unbiased*
3. *of lesser variance than that of $\check{\boldsymbol{\theta}}, \forall \boldsymbol{\theta} \in \boldsymbol{\Theta}$, in the sense that, if*

$$\begin{aligned} \mathbf{C}_{\check{\boldsymbol{\theta}}} &\equiv \mathbb{E}_{\mathbf{I}\sim p(\mathbf{I}|\boldsymbol{\theta})}\{(\check{\boldsymbol{\theta}} - \boldsymbol{\theta})(\check{\boldsymbol{\theta}} - \boldsymbol{\theta})^{\dagger}\}, \\ \mathbf{C}_{\hat{\boldsymbol{\theta}}} &\equiv \mathbb{E}_{\mathbf{I}\sim p(\mathbf{I}|\boldsymbol{\theta})}\{(\hat{\boldsymbol{\theta}} - \boldsymbol{\theta})(\hat{\boldsymbol{\theta}} - \boldsymbol{\theta})^{\dagger}\} \end{aligned} \tag{2.17}$$

   denote the covariance matrices of $\check{\boldsymbol{\theta}}$ and $\hat{\boldsymbol{\theta}}$, respectively, then $\mathbf{C}_{\hat{\boldsymbol{\theta}}} \succeq \mathbf{C}_{\check{\boldsymbol{\theta}}}$.

Additionally, if $T(\mathbf{I})$ is complete, $\hat{\boldsymbol{\theta}}$ is the MVUE.

A sufficient statistic $T(\mathbf{I})$ is said to be ***complete*** *if and only if there exists only one function $g(T(\mathbf{I}))$ that is unbiased,* i.e.*, such that $\mathbb{E}_{\mathbf{I}\sim p(\mathbf{I}|\boldsymbol{\theta})}\{g(T(\mathbf{I}))\} = \boldsymbol{\theta}$.*

Note that the completeness of $T(\mathbf{I})$ is itself a property of the model $p(\mathbf{I}|\boldsymbol{\theta})$. In particular, the family of exponential density functions is complete [Kay, 1993, Levy, 2008].

2.4 Related Work

The current work is heavily influenced in its methodology by the works of Méndez et al. on Cramér-Rao [Mendez et al., 2013] and Espinosa et al. on near-optimal estimators [Espinosa et al., 2018] for astrometry.

The former aims to characterize exhaustively the Cramér-Rao Bounds for the problem of estimating the relative position of a resolved point source. The authors explore the behavior of the bound under different observational scenarios and find interesting limits for source-dominated and background-dominated cases. They find as well that, for a wide range of signal-to-noise ratios, the Maximum Likelihood and Least-Squares (LS) estimators approach the bound tightly. This work is expanded to a two-dimensional case in which astrometry is determined alongside photometry [Mendez et al., 2014]. Therein, scenario's SNR and joint Cramér-Rao bounds are related with good correspondence between them, as well as predictions that confirm common heuristics on the field in a theoretic-based manner are performed.

The second work mentioned assesses the optimality of the ML and WLS estimators for astrometry by expanding Fessler's work on implicit estimators [Fessler, 1996]. Fessler developed general first and second order Taylor expansions for said kind of estimators to allow bias and variance approximations. Espinosa et al. restricted themselves to the one-dimensional case, but developed Fessler's methodology further by formulating bounds on those quantities rather than just approximations. With that newly formulated mathematical tools they studied the behaviors of the estimators with respect to the Cramér-Rao bound already discussed [Mendez et al., 2013], finding that ML offers optimal performance over a wide range of relevant observational conditions, both by showing that their bounds tightly enclose the fundamental limit and how the empirical precision matches it. WLS estimator was shown to be less consistent as it exhibits sub-optimal performance as SNR increases. The current work recovers their spirit and formulations to expand them back to the multidimensional case, allowing work on any number of parameters.

Last but not least, it is worth noting two practical examples of joint estimation already put into practice in the astronomy field.

On one hand stands the Bayesian background-source separation technique developed by Guglielmetti in her Ph.D. dissertation [Guglielmetti, 2010]. Briefly put, the method successfully perform accurate background estimates while detecting different sources on an image. However, the stepwise paradigm remains partially as detected source's flux estimates require the previous background ones[4].

Back on the parametric estimation field lies the work of Gai et al. on joint estimation of flux, background and position [Gai et al., 2017]. They developed a maximum likelihood framework to simultaneously get consistent estimates for these three quantities. They also studied the correlation between their estimates in a well-understood manner.

[4]The current work is not different for that matter, nevertheless. Here we take for granted the detection phase, while merging the background-flux estimation ones.

Chapter 3

Finding Performance Bounds for high-dimensional Implicit Estimators

As stated in Section 2.1, an estimator is given by a decision rule $\tau_J(\cdot)$, which is often given as the solution of a generic optimization problem of the form

$$\tau_J(\mathbf{I}) \equiv \underset{\boldsymbol{\alpha}\in\boldsymbol{\Theta}}{\operatorname{argmin}} J(\boldsymbol{\alpha}, \mathbf{I}), \tag{3.1}$$

where $\boldsymbol{\alpha}$ represents the resulting p-dimensional vector parameter, and $\mathbf{I}$ is a n-dimensional observation vector. This generalization can lead to two different situations: either the resulting decision rule can be obtained in a closed or *explicit* form, where its variance and bias may be determined directly. The other possible scenario is that of an *implicit* estimator [Fessler, 1996, Lobos et al., 2015, Espinosa et al., 2018]. This latter case is difficult to assess since not having an expression for $\tau_J(\cdot)$ prevents one to determine its moments.

For the last case, one can resort to a Taylor expansion in order to approximate [Fessler, 1996] or bound [Espinosa et al., 2018] both the estimator's bias and variance. The proposed methodology in [Espinosa et al., 2018] to bound the performance of a single-parameter implicit estimator can be extended to the multidimensional case.

For that matter, it is assumed that the cost function $J(\boldsymbol{\alpha}, \mathbf{I})$ has a unique optimal value at $\boldsymbol{\alpha} = \tau_J(\mathbf{I})$ such that it also satisfies the first order condition given in equation (3.2). Note that, given an observation vector $\mathbf{I}$, $J(\boldsymbol{\alpha}, \mathbf{I})$ is a function depending only on the parameter vector $\boldsymbol{\alpha}$.

$$\begin{aligned} \mathbf{0} = \nabla J(\boldsymbol{\alpha}, \mathbf{I})\Big|_{\boldsymbol{\alpha}=\tau_J(\mathbf{I})} &= [J'(\boldsymbol{\alpha}, \mathbf{I})]^{\intercal}\Big|_{\boldsymbol{\alpha}=\tau_J(\mathbf{I})} \\ &= \begin{bmatrix} \frac{\partial}{\partial\alpha_1} J(\tau_J(\mathbf{I}), \mathbf{I}) \\ \vdots \\ \frac{\partial}{\partial\alpha_p} J(\tau_J(\mathbf{I}), \mathbf{I}) \end{bmatrix}. \end{aligned} \tag{3.2}$$

Under these general assumptions, the estimator's Taylor expansion around the mean vector $\bar{\mathbf{I}}$ is as follows:

$$\tau_J(\mathbf{I}) \approx \tau_J(\bar{\mathbf{I}}) + \tau'_J(\bar{\mathbf{I}}) \cdot (\mathbf{I} - \bar{\mathbf{I}}) + e(\bar{\mathbf{I}}, \mathbf{I} - \bar{\mathbf{I}}), \tag{3.3}$$

where

$$\begin{aligned} \mathbf{e}(\bar{\mathbf{I}}, \mathbf{I} - \bar{\mathbf{I}}) &= \frac{1}{2} \sum_{i=1}^{n} \sum_{h=1}^{n} \frac{\partial^2}{\partial I_i \partial I_h} \tau_J(\bar{\mathbf{I}} + t(\mathbf{I} - \bar{\mathbf{I}}))(I_i - \bar{I}_i)(I_h - \bar{I}_h) \\ &= \frac{1}{2} \sum_{i=1}^{n} \sum_{h=1}^{n} \begin{bmatrix} \frac{\partial^2}{\partial I_i \partial I_h} \tau_{J,1}(\bar{\mathbf{I}} + t(\mathbf{I} - \bar{\mathbf{I}})) \\ \vdots \\ \frac{\partial^2}{\partial I_i \partial I_h} \tau_{J,p}(\bar{\mathbf{I}} + t(\mathbf{I} - \bar{\mathbf{I}})) \end{bmatrix} (I_i - \bar{I}_i)(I_h - \bar{I}_h), \end{aligned} \tag{3.4}$$

for some fixed but unknown value $t \in [0, 1]$. The expansion in equation (3.3) can be used to bound the bias and variance associated to each of the vector's components. Noting $\boldsymbol{\alpha}^\star$ as the ground-truth parameter vector, it follows that, for each $j \in \{1, \ldots, p\}$:

$$\begin{aligned} |\mathbb{E}_{\mathbf{I} \sim L(\mathbf{I}; \boldsymbol{\alpha}^\star)} \{\tau_{J,j}(\mathbf{I})\} - \alpha_j^\star| &\leq |\tau_{J,j}(\bar{\mathbf{I}}) - \alpha_j^\star| + \max_{t \in [0,1]} \left| \mathbb{E}_{\mathbf{I} \sim L(\mathbf{I}; \boldsymbol{\alpha}^\star)} \left\{ e_j(\bar{\mathbf{I}}, \mathbf{I} - \bar{\mathbf{I}}) \right\} \right| \\ &\equiv |\tau_{J,j}(\bar{\mathbf{I}}) - \alpha_j^\star| + \varepsilon_{J,j} \\ &\equiv \varepsilon'_{J,j}, \end{aligned} \tag{3.5}$$

$$Var(\tau_{J,j}(\mathbf{I})) \in \left[\left[\tau'_J(\bar{\mathbf{I}}) \right]_{(j,\cdot)} Cov(\mathbf{I}) \left[\tau'_J(\bar{\mathbf{I}}) \right]^\intercal_{(j,\cdot)} - \beta_{J,j}, \left[\tau'_J(\bar{\mathbf{I}}) \right]_{(j,\cdot)} Cov(\mathbf{I}) \left[\tau'_J(\bar{\mathbf{I}}) \right]^\intercal_{(j,\cdot)} + \beta_{J,j} \right] [1], \tag{3.6}$$

where

$$\beta_{J,j} = \max_{t \in [0,1]} \mathbb{E}_{\mathbf{I} \sim L(\mathbf{I}; \boldsymbol{\alpha}^\star)} \left\{ \left(e_j(\bar{\mathbf{I}}, \mathbf{I} - \bar{\mathbf{I}}) \right)^2 \right\} + 2 \max_{t \in [0,1]} \left| \mathbb{E}_{\mathbf{I} \sim L(\mathbf{I}; \boldsymbol{\alpha}^\star)} \left\{ \left[\tau'_{J,j}(\bar{\mathbf{I}}) \right]_{(j,\cdot)} (\mathbf{I} - \bar{\mathbf{I}}) \cdot e_j(\bar{\mathbf{I}}, \mathbf{I} - \bar{\mathbf{I}}) \right\} \right|. \tag{3.7}$$

For ease of notation, we define $\sigma^2_{J,j} \equiv \left[\tau'_J(\bar{\mathbf{I}}) \right]_{(j,\cdot)} Cov(\mathbf{I}) \left[\tau'_J(\bar{\mathbf{I}}) \right]^\intercal_{(j,\cdot)}$ to be the central value of the interval in (3.6), *i.e.*:

$$Var(\tau_{J,j}(\mathbf{I})) \in \left[\sigma^2_{J,j} - \beta_{J,j}, \sigma^2_{J,j} + \beta_{J,j} \right]. \tag{3.8}$$

[1] In what remains of this work, the expectations that define second-order momenta such as $Var(\cdot)$ and $Cov(\cdot)$ are taken w.r.t the likelihood function $L(\mathbf{I}; \boldsymbol{\alpha}^\star)$, unless otherwise stated.

These inequalities heavily resemble those found by [Espinosa et al., 2018] for the one-dimensional case, *i.e.*, $p = 1$, and do not depend on the exact value of $\tau_J(\mathbf{I})$, but on its first- and second-order derivatives; being their calculation a critical task to work up to.

The components of said derivatives can be calculated by following a similar methodology of that proposed by Fessler [Fessler, 1996]. For that purpose a family of operators can be stated as follows: let $i, j \in \mathbb{N}$ and a real function $f(\boldsymbol{\alpha}, \mathbf{I}), f : \boldsymbol{\Theta} \times \mathbb{N}^n \to \mathbb{R}$, then $\nabla^{ij} f(\cdot)$ denotes a tensor function

$$\nabla^{ij} f(\cdot) = \frac{\partial^{i+j}}{\partial \boldsymbol{\alpha}^i \partial \mathbf{I}^j} f(\cdot), \tag{3.9}$$

where f is derived i times with respect to the vector $\boldsymbol{\alpha}$ and j times with respect to $\mathbf{I}$.

Then, the first derivative of τ_J evaluated at some observation vector $\mathbf{I}$, namely

$$\begin{aligned} \tau'_J(\mathbf{I}) &= \begin{bmatrix} \frac{\partial}{\partial I_1}\tau_J(\mathbf{I}) & \dots & \frac{\partial}{\partial I_n}\tau_J(\mathbf{I}) \end{bmatrix} \\ &= \begin{bmatrix} \frac{\partial}{\partial I_1}\tau_{J,1}(\mathbf{I}) & \dots & \frac{\partial}{\partial I_n}\tau_{J,1}(\mathbf{I}) \\ \vdots & \ddots & \vdots \\ \frac{\partial}{\partial I_1}\tau_{J,p}(\mathbf{I}) & \dots & \frac{\partial}{\partial I_n}\tau_{J,p}(\mathbf{I}) \end{bmatrix}, \end{aligned} \tag{3.10}$$

can be calculated as

$$\tau'_J(\mathbf{I}) = -\left[\nabla^{20} J(\tau_J(\mathbf{I}), \mathbf{I})\right]^{-1} \left[\nabla^{11} J(\tau_J(\mathbf{I}), \mathbf{I})\right], \tag{3.11}$$

where $\nabla^{20} J(\tau_J(\mathbf{I}), \mathbf{I})$ and $\nabla^{11} J(\tau_J(\mathbf{I}), \mathbf{I})$ denote $p \times p$ and $p \times n$ matrices, respectively. Thus being $\tau'_J(\mathbf{I})$ a $p \times n$ matrix.

Finding the second-order derivative $\tau''_J(\mathbf{I})$ boils down to calculate each of the n^2 vectorial components

$$\frac{\partial^2}{\partial I_i \partial I_h}\tau_J(\mathbf{I}) = \left[\frac{\partial^2}{\partial I_i \partial I_h}\tau_{J,1}(\mathbf{I}) \quad \dots \quad \frac{\partial^2}{\partial I_i \partial I_h}\tau_{J,p}(\mathbf{I})\right]^{\intercal}. \tag{3.12}$$

In order to find the p components of the vector defined in equation (3.12) one can resort to Fessler's equation (15) [Fessler, 1996], which allows to state a set of p equations in said p unknowns. Therefore, the derivative in equation (3.12) can be written in a matrix form as

$$\frac{\partial^2}{\partial I_i \partial I_h}\tau_J(\mathbf{I}) = -\left[\nabla^{20} J(\tau_J(\mathbf{I}), \mathbf{I})\right]^{-1} \left[P_J^{i,h}(\mathbf{I}) + Q_J^{i,h}(\mathbf{I})\right], \tag{3.13}$$

where

$$P_J^{i,h}(\mathbf{I}) \equiv \left[[\tau_J'(\mathbf{I})]_{(\cdot,i)}^{\intercal} \left[\nabla^{30} J(\tau_J(\mathbf{I}), \mathbf{I}) \right]_{(j,\cdot,\cdot)} [\tau_J'(\mathbf{I})]_{(\cdot,h)} + \left[\nabla^{21} J(\tau_J(\mathbf{I}), \mathbf{I}) \right]_{(j,\cdot,h)} [\tau_J'(\mathbf{I})]_{(\cdot,i)} \right]_{j=1}^{p} \in \mathbb{R}^{p \times 1}, \tag{3.14}$$

$$Q_J^{i,h}(\mathbf{I}) \equiv \left[\left[\nabla^{21} J(\tau_J(\mathbf{I}), \mathbf{I}) \right]_{(j,\cdot,i)} [\tau_J'(\mathbf{I})]_{(\cdot,h)} + \left[\nabla^{12} J(\tau_J(\mathbf{I}), \mathbf{I}) \right]_{(j,i,h)} \right]_{j=1}^{p} \in \mathbb{R}^{p \times 1}. \tag{3.15}$$

The demonstration for the equations and bounds exposed in this section is detailed in Appendix A.

Chapter 4

Cramér-Rao Lower Bound for Joint Source Flux and Background Estimation

In this section, the behavior of the Fisher Information Matrix and the CRLBs for the joint estimation problem introduced in Section 2.1 is studied through simulations. In order to do that, some model considerations need to be specified. On one hand, a Gaussian PSF is assumed, *i.e.*,

$$\phi(x) = \frac{1}{\sqrt{2\pi\sigma^2}} \exp\left(-\frac{1}{2}\frac{x^2}{\sigma^2}\right), \tag{4.1}$$

which is a reasonable choice in the considered context of a ground-based observation model [Mendez et al., 2010]. From equation (2.5) it verifies that $\tilde{F}$ is indeed the total expected flux of the source spread along the array:

$$\begin{aligned}
\sum_{i=1}^{n} \tilde{F}_i(x_c, \tilde{F}) &= \tilde{F} \sum_{i=1}^{n} g_i(x_c) \\
&= \tilde{F} \sum_{i=1}^{n} \int_{x_i - \frac{\Delta x}{2}}^{x_i + \frac{\Delta x}{2}} \phi(x - x_c, \sigma) dx \\
&\approx \tilde{F} \int_{-\infty}^{\infty} \phi(x - x_c, \sigma) dx \\
&= \tilde{F}.
\end{aligned} \tag{4.2}$$

As was said before, σ is usually related to image quality, since narrower PSFs translate into less light-spreading. An alternative measure of quality is that of "Full-Width at Half-Maximum" (FWHM), which is related to the Gaussian σ through:

$$FWHM = 2\sqrt{2\ln 2}\sigma. \tag{4.3}$$

For astronomical applications, detector's noise sources are dominated by the diffuse light coming from the sky due to the long exposure times (unless the targeted source is too bright and requires very short exposures), then the background per pixel $\tilde{B}$ is dependent on the pixel size Δx. Such a background model can be formulated by [Mendez et al., 2013] [Winick, 1986]:

$$\tilde{B} = G\Delta x f_s + D + RON^2, \tag{4.4}$$

where G denotes the detector's (inverse-) gain in units of photo-e$^-$/ADU (ADU stands for "analog to digital unit"), f_s denotes the sky background in units of ADUs/arcsec, and D and RON denote dark-current and read-out noise, respectively, in units of photo-e$^-$. This model allows to translate noise from the sky itself into individual pixels, taking into account instrumental noise too, while being able to capture the effect of exposure time through f_s [Winick, 1986].

Note that the source's flux and the background can be transformed into ADUs through G, and vice versa. Those conversions are denoted as F and B, respectively, and relate to the quantities measured in photo-e$^-$ by means of:

$$\tilde{F} = G \cdot F, \tag{4.5}$$

$$\tilde{B} = G \cdot B. \tag{4.6}$$

For analysis purposes, it is also worthwhile to develop a measurable form of signal-to-noise ratio [Mendez et al., 2013] that captures to some extent the quality of the signal as the source is observed through the CCD detector under determined sky conditions. The sampled signal S (in photo-e$^-$) can be defined as:

$$S = \tilde{F} \cdot \int_{x_l}^{x_u} \phi(x - x_c, \sigma)dx, \tag{4.7}$$

where x_l and x_u are suitably chosen (but arbitrary) apertures such that an appreciable fraction of the total flux is included. For the Gaussian case considered above, this expression can be written as:

$$S = \tilde{F} \cdot P(u_+), \quad P(u) = \frac{2}{\sqrt{\pi}} \int_0^u e^{-v^2} dv, \tag{4.8}$$

where $u_+ = (x_u - x_l)/\sqrt{2}\sigma$ denotes the chosen aperture, which is symmetric with respect to the source's position x_c, that is $x_u - x_c = x_c - x_l$.

The total noise, N, is considerred to have contributions from the detector's read-out noise, from the sky noise and the noise from the source itself [Mendez et al., 2013], all of them assumed to follow a Poisson distribution, such that:

$$N = \sqrt{S + N_{pix}(G\Delta x f_s + RON^2)}, \tag{4.9}$$

where N_{pix} denotes the number of pixels under the same region in which the signal S was sampled, *i.e.*, the pixels used to get an estimation $\hat{\tilde{F}}$. Finally, the signal-to-noise ratio (SNR) is given by S/N. This definition can be extended and generalized. To do so, let $\mathcal{J} \subseteq \{1, \ldots, n\}$ be a set of sub-indices such that $N_{pix} = |\mathcal{J}|$. $\mathcal{J}$ denotes the indices of the pixels to be used to perform the estimation through a decision rule $\tau(\cdot)$. Therefore, the signal sampled with pixels whose index i is contained in $\mathcal{J}$, $S_{\mathcal{J}}$, and the corresponding total noise, $N_{\mathcal{J}}$, are given by:

$$S_{\mathcal{J}} = \tilde{F} \cdot \sum_{i \in \mathcal{J}} g_i(x_c), \tag{4.10}$$

$$\begin{aligned} N_{\mathcal{J}} &= \sqrt{S_{\mathcal{J}} + N_{pix}(G\Delta x f_s + RON^2)} \\ &= \sqrt{S_{\mathcal{J}} + |\mathcal{J}|(G\Delta x f_s + RON^2)}. \end{aligned} \tag{4.11}$$

Under the assumption that only full pixels are taken into consideration, *i.e.*, x_l and x_u can only take values on the borders of pixels[1], there would be some set of indices $\mathcal{J}$ such that $S_{\mathcal{J}} = S$ and $N_{\mathcal{J}} = N$, for some pair (x_l, x_u).

When the pixels indexed by $\mathcal{J}$ are used as information sources, the Fisher information matrix for the joint estimation problem posed here can be expressed as:

$$\mathcal{I}_{\boldsymbol{\theta}} = \begin{bmatrix} \sum_{i \in \mathcal{J}} \frac{g_i^2(x_c)}{\lambda_i(x_c, \tilde{F})} & \sum_{i \in \mathcal{J}} \frac{g_i(x_c)}{\lambda_i(x_c, \tilde{F})} \\ \sum_{i \in \mathcal{J}} \frac{g_i(x_c)}{\lambda_i(x_c, \tilde{F})} & \sum_{i \in \mathcal{J}} \frac{1}{\lambda_i(x_c, \tilde{F})} \end{bmatrix} \equiv \begin{bmatrix} \mathcal{I}_{1,1} & \mathcal{I}_{1,2} \\ \mathcal{I}_{2,1} & \mathcal{I}_{2,2} \end{bmatrix}. \tag{4.12}$$

Note that, as expected, $\mathcal{I}_{1,2} = \mathcal{I}_{2,1}$. Then, as stated in Theorem 2.1, the CRLBs are given by:

$$Var(\hat{\tilde{F}}) \geq \sigma_{\tilde{F}}^2 = \frac{\mathcal{I}_{2,2}}{\mathcal{I}_{1,1} \cdot \mathcal{I}_{2,2} - \mathcal{I}_{1,2}^2} = \frac{\mathcal{I}_{2,2}}{|\mathcal{I}_{\boldsymbol{\theta}}|}, \tag{4.13}$$

$$Var(\hat{\tilde{B}}) \geq \sigma_{\tilde{B}}^2 = \frac{\mathcal{I}_{1,1}}{\mathcal{I}_{1,1} \cdot \mathcal{I}_{2,2} - \mathcal{I}_{1,2}^2} = \frac{\mathcal{I}_{1,1}}{|\mathcal{I}_{\boldsymbol{\theta}}|}. \tag{4.14}$$

It is worth noting that for this particular problem, equation (2.13) is not satisfied. Therefore, no MVUE can be found through Theorem 2.1 and the bounds in equations (4.13) and (4.14) are not achieved.

[1] $x_l \in \{x \in \mathbb{R} : x = x_i - \frac{\Delta x}{2}, i = 1, \ldots, n\}$ and $x_u \in \{x \in \mathbb{R} : x = x_i + \frac{\Delta x}{2}, i = 1, \ldots, n\}$.

4.1 The Cramér-Rao Bounds under different Pixel Selection Schemes

From equation (4.12), it is natural to expect that different pixel selections ($\mathcal{J}$) determine different performance bounds. For example, it is reasonable to expect that if only the most-external pixels are employed for inference, little to none source flux shall be measured and, therefore, an imprecise estimator $\hat{\tilde{F}}$ would be gotten. This section aims to provide some insight on the effect of $\mathcal{J}$ on $\mathcal{I}_{\boldsymbol{\theta}}, \sigma^2_{\tilde{F}}$ and $\sigma^2_{\tilde{B}}$.

For this, three pixel selection schemes are studied through simulations. A "sequential" scheme shall refer to sequentially adding pixels from left to right, thus getting a sequence of sets given by $(\mathcal{J}_k) = \{\{1\}, \{1,2\}, \{1,2,3\} \ldots, \{1,\ldots,n\}\}$; an "aperture" scheme denotes that, starting from the pixel the source is located at (denoted by n_{x_c}), sequentially adding adjacent pixels (left- and right-pixel), obtaining a sequence of the form $(\mathcal{J}_k) = \{\{n_{x_c}\}, \{n_{x_c}-1, n_{x_c}, n_{x_c}+1\}, \{n_{x_c}-2, n_{x_c}-1, n_{x_c}, n_{x_c}+1, n_{x_c}+2\}, \ldots\}$; finally a "random" scheme denotes sequentially adding random pixels which have not been added yet. Note that the random scheme may be understood as a sequential scheme performed over a permutation of the full set of indices $\{1,\ldots,n\}$ as seen on Figure 4.1[2]. Note that the permutation presented in Figure 4.1 is the one considered for this analysis.

The parameters that characterize the source, device and sky conditions along this section are: $D = 0$, $RON = 5$ photo-e$^-$, $G = 2$ photo-e$^-$/ADU, $\Delta x = 0.2$ arcsec, $n = 41$ pixels, $f_s = 1502.5$ ADUs/arcsec, $n_{x_c} = 21$, $dither = 0$, $FWHM = 1.0$ arcsec and $\tilde{F} = 10002$ photo-e$^-$. The *dither* parameter expresses an offset between the $n^{th}_{x_c}$ pixel's center and the actual position of the point source x_c [Mendez et al., 2013, Mendez et al., 2014].

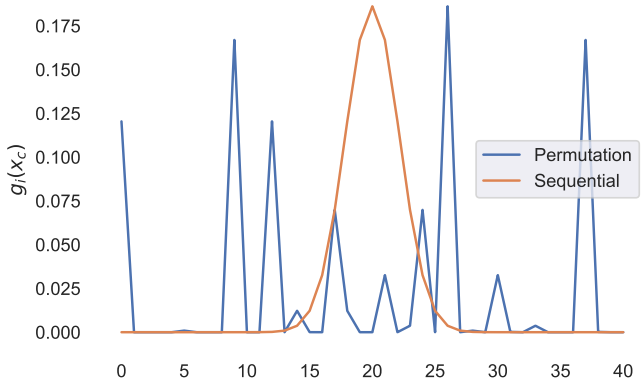

Figure 4.1: Quantified PSF[3], $g_i(x_c)$, and its permutation, which is employed for the random selection scheme.

Considering the three selection schemes and scenario above mentioned, Figure 4.2 shows the four elements of the Fisher information matrix, as described in equation (4.12), and its determinant $|\mathcal{I}_{\boldsymbol{\theta}}|$. It shows increasing trends that are expected for the problem of joint estimation of $\tilde{F}$ and $\tilde{B}$. Those curve shapes determine to some extent how the Cramér-Rao bounds curves behave.

[2]For accurate computation of the $g_i(x_c)$ values the mpmath [Johansson et al.,] *Python* library was used throughout this work.

[3]Also referred to as Pixel Response Function (PRF) [Handberg et al., 2021].

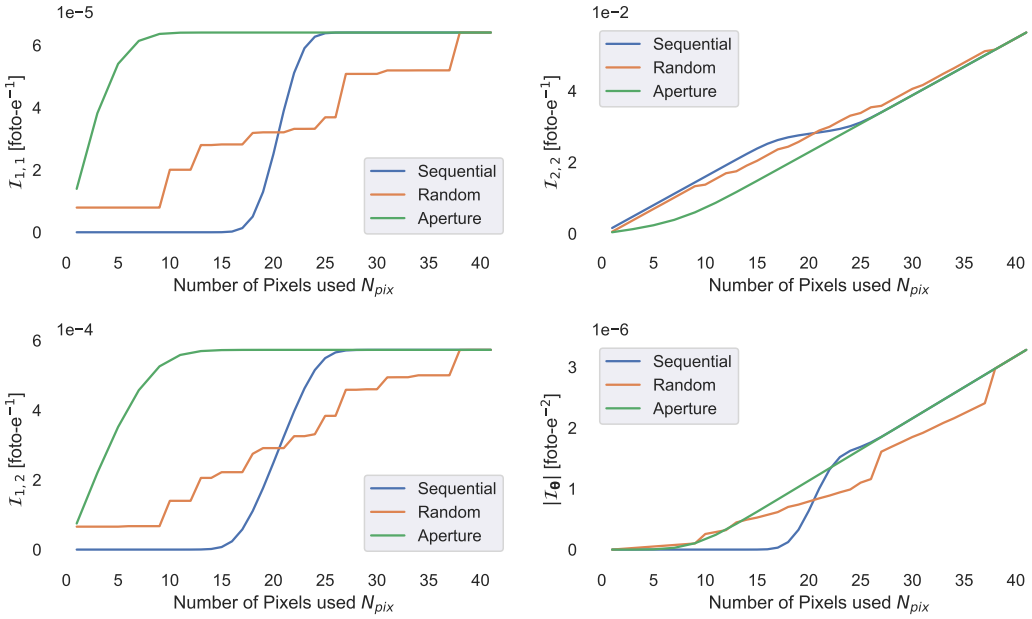

Figure 4.2: Fisher matrix elements and its determinant for different selection schemes.

Focusing on the upper-left graphic presented in Figure 4.2, the curve corresponding to the sequential scheme shows that the first ~ 15 pixels added contain no information about the source, because of the shape of the PSF on that region, since its value is 0 for all practical effects. Then, as pixels near the mode of the PSF are added (pixels that contain flux coming from the source), $\mathcal{I}_{1,1}$ increases rapidly, until it saturates, since no source flux is taken from the last-added observations. On the other hand, for the aperture scheme, $\mathcal{I}_{1,1}$ increases due to the increasing fraction of $\tilde{F}$ observed. This curve saturates as the last pixels added mostly measure background information. For the random case, what's most remarkable about the curve for $\mathcal{I}_{1,1}$ is that it tends to "jump" each time a pixel whose $g_i(x_c)$ value is relatively high is added. Moreover, the higher $g_i(x_c)$ is the more $\mathcal{I}_{1,1}$ increases.

Note that for any selection scheme, saturation of the elements in the Fisher matrix is a consequence of the coverage assumption of equation (2.5).

For the case of $\mathcal{I}_{2,2}$ depicted in the upper-right graphic on Figure 4.2, it happens the opposite of what is observed for $\mathcal{I}_{1,1}$. When pixels near the source are added, the slope of the curve decreases. Therefore one can conclude that those pixels give less information about the background due to the influence of $\tilde{F}$ on the statistics of the corresponding mean values $\lambda_i(x_c, \tilde{F})$. It is worth noting that in any of the three cases shown, $\mathcal{I}_{2,2}$ does not saturate. The main reason behind this behavior is the homogeneous background assumption across the field of view.

For the curves outside the diagonal of $\mathcal{I}_{\boldsymbol{\theta}}$, those curves resembles what was shown for $\mathcal{I}_{1,1}$. Again, this can be explained by the coverage assumption: note that both terms have the form $\sum_{i\in\mathcal{J}} \alpha_i g_i(x_c)$, which is clearly bounded considering $\sup_{i\in\mathcal{J}} |\alpha_i| < \infty$.

Finally, though the curves for $|\mathcal{I}_{\boldsymbol{\theta}}|$ may be difficult to interpret, the fact that they show a slope very similar to that seen for $\mathcal{I}_{2,2}$ (at least for the sequential and aperture schemes after ~ 25 pixels are added) allows to infer how the Cramér-Rao bounds curves behave. For that matter, since the

slopes of $\mathcal{I}_{2,2}$ and $|\mathcal{I}_{\boldsymbol{\theta}}|$ (eventually) become similar to each other, their ratio shall become constant at some point, too. On the other hand, since $\mathcal{I}_{1,1}$ saturates eventually and the determinant $|\mathcal{I}_{\boldsymbol{\theta}}|$ does not, it is reasonable to expect that the ratio $\mathcal{I}_{1,1}/|\mathcal{I}_{\boldsymbol{\theta}}|$ exhibits a monotonic decreasing behavior. Both mentioned fractions correspond precisely to the CRLBs shown in equations (4.13) and (4.14).

Before analysing the actual behavior of the CRLBs, let us introduce some concepts and notation. For ease of visualization, it may be convenient to express the Cramér-Rao bound for flux $\tilde{F}$ in terms of magnitudes, rather than directly in photo-e$^-$. The corresponding standard deviation is computed as [Mendez et al., 2014]:

$$\sigma_m = \frac{2.5}{2} \cdot \left(\log\left(\tilde{F} + \sigma_{\tilde{F}}\right) - \log\left(\tilde{F} - \sigma_{\tilde{F}}\right) \right). \tag{4.15}$$

One key difference between the Cramér-Rao Lower Bound for a parameter vector $\boldsymbol{\theta} = (\theta_1, \ldots, \theta_m)$ and the bound for the one-dimensional problem of estimating just one of these parameters, is that the former takes into account how the uncertainty on each parameter shall impact on the others [Kay, 1993]. For the joint estimation problem adressed here, if the determination of $\tilde{B}$ is complete, the corresponding CRLB for $\tilde{F}$, denoted here as $\sigma^2_{\tilde{F},1D}$, is:

$$\sigma^2_{\tilde{F},1D} = \frac{1}{\mathcal{I}_{1,1}}, \tag{4.16}$$

where $\mathcal{I}_{1,1}$ is just the Fisher information matrix element described in equation (4.12)[45]. The statistical interaction between components is captured (to some extent) by the off-diagonal elements of the Fisher Information matrix, and therefore the "optimal" covariance matrix, $\mathcal{I}_{\boldsymbol{\theta}}^{-1}$. With the problem of jointly estimating $\tilde{F}$ and $\tilde{B}$ as example, if $\mathcal{I}_{1,2} = 0$ it follows that:

$$\sigma^2_{\tilde{F}} = \frac{\mathcal{I}_{2,2}}{\mathcal{I}_{1,1} \cdot \mathcal{I}_{2,2} - 0} = \frac{1}{\mathcal{I}_{1,1}} = \sigma^2_{\tilde{F},1D}, \tag{4.17}$$

$$\sigma^2_{\tilde{B}} = \frac{\mathcal{I}_{1,1}}{\mathcal{I}_{1,1} \cdot \mathcal{I}_{2,2} - 0} = \frac{1}{\mathcal{I}_{2,2}} = \sigma^2_{\tilde{B},1D}, \tag{4.18}$$

and, for the covariances:

$$[\mathcal{I}_{\boldsymbol{\theta}}^{-1}]_{1,2} = [\mathcal{I}_{\boldsymbol{\theta}}^{-1}]_{2,1} = \frac{-\mathcal{I}_{1,2}}{\mathcal{I}_{1,1} \cdot \mathcal{I}_{2,2} - \mathcal{I}_{1,2}^2} = 0. \tag{4.19}$$

Therefore $\mathcal{I}_{1,2}$ captures codependency among the estimators and in case that $\mathcal{I}_{1,2} = 0$, these become uncorrelated[6]. If that were the case, one could consider that the estimation problems can

[4] Analogously, the bound for $\tilde{B}$ when $\tilde{F}$ and all the other parameters are assumed known corresponds to $\sigma^2_{\tilde{B},1D} = \frac{1}{\mathcal{I}_{2,2}}$.

[5] Precisely because of this interaction and the definition of the Fisher information matrix it happens that the term $\mathcal{I}_{1,1}$ appears in other related problems and analyses [Mendez et al., 2014, Lobos et al., 2015].

[6] Though not necessarily independent.

be decoupled and treated separately, since the two-dimensional problem and the one-dimensional problems behave the same in terms of MSE. Therefore, the fractional difference or *discrepancy* between the corresponding bounds for the joint and one-dimensional problems (defined in equations (4.20) and (4.21)) measure how much the bounds deteriorate as dimensionality of the estimation problem increases or less information is available.

$$\Delta^{1D}\sigma_m \equiv \frac{\sigma_m - \sigma_{m,1D}}{\sigma_m} \times 100, \tag{4.20}$$

$$\Delta^{1D}\sigma_{\tilde{B}} \equiv \frac{\sigma_{\tilde{B}} - \sigma_{\tilde{B},1D}}{\sigma_{\tilde{B}}} \times 100. \tag{4.21}$$

This two quantities are dimensionless and non-negative.

That said, Figure 4.3 shows the corresponding performance bounds obtained through the depicted selection schemes. The top graphics show both the bounds for the joint case and their one-dimensional counterpart, while the bottom graphics display those results in the form of discrepancies.

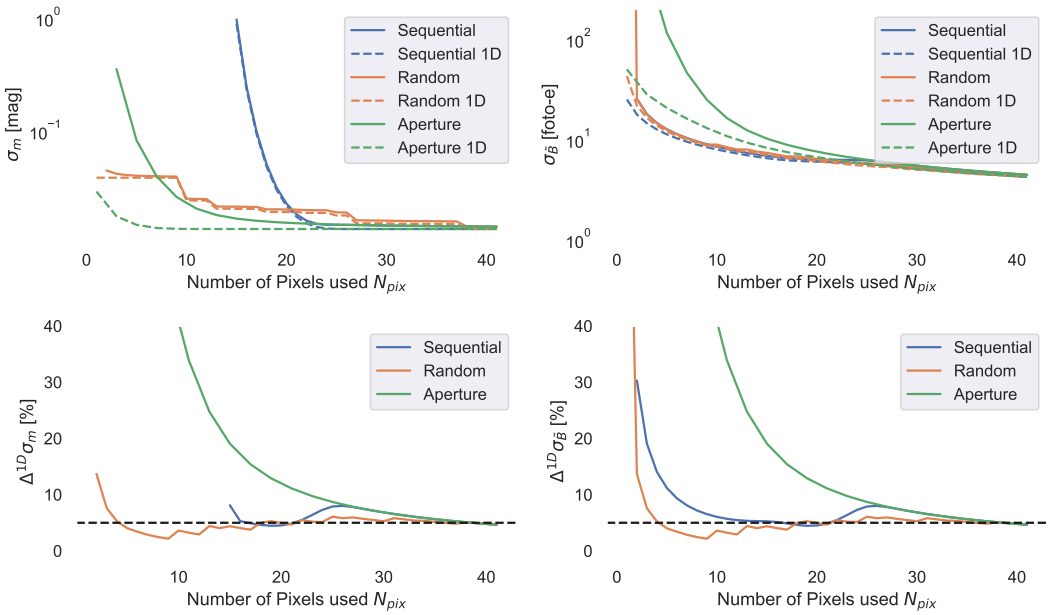

Figure 4.3: Performance bounds for joint source flux and background estimation under different pixel selection schemes. For the upper-left and -right graphics, a solid line is used for the bounds for the joint estimation problem, σ_m^2 and $\sigma_{\tilde{B}}^2$, and a dashed line for the corresponding one-dimensional bounds, $\sigma_{m,1D}^2$ and $\sigma_{\tilde{B},1D}$. The black dashed line on the lower-left and -right graphics indicates a 5% discrepancy.

The way each selection scheme affects the bounds behave as expected:

- For the sequential scheme, very high uncertainty for $\tilde{F}$ is expected at first since no source flux is measured, followed by a rapid decrease that ends up stabilizing as only background pixels

are added. For $\sigma_{\tilde{B}}$, as no source is measured at first, the sequential scheme outperforms the other two, and decrease continuously as more pixel information is considered.

- The aperture scheme allows σ_m and $\sigma_{m,1D}$ to decrease earlier, in comparison with the sequential one. However, this scheme requires much more pixels to yield an estimation for $\tilde{B}$ that is as precise as the sequential scheme.
- The random scheme can be thought to be a intermediate case between the other two schemes, in the sense that it attains relatively good precision with less information by means of taking into account both pixels that contain a significant proportion of flux and pixels that measure only background.

It is remarkable that as more information (pixels) is added, the bounds decrease further, just as predicted from the analysis of the elements of the Fisher matrix. This is observed in any of the selection schemes and for both the joint estimation and the one-dimensional estimators.

It should be kept in mind however, that the results for the random scheme and discrepancy may be misleading. Though that scheme seems to offer relatively low discrepancies and yet good performance bounds, it's not a "good" scheme in the sense that as more pixels are added it ends up behaving as other simpler schemes. This behavior is attributed to the fact that apparent performance gains with respect to other schemes rely mostly on the randomness of the selection. Furthermore, performing some stochastic optimization mechanism to ensure a good balance between both parameters' uncertainties would require knowing the parameters themselves to optimize the bounds (*i.e.*, calculation of $\mathcal{I}_{\boldsymbol{\theta}}$) and to restrict the problem, since it is already evidenced that using every pixel available leads to optimality over N_{pix}. On the other hand, the discrepancy obtained through the random scheme shows itself going even below the 5% discrepancy level, even for small values of N_{pix}. If the one-dimensional bound were constant, it would be an indicator that better precision is achieved, but this is not the case, since discrepancy shows convergence to a constantly-decreasing value. For example, the precision attained with the random scheme at $N_{pix} = 10$ is clearly worse than that obtained with $N_{pix} = 41$, though discrepancy is deteriorated in that latter case.

Further evidence on that considering all the pixels available for inference is preferable is shown in Figure 4.4. It illustrates how the best attainable estimators become less correlated as N_{pix} increases. It also proves that $\hat{\tilde{F}}$ and $\hat{\tilde{B}}$ are negatively correlated, implying that there's a trade-off when estimating both parameters, which emerges as a consequence of fitting the PSF into noisy data.

This behavior can be explained in a natural manner when inspecting the covariance term $[\mathcal{I}_{\boldsymbol{\theta}}^{-1}]_{1,2}$. Resorting to the approximation $\mathcal{I}_{1,2} \propto \mathcal{I}_{2,2}$ (for some N_{pix} sufficiently large) it follows that:

$$[\mathcal{I}_{\boldsymbol{\theta}}^{-1}]_{1,2} \approx \frac{-\mathcal{I}_{1,2}}{\mathcal{I}_{1,1} \cdot c \cdot \mathcal{I}_{1,2} - \mathcal{I}_{1,2}^2} = \frac{-1}{c \cdot \mathcal{I}_{1,1} - \mathcal{I}_{1,2}}, \tag{4.22}$$

with c some proportionality constant. For $c \cdot \mathcal{I}_{1,1}$ sufficiently large, the denominator in equation (4.22) decreases and the covariance increases as consequence. Therefore, as estimations become less correlated, the more the joint estimation problem resembles the two decoupled problems. As a consequence of this resemblance between problems discrepancies reduce.

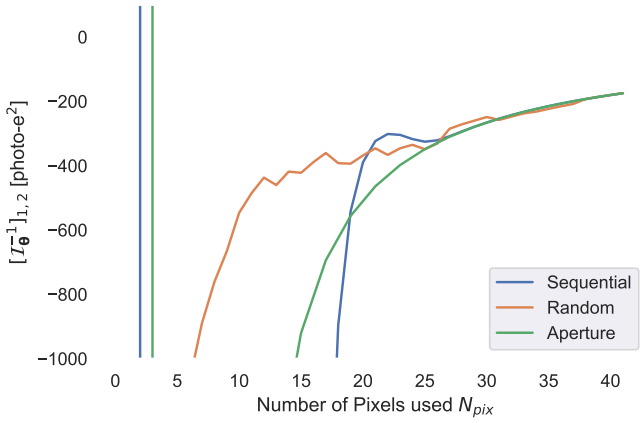

Figure 4.4: Off-diagonal element of $I_{\boldsymbol{\theta}}^{-1}$ for different selections schemes.

One can contrast these findings with the SNR calculated for each of the selection schemes proposed, which are shown in Figure 4.5. It is shown that for any of the selection schemes the SNR dampens though Figure 4.3 exhibits that minimal bounds have been reached and discrepancies converged to 5%. What's most interesting is the fact that at $N_{pix} \sim 10$ the bounds given by the aperture and random scheme are shown to reach approximately the same value, while the discrepancies differ significantly, and so does the SNR, since the aperture for the former is near its maximum while the random scheme goes below 20. This figure exemplifies that the SNR may not be a good predictor of the best achievable performance for an unbiased estimator, since it depends mostly on the selection scheme rather than the observed object or device themselves.

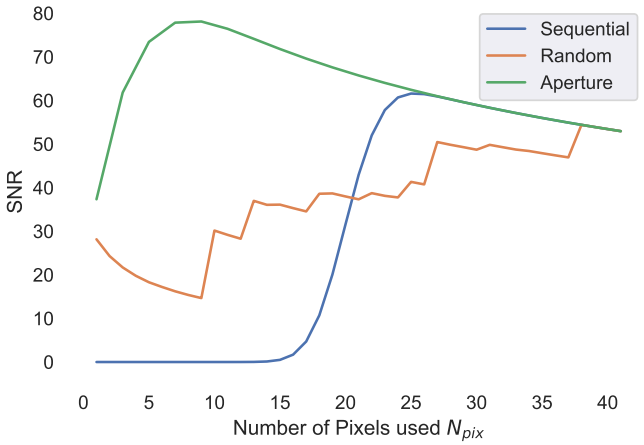

Figure 4.5: SNR for different selection schemes as more pixels are included.

To illustrate that these findings do apply further for other seeing conditions Figures 4.6, 4.7 and 4.8 resemble Figures 4.3, 4.4 and 4.5, respectively, where each curve shown differs from the already discussed base case in only one parameter (specified in the curve's label). Note that an aperture selection scheme was employed for all curves in Figures 4.6, 4.7 and 4.8. As can be seen, these Figures do not present substantial differences with respect to the base case discussed above, leading to the same conclusions.

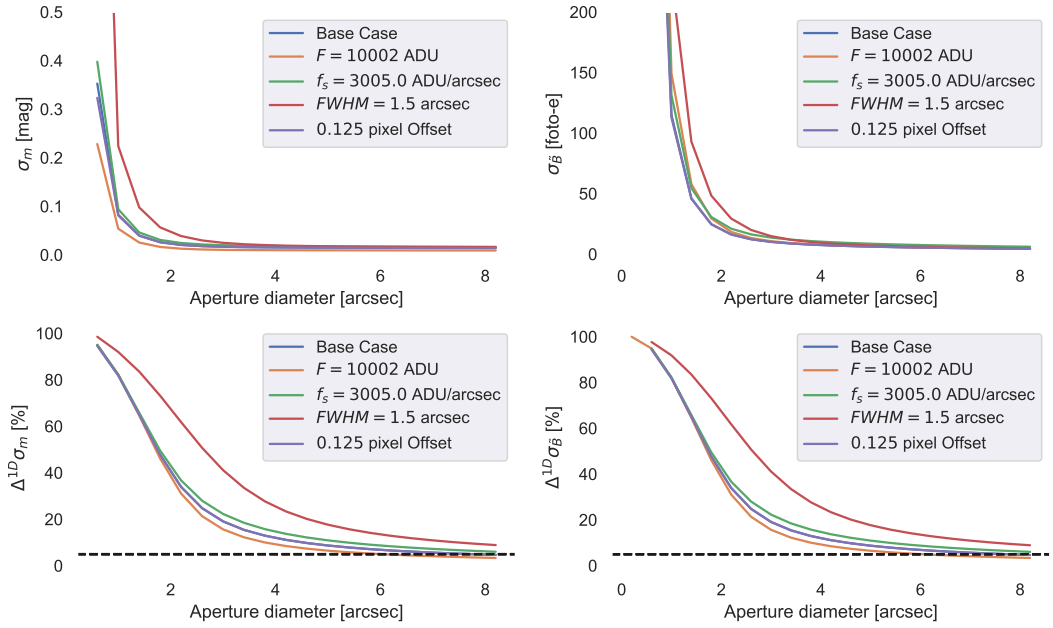

Figure 4.6: Performance bounds (top) and discrepancies (bottom) for joint source flux and background estimation for different observational scenarios, under an aperture pixel selection scheme.

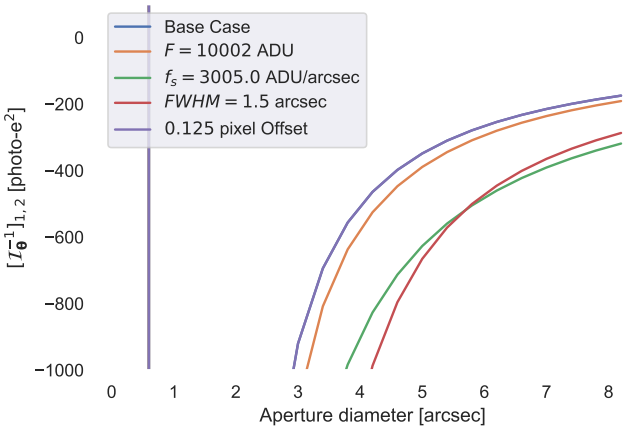

Figure 4.7: Off-diagonal element of $\mathcal{I}_{\boldsymbol{\theta}}^{-1}$ for different observational scenarios, under an aperture pixel selection scheme.

4.2 Effect of Device Resolution on Cramér-Rao Lower Bounds

Up to this point it has been discussed mostly the effects of source's parameters, sky conditions and information selection on the behavior of the fundamental bounds given by Theorem 2.1. In this section, the interaction between some of these parameters and the resolution of the device, Δx, is explored and how these interactions translates to the Cramér-Rao bounds.

Though source's position has been assumed known, it becomes interesting to study whether or not the findings on the effects of dithering seen on previous work [Mendez et al., 2014] do apply to the problem posed here.

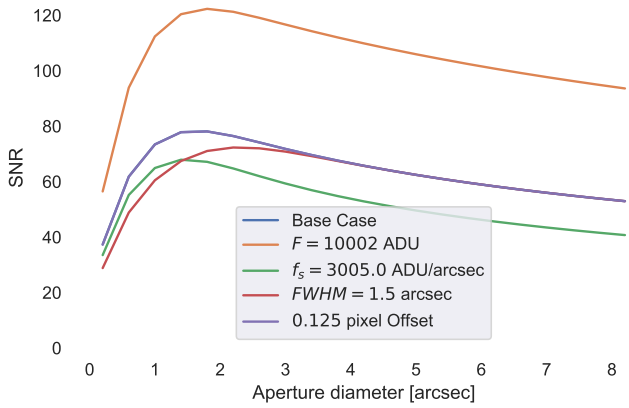

Figure 4.8: SNR for different observational scenarios, under an aperture pixel selection scheme.

The parameters considered for this analysis are the same employed in Section 4.1, but with $\Delta x \in (0, 2]$ and an observation dither ranging from 0 pixel offset and 0.9 pixel offset; and the bounds are computed using each one of the $n = 41$ pixels of the array. It is important then to note that, since the total amount of pixels in the array is considered fixed, as Δx grows the source becomes covered by fewer pixels and sky coverage increases.

Then again, Figure 4.9 shows the performance bounds as the resolution decreases, for different values of dithering; and the corresponding discrepancies with respect to the one-dimensional bounds. For the case of source flux (top-left and bottom-left in the figure), it seems that as long as $\Delta x < FWHM$ the Cramér-Rao bounds are not significantly hindered by the lowering resolution of the device. Beyond that value emerges some sort of symmetry, which translates into that photometry is better done near pixel centers than pixel boundaries [Mendez et al., 2014]. Said symmetry does apply both for the bound for flux itself and for discrepancy, which reinforces the idea of good centering for photometry.

For background estimation (top-right and bottom-right in Figure 4.9), the CRLB is more resilient to dithering than source flux estimation, as the different curves show negligible differences among them. It is worth noting that this is not the case for discrepancy, as it shows the same symmetry effect that source brightness exhibits. This behavior is probably due to the correlation that emerges when simultaneously estimating $\tilde{F}$ and $\tilde{B}$. Some insight into this behavior is provided by Figure 4.10, which shows how dithering affects the covariance given by the matrix $I_{\boldsymbol{\theta}}^{-1}$. As can be seen, when a source is positioned near the boundaries of a pixel, the covariance tends to grow larger in magnitude, thus the two-dimensional bound grows apart from the one-dimensional one and increasing discrepancy.

One final remark on what is observed in Figure 4.9 is that, after a rapid decrease of $\sigma_{\tilde{B}}$, it behaves like a square-root. This can be explained simply by noting the linear relation between $\tilde{B}$ and Δx of equation (4.4), meaning that the contribution of $\tilde{B}$ to the variance of each observation I_i also grows linearly with Δx, since larger pixels are prone to measure more noise coming from the sky.

The discussion and observations made for Figures 4.9 and 4.10 do apply for other source's profiles, as can be seen from Figures 4.11 and 4.12, which resemble Figure 4.9 but considering

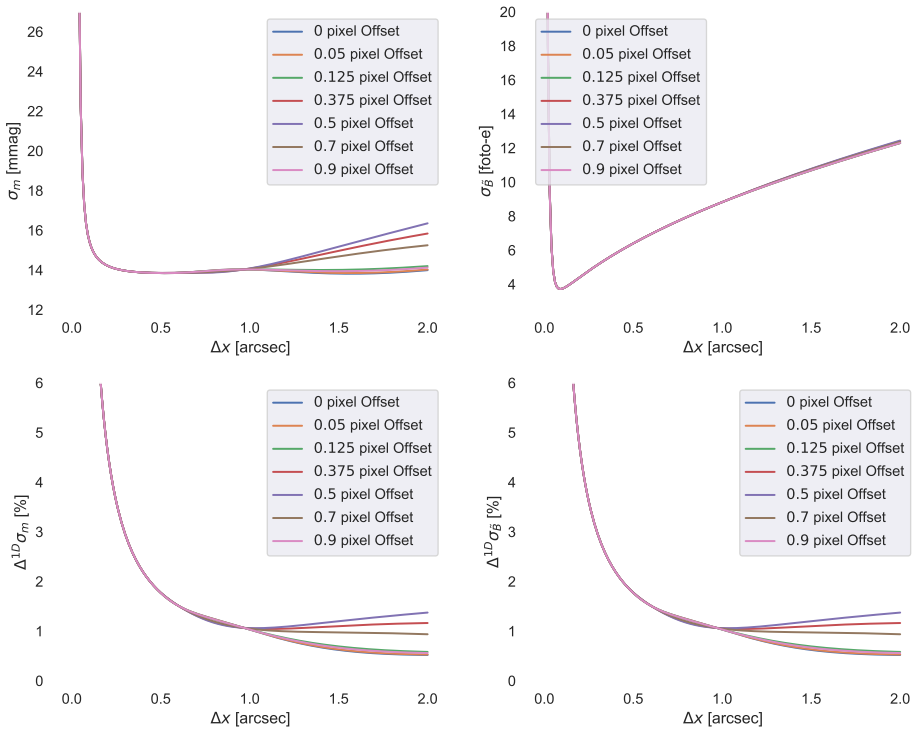

Figure 4.9: Performance bounds (top) and discrepancies (bottom) for joint source flux and background estimation for different centering configurations, as functions of pixel size Δx.

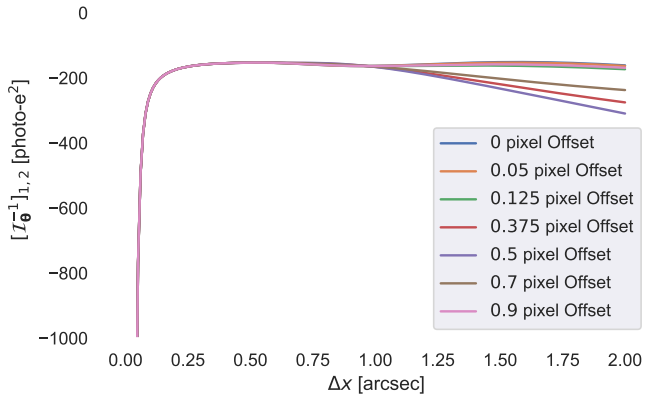

Figure 4.10: Off-diagonal element of $\mathcal{I}_{\boldsymbol{\theta}}^{-1}$ for different centering configurations, as a function of pixel size Δx.

$FWHM = 0.5''$ and $FWHM = 1.5''$, respectively.

Going further on this analysis, this time varying Δx for different values of total flux (fixing again $FWHM = 1.0''$), Figure 4.13 shows the bounds obtained and their corresponding discrepancies for $\tilde{F} \in \{1080, 3324, 20004, 60160\}$. In the figure's top-left graphic it is shown that, for reasonable resolutions, photometry is quite robust in the sense that the bound remains practically constant (though, more precisely, it tends to become less precise as Δx increases). It may seem counterintuitive that brighter sources lead to lower bounds, following the same argument said

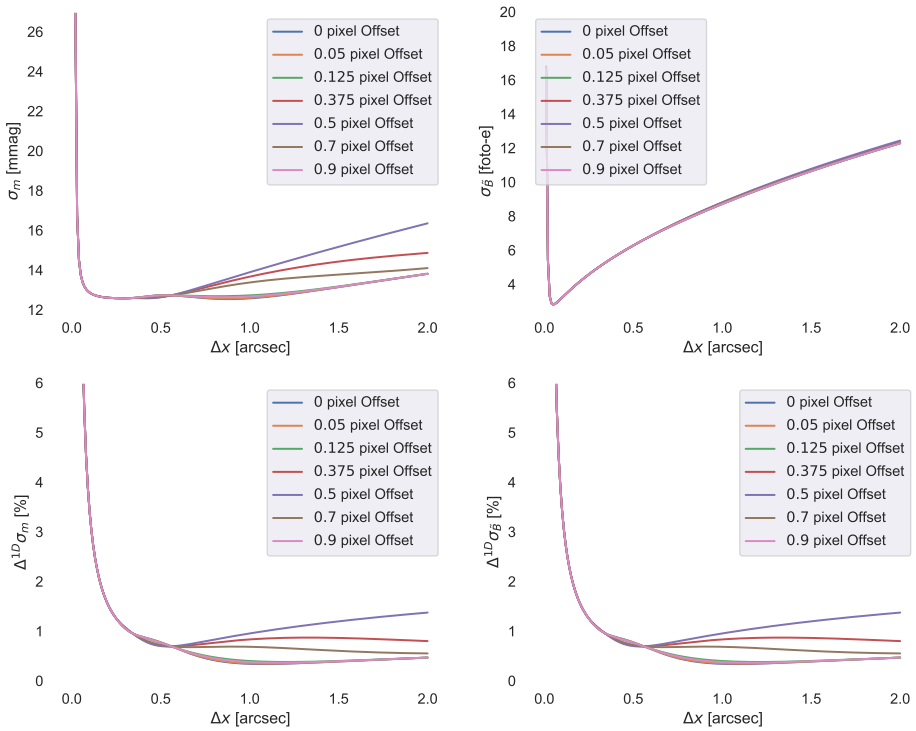

Figure 4.11: Performance bounds (top) and discrepancies (bottom) for joint source flux and background estimation for different centering configurations, as functions of pixel size Δx, $FWHM = 0.5''$.

above that increasing the variance of the observations I_i, given by $\lambda_i(x_c, \tilde{F}) = \tilde{F} \cdot g_i(x_c) + \tilde{B}$, turns into an increase of the estimator's (expected) variance. The reasoninng behind this seemingly odd behavior is the logarithmic transformation given by equation (4.15) when parsing photo-e$^-$ into magnitudes.

On the other hand, the discrepancy between σ_m and $\sigma_{m,1D}$ behaves differently, as it is shown almost as a decreasing function of Δx, specially for fainter sources. The reasoning behind this is that of the one-dimensional bound gets worsen more rapidly than the two-dimensional one as pixel size increases. As an alternative explanation of this behavior, it could be stated that, if correlation decreased in magnitude, it would be expected that discrepancy did it as well. But, as Figure 4.14 shows, this is not the case. Therefore, the fainting discrepancy is a consequence of the decreasing precision, both for the one- and two-dimensional cases.

It should also be remarked that brighter sources tend to exhibit more anticorrelation between the optimal estimators, compared to fainter sources.

For the case of $\sigma_{\tilde{B}}$, Figure 4.13 shows no significant effect of $\tilde{F}$ on said bound. Its behavior is mostly explained by the same arguments presented above.

Fixing $\tilde{F} = 10002$ photo-e$^-$, Figures 4.15 and 4.16 show that similar explanations as the aforementioned do apply under different sky conditions. It is worth noting that, as could be expected, when the sky brightness is higher the problem becomes more complex, in the sense that both the covariance and the bounds, hence the attainable MSE, increase in magnitude.

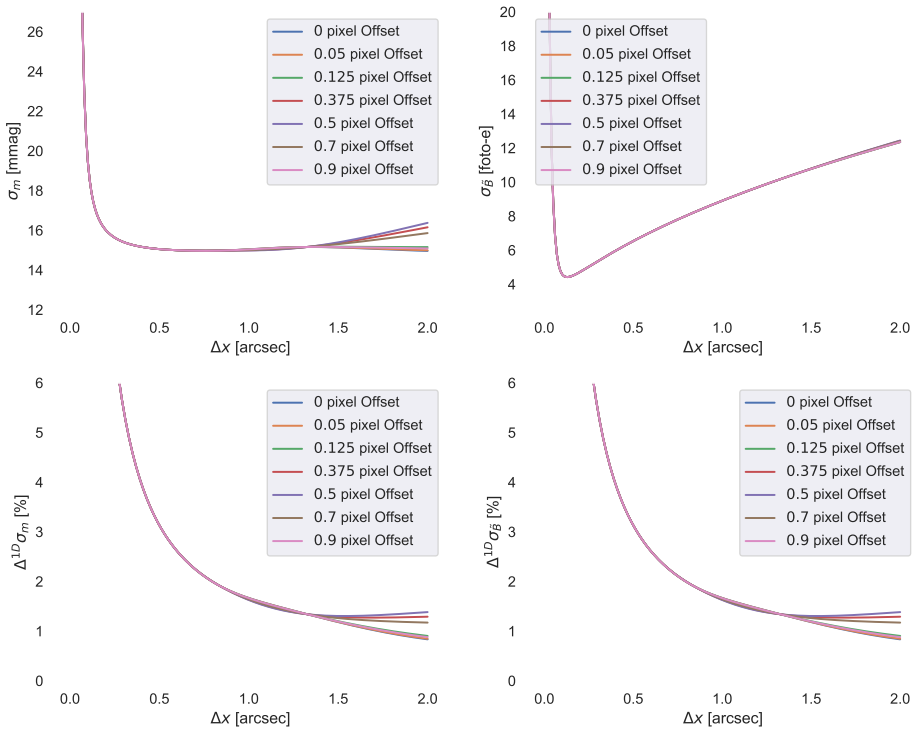

Figure 4.12: Performance bounds (top) and discrepancies (bottom) for joint source flux and background estimation for different centering configurations, as functions of pixel size Δx, $FWHM = 1.5''$.

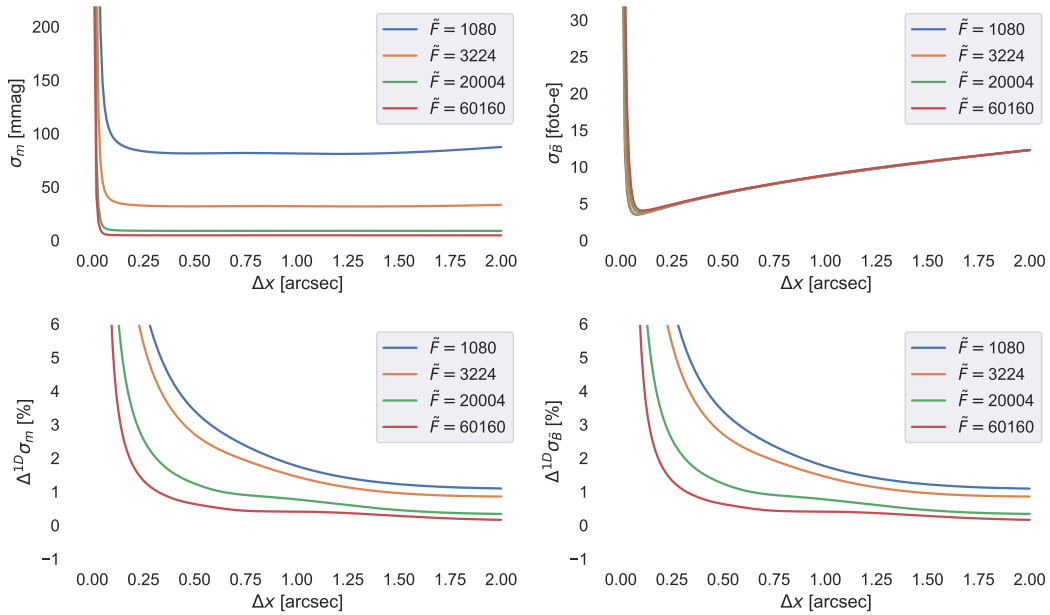

Figure 4.13: Performance bounds (top) and discrepancies (bottom) for joint source flux and background estimation for different source brightness, as functions of pixel size Δx.

4.3 MVUE and its Achievability

After studying the fundamental properties of the posed joint estimation problem and having stated the theoretical benefits of employing as much pixel information as possible, the question of how to

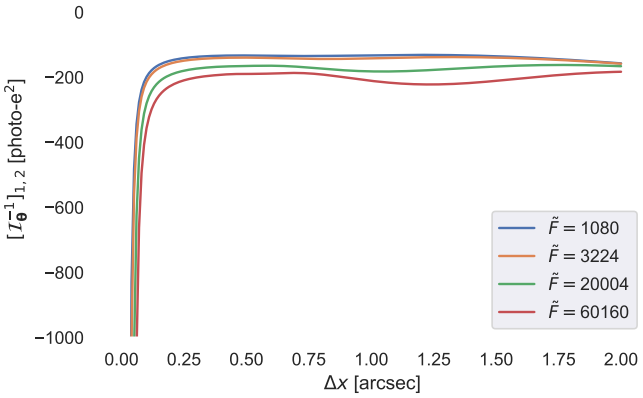

Figure 4.14: Off-diagonal element of $\mathcal{I}_{\boldsymbol{\theta}}^{-1}$ for different source brightness, as a function of pixel size Δx.

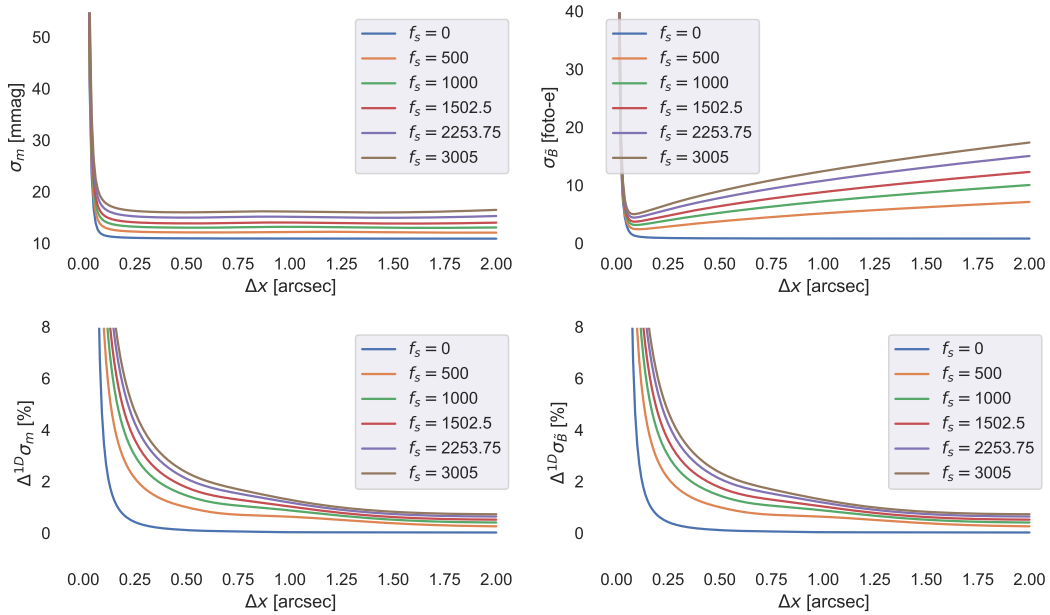

Figure 4.15: Performance bounds (top) and discrepancies (bottom) for joint source flux and background estimation for different sky conditions, as functions of pixel size Δx.

implement such an estimation scheme arises.

The natural first attempt to answer that question is to draw upon Theorem 2.1, more specifically its equation (2.13), since if such a function $\mathbf{h}$ is found, it is the optimal decision rule under the minimal MSE criterion.

Unfortunately, such a function could not be found, at least not in a vectorial form. To show that, it suffices to write equation (2.13) for this problem:

$$\begin{bmatrix} \sum_{i=1}^{n} \frac{g_i(x_c)}{\lambda_i(x_c,\tilde{F})} \cdot I_i - 1 \\ \sum_{i=1}^{n} \frac{1}{\lambda_i(x_c,\tilde{F})} \cdot I_i - n \end{bmatrix} = \mathcal{I}_{\boldsymbol{\theta}} \begin{bmatrix} h_1(\mathbf{I}) - \tilde{F} \\ h_2(\mathbf{I}) - \tilde{B} \end{bmatrix}, \tag{4.23}$$

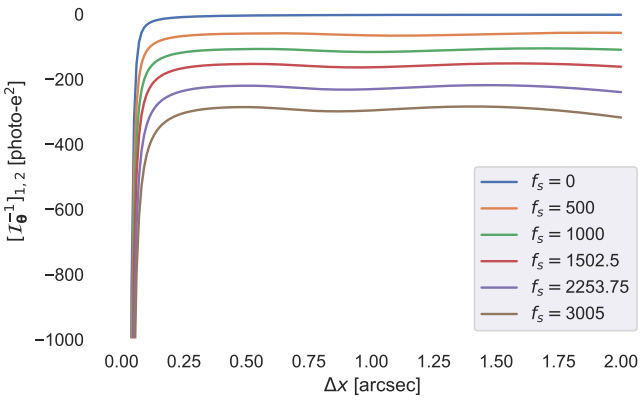

Figure 4.16: Off-diagonal element of $\mathcal{I}_{\boldsymbol{\theta}}^{-1}$ for different sky conditions, as a function of pixel size Δx.

where $\mathcal{I}_{\boldsymbol{\theta}}$ is the Fisher Information matrix presented in equation (4.12) and the coverage assumption has been considered when calculating the LHS. If $\mathcal{I}_{\boldsymbol{\theta}}^{-1}$ does exists, then

$$\mathbf{h}(\mathbf{I}) = \begin{bmatrix} h_1(\mathbf{I}) \\ h_2(\mathbf{I}) \end{bmatrix} = \mathcal{I}_{\boldsymbol{\theta}}^{-1} \begin{bmatrix} \sum_{i=1}^{n} \frac{g_i(x_c)}{\lambda_i(x_c, \tilde{F})} \cdot I_i - 1 \\ \sum_{i=1}^{n} \frac{1}{\lambda_i(x_c, \tilde{F})} \cdot I_i - n \end{bmatrix} + \begin{bmatrix} \tilde{F} \\ \tilde{B} \end{bmatrix}, \tag{4.24}$$

which explicitly depends on the parameters to be estimated, leading to a contradiction. Therefore, the CRLBs cannot be achieved and the theory depicted in Section 2.3 poses as a possibility to find the decision rule that leads to the MVUE, specially when recalling that the Poisson distribution belongs to the exponential family of probability distributions.

In order to find a candidate for sufficient statistic for $(\tilde{F}, \tilde{B})$ Theorem 2.2 must be recalled. In other words, the likelihood described in equation (2.7) must be factorized in the form of equation (2.16). The likelihood can be written as:

$$p(\mathbf{I}|x_c, \tilde{F}, \tilde{B}) = \prod_{i=1}^{n} e^{\tilde{F} \cdot g_i(x_c) + \tilde{B}} \cdot \prod_{i=1}^{n} \left(\tilde{F} \cdot g_i(x_c) + \tilde{B} \right)^{I_i} \cdot \prod_{i=1}^{n} \frac{1}{I_i!}. \tag{4.25}$$

Therefore, $h(\cdot)$ can be identified as $h(\mathbf{I}) = \prod_{i=1}^{n} 1/I_i!$. Additionally, since the leftmost product in the RHS of equation (4.25) does not depend on the observation vector $\mathbf{I}$, the statistic $T(\mathbf{I})$ must be found from $\prod_{i=1}^{n} (\tilde{F} \cdot g_i(x_c) + \tilde{B})^{I_i}$.

Unfortunately, the observations $I_1, \ldots, I_n$ could not be arithmetically separated from the parameters $\tilde{F}$ and $\tilde{B}$. Therefore the MVUE could not be found here with the framework provided by Theorems 2.2 and 2.3.

Finally, the nonachievability of the CRLBs and the absence of an explicit MVUE, at least by means of a sufficient statistic, support the adoption of *alternative criteria* to tackle the joint estimation problem. Further justification is that the nonachievability of the Cramér-Rao Lower

Bounds does not exclude the possibility that they can be approximated arbitrarily close by practical estimators. The following sections focus on assessing the optimality (or non-optimality) of two well adopted and popular estimation schemes: the Weighted Least-Squares (WLS) and the Maximum Likelihood (ML) estimators. This follows previous works by [Lobos et al., 2015, Espinosa et al., 2018].

Chapter 5

WLS Estimator for Joint Source Flux and Background Estimation

Let $\mathcal{J} \subseteq \{1, \ldots, n\}$ be a set of indices and $\{w_i\}_{i=1}^n$ be a set of weights which defines a cost function given by

$$J_{WLS}(\boldsymbol{\alpha}, \mathbf{I}) = \sum_{i \in \mathcal{J}} w_i (I_i - \alpha_1 \cdot g_i(x_c) - \alpha_2)^2, \tag{5.1}$$

where $\boldsymbol{\alpha} \in \boldsymbol{\Theta}$. Such function implicitly defines the Weighted Least-Squares estimator $\tau_{WLS}(\mathbf{I})$ just as in equation (3.1), *i.e.*,

$$\tau_{WLS}(\mathbf{I}) = \underset{\boldsymbol{\alpha} \in \boldsymbol{\Theta}}{\operatorname{argmin}} J_{WLS}(\boldsymbol{\alpha}, \mathbf{I}). \tag{5.2}$$

Fortunately, the minimization problem of equation (5.2) can be algebraically solved into the form of a linear estimator. Therefore, the WLS estimator $\tau_{WLS}(\mathbf{I})$ is given by

$$\begin{aligned} \tau_{WLS}(\mathbf{I}) &= \begin{bmatrix} \sum_{i \in \mathcal{J}} w_i \cdot g_i^2(x_c) & \sum_{i \in \mathcal{J}} w_i \cdot g_i(x_c) \\ \sum_{i \in \mathcal{J}} w_i \cdot g_i(x_c) & \sum_{i \in \mathcal{J}} w_i \end{bmatrix}^{-1} \cdot \begin{bmatrix} w_{i_1} \cdot g_{i_1}(x_c) & \ldots & w_{i_{|\mathcal{J}|}} \cdot g_{i_{|\mathcal{J}|}}(x_c) \\ w_{i_1} & \ldots & w_{i_{|\mathcal{J}|}} \end{bmatrix} \cdot \mathbf{I} \\ &= -[\nabla^{20} J_{WLS}(\tau_{WLS}(\bar{\mathbf{I}}), \bar{\mathbf{I}})]^{-1} \cdot \nabla^{11} J_{WLS}(\tau_{WLS}(\bar{\mathbf{I}}), \bar{\mathbf{I}}) \cdot \mathbf{I}. \end{aligned} \tag{5.3}$$

As $\tau_{WLS}(\mathbf{I})$ is a linear estimator, its mean vector $\bar{\tau}_{WLS}$ and covariance matrix $\mathbf{C}_{\tau_{WLS}}$ can also be expressed in closed-form. Those moments are given by:

$$\begin{aligned} \bar{\tau}_{WLS} &= -[\nabla^{20} J_{WLS}(\tau_{WLS}(\bar{\mathbf{I}}), \bar{\mathbf{I}})]^{-1} \cdot \nabla^{11} J_{WLS}(\tau_{WLS}(\bar{\mathbf{I}}), \bar{\mathbf{I}}) \cdot \bar{\mathbf{I}} \\ &= \tau'_{WLS}(\bar{\mathbf{I}}) \cdot \bar{\mathbf{I}}. \end{aligned} \tag{5.4}$$

$$\mathbf{C}_{\tau_{WLS}} = \tau'_{WLS}(\bar{\mathbf{I}}) \cdot Cov(\mathbf{I}) \cdot \left[\tau'_{WLS}(\bar{\mathbf{I}})\right]^{\intercal}. \tag{5.5}$$

5.1 Numerical Analysis

Since the estimator $\tau_{WLS}(\cdot)$ can be found in an explicit form, it is possible to directly compute in an experimental setting both its expectation and its covariance matrix, therefore the variances for $\hat{\tilde{F}}$ and $\hat{\tilde{B}}$. For that matter, some useful definitions can be introduced: the performance discrepancies of an explicit estimator $\tau_J(\mathbf{I})$, $\Delta\sigma_m$, $\Delta\sigma_{\tilde{B}}$, and its relative biases, $\varepsilon_{\tilde{F}}$, $\varepsilon_{\tilde{B}}$, are defined as follows:

$$\begin{aligned}\Delta\sigma_m &= \frac{\frac{2.5}{2} \cdot \left(\log\left(\tilde{F} + \sqrt{Var(\tau_{J,1}(\mathbf{I}))}\right) - \log\left(\tilde{F} - \sqrt{Var(\tau_{J,1}(\mathbf{I}))}\right)\right) - \sigma_m}{\sigma_m} \times 100 \\ &= \frac{\frac{2.5}{2} \cdot \left(\log\left(\tilde{F} + \sqrt{[\mathbf{C}_{\tau_J}]_{1,1}}\right) - \log\left(\tilde{F} - \sqrt{[\mathbf{C}_{\tau_J}]_{1,1}}\right)\right) - \sigma_m}{\sigma_m} \times 100,\end{aligned} \tag{5.6}$$

$$\begin{aligned}\Delta\sigma_{\tilde{B}} &= \frac{\sqrt{Var(\tau_{J,2}(\mathbf{I}))} - \sigma_{\tilde{B}}}{\sigma_{\tilde{B}}} \times 100 \\ &= \frac{\sqrt{[\mathbf{C}_{\tau_J}]_{2,2}} - \sigma_{\tilde{B}}}{\sigma_{\tilde{B}}} \times 100,\end{aligned} \tag{5.7}$$

$$\varepsilon_{\tilde{F}} = \frac{\left|\mathbb{E}_{\mathbf{I}\sim p(\mathbf{I}|\boldsymbol{\theta})}\{\tau_{J,1}(\mathbf{I})\} - \tilde{F}\right|}{\tilde{F}} \times 100, \tag{5.8}$$

$$\varepsilon_{\tilde{B}} = \frac{\left|\mathbb{E}_{\mathbf{I}\sim p(\mathbf{I}|\boldsymbol{\theta})}\{\tau_{J,2}(\mathbf{I})\} - \tilde{B}\right|}{\tilde{B}} \times 100, \tag{5.9}$$

where both the moments of $\tau_J(\mathbf{I})$ and the Cramér-Rao Bounds, σ_m and $\sigma_{\tilde{B}}$, are computed over the same set of indices $\mathcal{J}$. It is also worth noting that for the WLS estimator, $\tau_{WLS}(\cdot)$, the set of weights $\{w_i\}_{i=1}^n$ is fixed when calculating these quantities.

Unless specified otherwise, the parameters to be considered for the following simulations are $D = 0$, $RON = 5$ photo-e$^-$, $G = 2$ photo-e$^-$/ADU, $\Delta x = 0.2$ arcsec, $n = 41$ pixels, $f_s = 1502.5$ ADUs/arcsec, $n_{x_c} = 21$, $dither = 0$, $FWHM = 1.0$ arcsec, $\tilde{F} \in \{1080, 3224, 20004, 60160\}$ photo-e$^-$ and $\mathcal{J} = \{1, \ldots, n\}$. This last choice for $\mathcal{J}$ is due to the results presented in the previous section, as more information may allow to more precise and less correlated estimations $\hat{\tilde{F}}$ and $\hat{\tilde{B}}$.

5.1.1 Effect of Weight Selection

A key element of the Weighted Least-Squares estimator, and one that may considerably hinder the estimator's performance, is the weight set $\{w_i\}_{i=1}n$ employed for estimation. Therefore, it

is important to study how the estimator's statistical behavior is affected by the weight selection, which can lead to a guidance on how to properly choose the weights.

For example, it can be shown that if the weights are chosen such that:

$$w_i = \frac{K}{\lambda_i(x_c, \tilde{F})}, \quad \forall i \in \{1, \ldots, n\}, \tag{5.10}$$

where $K > 0$ is an arbitrary constant, then the covariance matrix of $\tau_{WLS}(\mathbf{I})$ equals the inverse of the Fisher Information matrix of equation (4.12). Adding up the fact that the WLS estimator with the weights of equation (5.10) is unbiased, it can be concluded that the resulting estimator is in fact optimal in the Cramér-Rao sense. However, this selection requires knowledge of the parameters to be estimated, which contradicts the objective of the inference task. Therefore, in practice an alternative weight design must be considered.

The simplest weight selection approach is that of the plain Least-Squares (LS) estimator, where $w_i = 1, \forall i = 1, \ldots, n$. In this case, the weight selection does not take into account any bias about the problem (such as the shape and position of the PSF), nor assign more relevance to any of the observations I_i. Such an estimator behaves as shown in Figures 5.1 and 5.2. Two of the most prominent results are: the Least-Squares estimator is unbiased, no matter the resolution Δx or the brightness of the source; and for very weak sources the estimator can be considered optimal, which is consistent with the analysis presented in [Perryman et al., 1989] when assuming the background $\tilde{B}$ is known.

Further analysis on the shape of the curves observed, specially for brighter sources, and the convenience of less resolution (larger pixel sizes) shall benefit from more experimental evidence and shall therefore be discussed later.

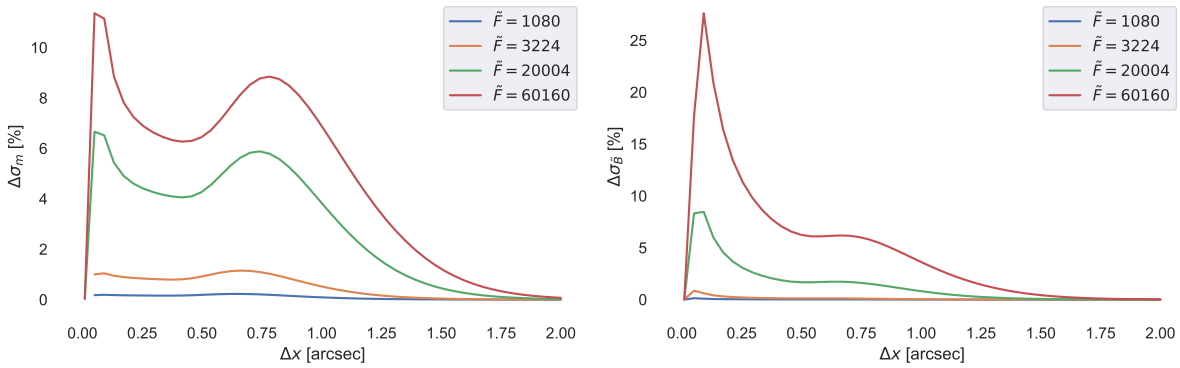

Figure 5.1: Performance discrepancies, as functions of pixel size Δx, for joint source flux and background estimation corresponding to the Least-Squares estimator for different source brightness.

In the following, an exploration of the weight-space is presented in order to study how close to the optimal parameters the weight set should be chosen to outperform the LS estimator. Reasonably, the considered weight-space comprises a structure of the form:

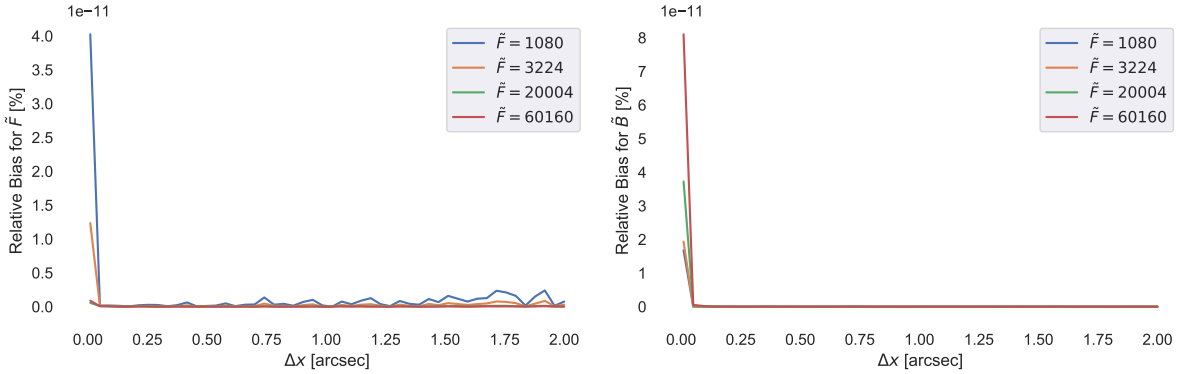

Figure 5.2: Relative biases, as functions of pixel size Δx, for joint source flux and background estimation corresponding to the Least-Squares estimator for different source brightness.

$$w_i = \frac{1}{\tilde{f} \cdot g_i(x_c) + \tilde{b}}, \quad \forall i \in \{1, \ldots, n\}, \tag{5.11}$$

where $\tilde{f}$ and $\tilde{b}$ can be interpreted as a prior belief regarding the source's flux and pixel background, respectively. For that matter, Figures 5.3 and 5.4 show the performance discrepancies for two point sources with $\tilde{F} = 1080$ and $\tilde{F} = 20004$ photo-e$^-$, respectively. For each of these study cases, the weights are defined as in equation (5.11), with $\tilde{f}$ taking values over a grid $\mathcal{G}_{\tilde{F}}$ and $\tilde{b} = \tilde{B}$. For each value of $\tilde{F}$, said grid is defined as:

$$\mathcal{G}_{\tilde{F}} = \{\tilde{f} = \tilde{F} + c \cdot \sqrt{\tilde{F}} : c \in \{-1, -0.8, -0.6, -0.4, -0.2, 0, 0.2, 0.4, 0.6, 0.8, 1\}\}. \tag{5.12}$$

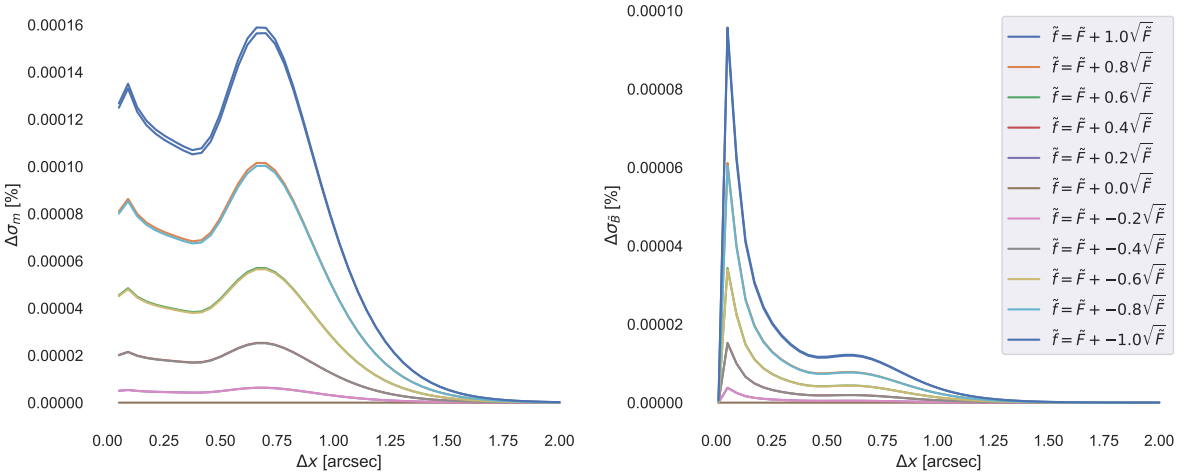

Figure 5.3: Performance discrepancies, as functions of pixel size Δx, for joint source flux and background estimation corresponding to the Weighted Least-Squares estimator with weights chosen over the grid $\mathcal{G}_{\tilde{F}}$, for $\tilde{F} = 1080$ photo-e$^-$.

It can be appreciated that the shape of the curves is preserved up to some extent, in comparison with the curves seen in Figure 5.1. As $\tilde{f}$ becomes farther from $\tilde{F}$, new and more prominent valleys

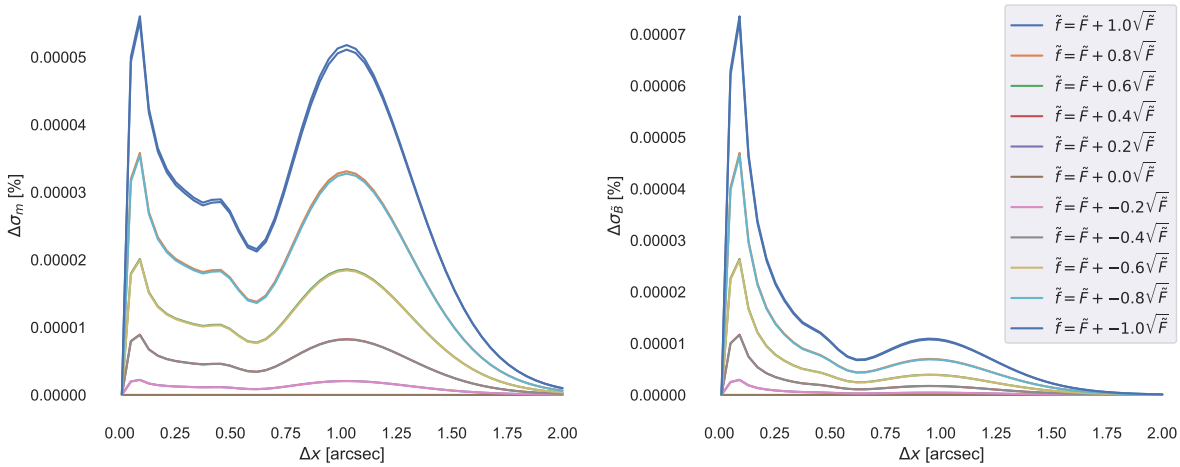

Figure 5.4: Performance discrepancies, as functions of pixel size Δx, for joint source flux and background estimation corresponding to the Weighted Least-Squares estimator with weights chosen over the grid $\mathcal{G}_{\tilde{F}}$, for $\tilde{F} = 20004$ photo-e$^-$.

and peaks appear. Moreover, the last one of those peaks becomes more tilted as $\tilde{f}$ draws away from $\tilde{F}$. This last behavior becomes even clearer when looking at Figures 5.5 and 5.6.

Despite that it is clear that the chosen grid is not a feasible option for a practical estimation problem, it reveals an interesting behavior of the discrepancies over weight design: both discrepancies exhibit some kind of symmetry around the optimal election $\tilde{f} = \tilde{F}$. Taking that into consideration, it is interesting to explore how far from the optimal value can $\tilde{f}$ without excessively hindering the overall performance of the WLS estimator. Figures 5.5 and 5.6 illustrate the effect of choosing $\tilde{f}$ far away from the value of $\tilde{F}$ on the estimator's performance.

The tilting effect mentioned before is shown even clearer, and so does the emergence of distortions on the curve's shape. More remarkable is the fact that the estimator is shown to be quite robust, in the sense that in order to raise $\Delta\sigma_m$ and $\Delta\sigma_{\tilde{B}}$ well beyond 5% requires $\tilde{f}$ to be chosen about 10 times larger than the optimal value.

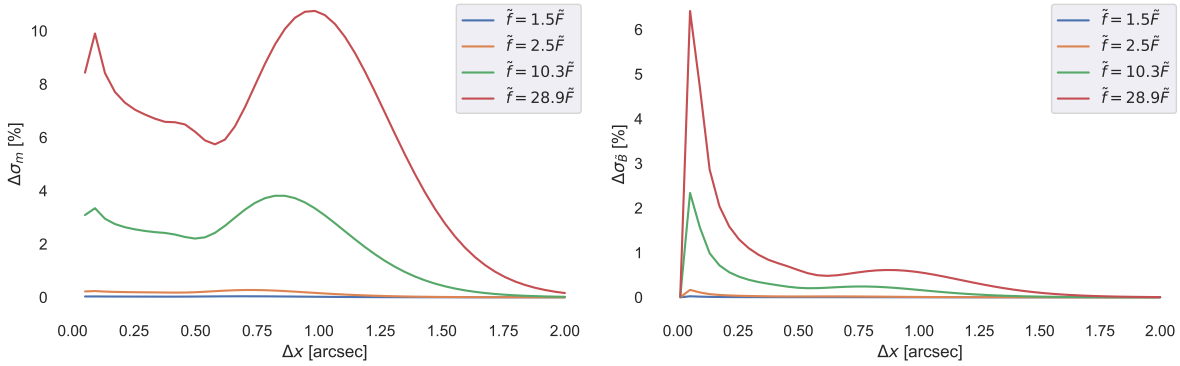

Figure 5.5: Performance discrepancies, as functions of pixel size Δx, for joint source flux and background estimation corresponding to the Weighted Least-Squares estimator with weights chosen such that $\tilde{f} = c \cdot \tilde{F}, c > 0.$, for $\tilde{F} = 1080$ photo-e$^-$.

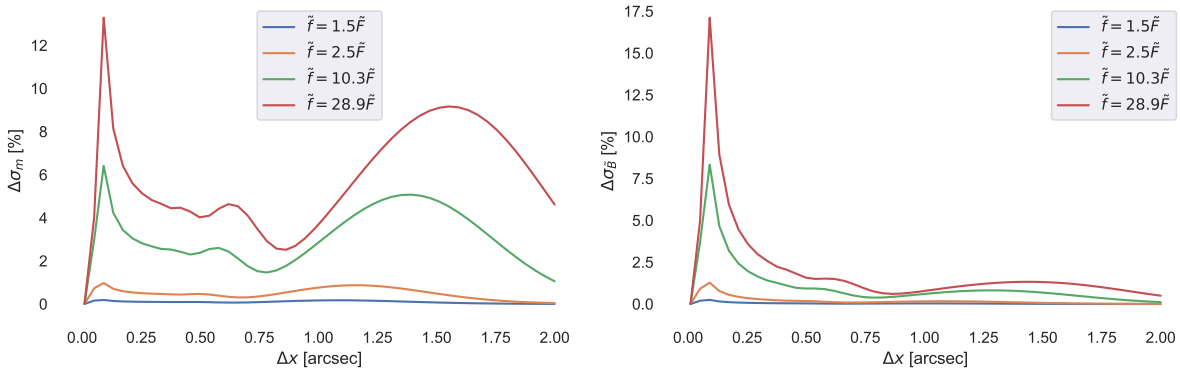

Figure 5.6: Performance discrepancies, as functions of pixel size Δx, for joint source flux and background estimation corresponding to the Weighted Least-Squares estimator with weights chosen such that $\tilde{f} = c \cdot \tilde{F}, c > 0.$, for $\tilde{F} = 20004$ photo-e$^-$.

The analysis on the effect of $\tilde{b}$ on the weight design proposed in equation (5.11) proceeds similarly. For that matter a grid $\mathcal{G}_{\tilde{B}}$ is defined as follows:

$$\mathcal{G}_{\tilde{B}} = \{\tilde{b} = \tilde{B} + c \cdot \sqrt{\tilde{B}} : c \in \{-1, -0.8, -0.6, -0.4, -0.2, 0, 0.2, 0.4, 0.6, 0.8, 1\}\}, \tag{5.13}$$

and, consequently, the weights are chosen as in equation (5.11), with $\tilde{f} = \tilde{F}$ and $\tilde{b} \in \mathcal{G}_{\tilde{B}}$.

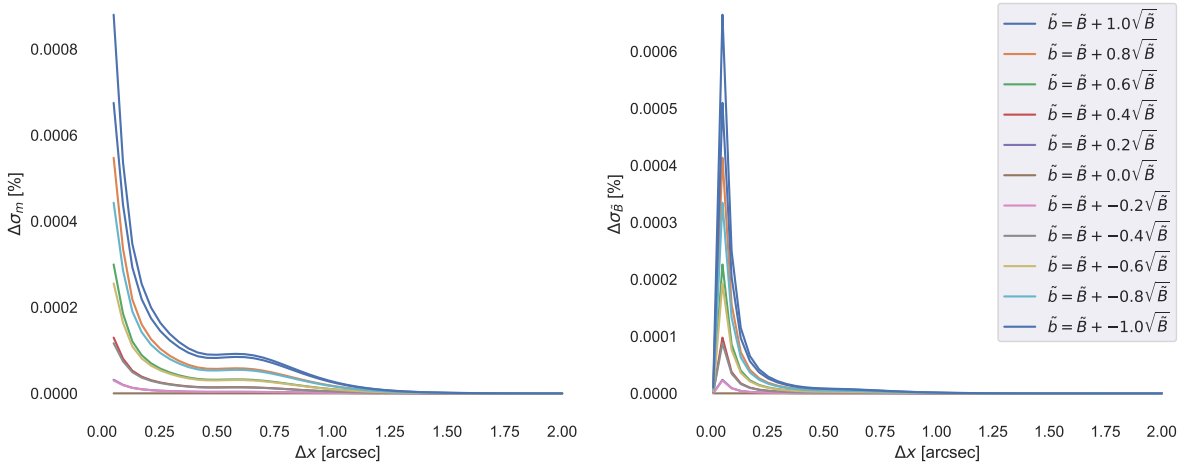

Figure 5.7: Performance discrepancies, as functions of pixel size Δx, for joint source flux and background estimation corresponding to the Weighted Least-Squares estimator with weights chosen over the grid $\mathcal{G}_{\tilde{B}}$, for $\tilde{F} = 1080$ photo-e$^-$.

From Figures 5.7, 5.8, 5.9 and 5.10 it follows a discussion that mostly resembles the one for previous analysis on $\tilde{f}$, and similar conclusions do apply, that is the emergence of symetry around the optimal $\tilde{b} = \tilde{B}$ and robustness in the same sense depicted above.

It is worth noting however that the estimator's performance seems to be more resilient to poorly chosen values of $\tilde{b}$, specially for weaker sources.

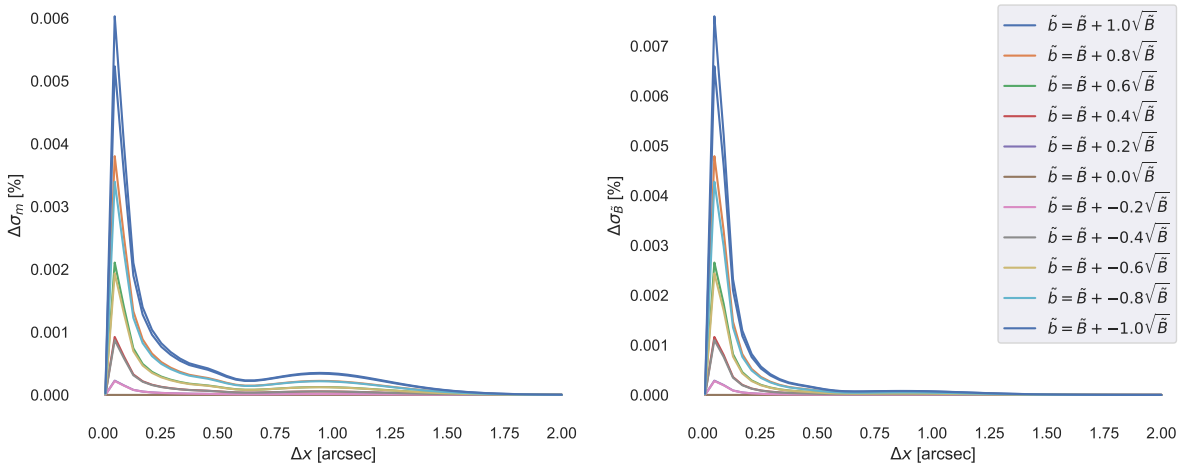

Figure 5.8: Performance discrepancies, as functions of pixel size Δx, for joint source flux and background estimation corresponding to the Weighted Least-Squares estimator with weights chosen over the grid $\mathcal{G}_{\tilde{B}}$, for $\tilde{F} = 20004$ photo-e$^-$.

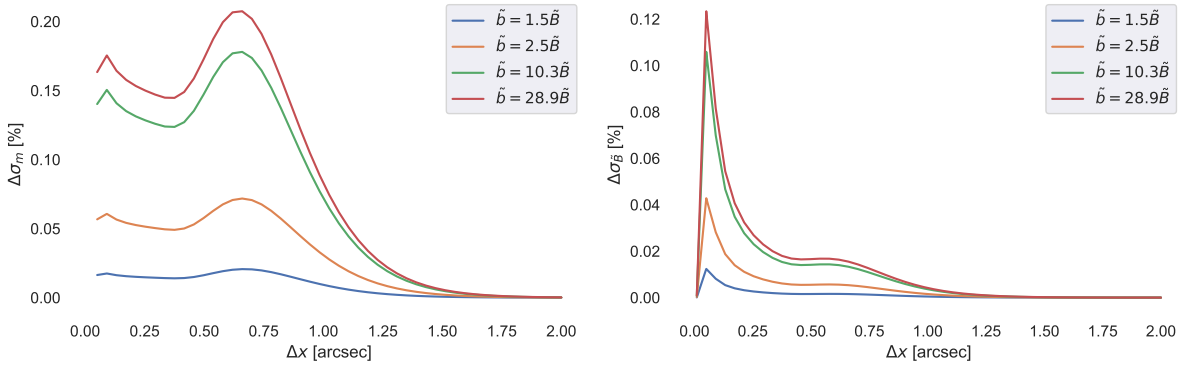

Figure 5.9: Performance discrepancies, as functions of pixel size Δx, for joint source flux and background estimation corresponding to the Weighted Least-Squares estimator with weights chosen such that $\tilde{b} = c \cdot \tilde{B}, c > 0.$, for $\tilde{F} = 1080$ photo-e$^-$.

Given these results, it is possible to come up with an alternative "worst-case scenario", other than the LS estimator, that takes into consideration the assumed information about the PSF of the object and the detector, without any prior belief on $\tilde{F}$ and $\tilde{B}$, that is a set of weights given by equation (5.11) with $\tilde{f} = 1$ and $\tilde{b} = D + RON^2$. Such an estimator will be referred here as "Uninformed" Weighted Least-Squares (UWLS) since it considers no initial guess on the parameters to be estimated, other than the bare minimum values possible without losing information on the PSF by means of $g_i(x_c)$. In other words, the estimator becomes clueless (*a priori*) about the brightness of the source and sky.

Figures 5.11 and 5.12 show how both the LS estimator and UWLS estimator compare to each other in terms of their respective discrepancies with the Cramér-Rao bounds, for different source brightness. Figure 5.11 corresponds to scenarios whose FWHM is 0.5 arcsec whilst Figure 5.12 comprises the similar scenarios whose FWHM is 1.5 arcsec.

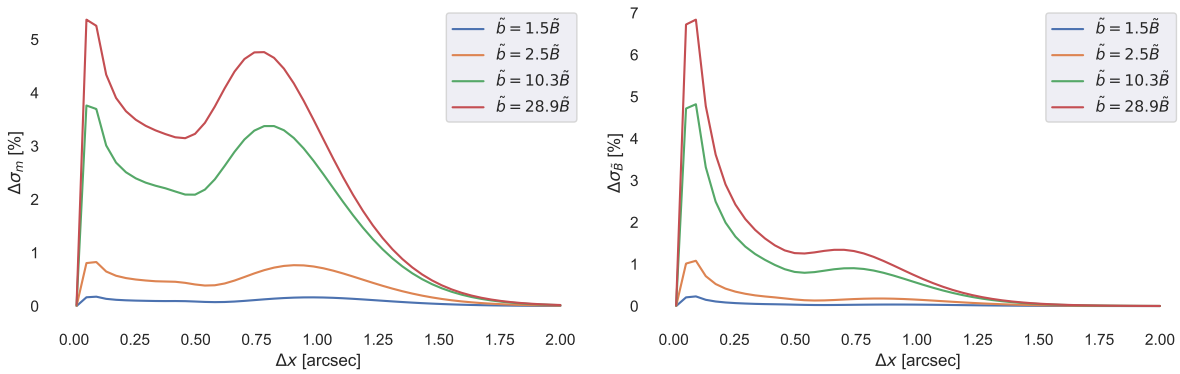

Figure 5.10: Performance discrepancies, as functions of pixel size Δx, for joint source flux and background estimation corresponding to the Weighted Least-Squares estimator with weights chosen such that $\tilde{b} = c \cdot \tilde{B}, c > 0.$, for $\tilde{F} = 20004$ photo-e$^-$.

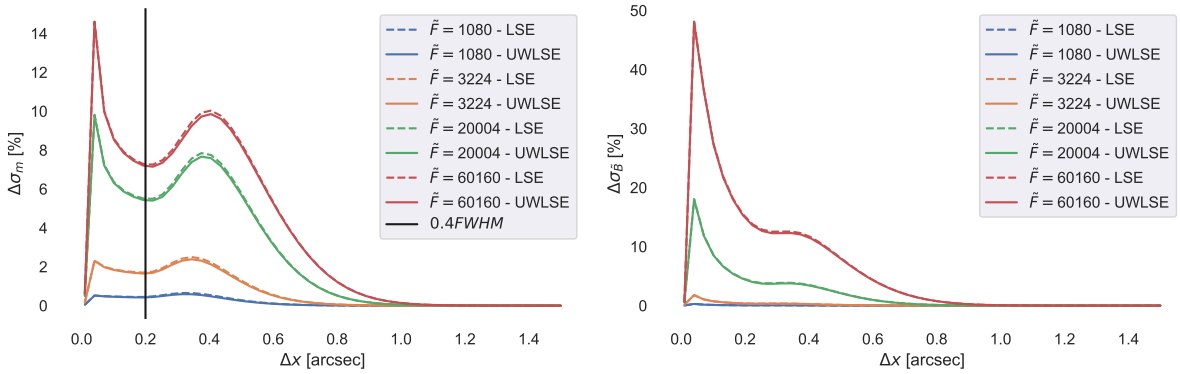

Figure 5.11: Performance comparison between LS estimator and UWLS estimator for different source brightness. $FWHM = 0.5$ arcsec.

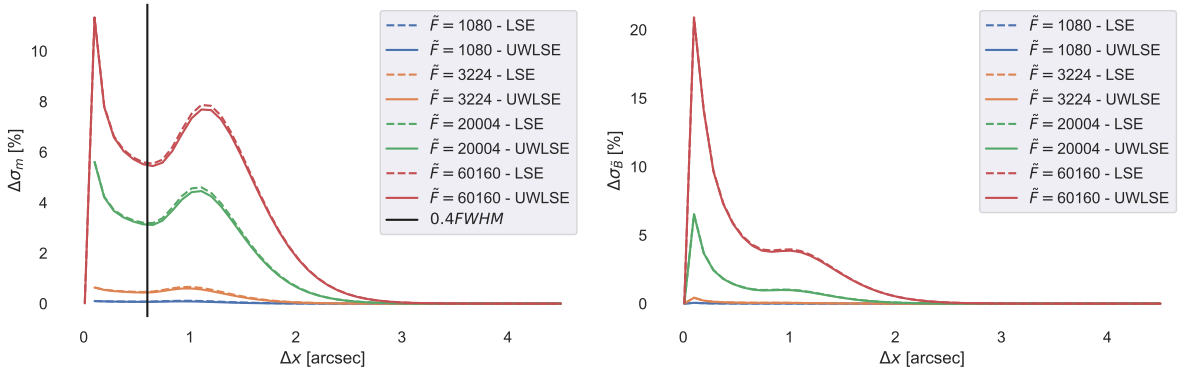

Figure 5.12: Performance comparison between LS estimator and UWLS estimator for different source brightness. $FWHM = 1.5$ arcsec.

For both Figures it has been considered Δx ranging from 0 up to $3 \times FWHM$. Provided this range, an interesting behavior emerges: the local minimum before the last peak of $\Delta\sigma_m$ (for any of the studied scenarios) lies around $\Delta x = 0.4 \times FWHM$. This finding supports (to some extent) typical pixel size values, as under that range of resolutions the expected discrepancy shall be

minimal, even for poorly chosen weight sets. Note that beyond the mentioned peak, which appears around $0.75 \times FWHM - 0.8 \times FWHM$, even though performance discrepancy diminishes such low resolutions aren't desirable because for such an instrument the Cramér-Rao bound deteriorates (see Section 4.2), thus lower discrepancy shall be equivalent to less precise estimations.

Up to this point, the worst-case scenarios for the WLS estimator have been characterized, verifying that for most practical cases the performance discrepancy on the flux, $\Delta\sigma_m$, shall lie between 0% and 10%[1]. On the other hand, achievability of the Cramér-Rao bounds requires knowledge of the desired parameters, making the weight selection of equation (5.10) unfeasible in practice. However, evidence shown so far suggest that by proper weight tweaking (and not necessarily optimal) huge improvements can be done, even to the point of near-optimality (see for example how the discrepancies shown in Figure 5.4 outperform by many orders of magnitude that from Figure 5.1 for the same observational scenario).

This motivates the introduction of a data-dependent version, $\hat{w}_i(\mathbf{I})$. WLS estimators defined through such a weight setting can be encompassed as Adaptive Weighted Least-Squares (AWLS).

Two different AWLS estimators can be introduced: on one hand, as I_i can be interpreted as a noisy version of $\lambda_i(x_c, \tilde{F})$, this justifies the following weight design:

$$\hat{w}_i(\mathbf{I}) = \hat{w}_i(I_i) = \frac{1}{I_i}, \quad \forall i = 1, \dots, n, \tag{5.14}$$

which can be interpreted as a noisy version of the optimal weight of equation (5.10). This data-driven weighting scheme shall here be referred to as Stochastic Weighted Least-Squares (SWLS)) as it relies on the random sample vector $\mathbf{I}$.

The second approach for an AWLS estimator, which is referred as Iterative Weighted Least-Squares (IWLS), is defined iteratively through an update rule: let $\{w_i^0\}_{i=1}^n$ be an initialization weight set arbitrarily chosen. Given a measurement vector $\mathbf{I}$ and a set of indices $\mathcal{J}$, $\{w_i^k\}_{i=1}^n, k > 0$ can be iteratively updated as:

$$\begin{aligned} w_i^k &= \frac{1}{\tau_{IWLS,1}^{k-1}(\mathbf{I}) \cdot g_i(x_c) + \tau_{IWLS,2}^{k-1}(\mathbf{I})}, \quad \forall i = 1, \dots, n, \\ \tau_{IWLS}^{k-1}(\mathbf{I}) &= \underset{\boldsymbol{\alpha} \in \boldsymbol{\Theta}}{\operatorname{argmin}} \sum_{i \in \mathcal{J}} w_i^{k-1} (I_i - \alpha_1 \cdot g_i(x_c) - \alpha_2)^2. \end{aligned} \tag{5.15}$$

Simply put, the IWLS estimator requires sequentially solving k WLS problems: $k-1$ problems in order to update the weight set and one last time to get the final estimation $(\hat{\tilde{F}}, \hat{\tilde{B}}) \equiv \tau_{IWLS}^k(\mathbf{I})$.

Figure 5.13 displays the performance discrepancies obtained through both adaptive estimation schemes, as functions of the pixel size for various sources. Figure 5.14 shows that both estimators hold the unbiasedness property, therefore comparison with previous results is admissible. As can

[1]Note that every weight setting studied until this moment has preserved the unbiasedness property of the WLS estimator.

be seen from Figure 5.13, both schemes overcome the struggles that previous estimators had when dealing with brighter sources, and for any practical effect they both achieve optimality, even though no prior belief or guess is required.

The weights employed in both adaptive estimation approaches are random variables. Therefore, the expectations by which the biases and discrepancies (more precisely the estimator's covariance matrix) are calculated need to consider that both $w_1, \ldots, w_n$ and $\mathbf{I}$ are random vectors. Since the probability distribution of $w_1, \ldots, w_n$ is not at hand, the mentioned expectations can be estimated trough empirical conditional expectations, taking samples of the random vector $\mathbf{I}$ to set the values for $w_1, \ldots, w_n$, which allows us to use the closed-form expectations given above.

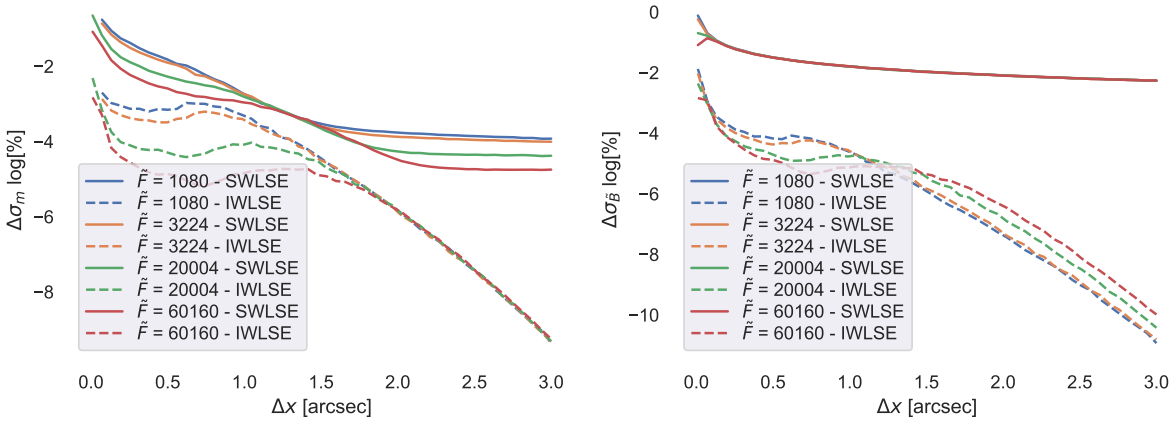

Figure 5.13: Performance discrepancies, as functions of pixel size Δx, for joint source flux and background estimation corresponding to adaptive versions of the WLS estimator for different source brightness.

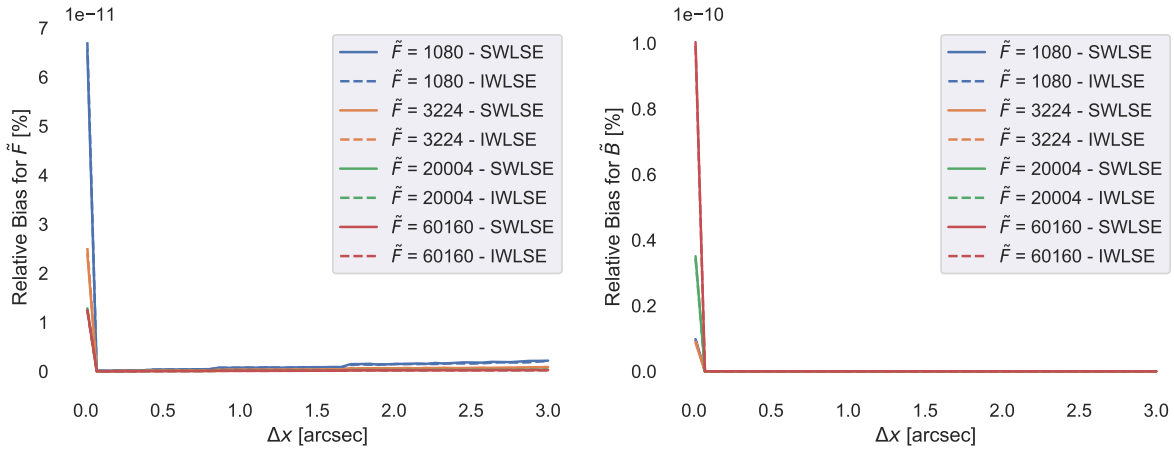

Figure 5.14: Relative biases, as functions of pixel size Δx, for joint source flux and background estimation corresponding to adaptive versions of the WLS estimator for different source brightness.

5.1.2 Aperture Analysis

Previous results assumed that all n pixels where employed during estimation. In this section, the effect of information usage is studied. For the sake of simplicity, the pixel selection scheme

considered along the following analysis is the aperture one described in Section 4.1, *i.e.*, $(\mathcal{J}_k) = \{\{n_{x_c}\}, \{n_{x_c}-1, n_{x_c}, n_{x_c}+1\}, \{n_{x_c}-2, n_{x_c}-1, n_{x_c}, n_{x_c}+1, n_{x_c}+2\}, \dots\}$. The objective here is to study if and how the AWLS estimators depicted above benefit from the addition of more information for estimation.

For that matter, let's introduce a second measure of discrepancy in order to assess optimality of the adaptive estimators, get a better understanding of it and develop comparisons. Let σ_m and $\sigma_{\tilde{B}}$ denote the Cramér-Rao bounds just as before, for any set $\mathcal{J}_k \neq \{1, \dots, n\}$, and let σ_m^{max} and $\sigma_{\tilde{B}}^{max}$ the corresponding Cramér-Rao Lower Bounds for $\mathcal{J}_k = \{1, \dots, n\}$, *i.e.*, the bounds obtained by taking into consideration all the n pixels. Consequently, for any set $\mathcal{J}_k \neq \{1, \dots, n\}$ in the selection scheme and the corresponding estimates' variances $Var(\tau_{J,1}(\mathbf{I})), Var(\tau_{J,2}(\mathbf{I}))$, the discrepancies with respect to σ_m and $\sigma_{\tilde{B}}$ are given just as in equations (5.6) and (5.7), and the ones calculated with respect to σ_m^{max} and $\sigma_{\tilde{B}}^{max}$ are given by:

$$\begin{aligned}\Delta\sigma_m^{max} &= \frac{\frac{2.5}{2}\cdot\left(\log\left(\tilde{F}+\sqrt{Var(\tau_{J,1}(\mathbf{I}))}\right)-\log\left(\tilde{F}-\sqrt{Var(\tau_{J,1}(\mathbf{I}))}\right)\right)-\sigma_m^{max}}{\sigma_m^{max}}\times 100 \\ &= \frac{\frac{2.5}{2}\cdot\left(\log\left(\tilde{F}+\sqrt{[\mathbf{C}_{\tau_J}]_{1,1}}\right)-\log\left(\tilde{F}-\sqrt{[\mathbf{C}_{\tau_J}]_{1,1}}\right)\right)-\sigma_m^{max}}{\sigma_m^{max}}\times 100,\end{aligned} \tag{5.16}$$

$$\begin{aligned}\Delta\sigma_{\tilde{B}}^{max} &= \frac{\sqrt{Var(\tau_{J,2}(\mathbf{I}))}-\sigma_{\tilde{B}}^{max}}{\sigma_{\tilde{B}}^{max}}\times 100 \\ &= \frac{\sqrt{[\mathbf{C}_{\tau_J}]_{2,2}}-\sigma_{\tilde{B}}^{max}}{\sigma_{\tilde{B}}^{max}}\times 100.\end{aligned} \tag{5.17}$$

In other words, $\Delta\sigma_m^{max}$ and $\Delta\sigma_{\tilde{B}}^{max}$ denote discrepancy between any estimator $\tau_J(\cdot)$ got over any set $\mathcal{J}_k \subseteq \{1, \dots, n\}$ and the maximal achievable precision attainable with an instrument equipped with the n pixels. With such a distinction it is possible to discern how much of all the information available in $\mathbf{I}$ is obtained along the pixel selection scheme $(\mathcal{J}_k)$.

Before going deeper on the performance analysis for the SWLS and IWLS estimators, it is worth noting that the aperture scheme does not break the unbiasedness property of the estimators, as seen on Figure 5.15, validating comparisons with the CRLBs.

Looking at Figure 5.16, it may seem that there's some sort of sufficient aperture. After approximately half the pixels on the CCD are incorporated into the inference process the discrepancies stabilize. This statement applies for both estimators, even though the iterative scheme shows to be more precise than the SWLS estimator. Nevertheless, the value of σ_m and $\sigma_{\tilde{B}}$ is not static as the aperture increases. In fact, these quantities approaches σ_m^{max} and $\sigma_{\tilde{B}}^{max}$, respectively, as more pixels are added in the analysis, just as seen in Section 4.1. If the discrepancies with respect to σ_m^{max} and $\sigma_{\tilde{B}}^{max}$ are observed instead, the scene drastically changes, as seen on Figure 5.17.

It becomes evident that as the aperture increases both discrepancies shown in Figure 5.17 decrease monotonically. However, the rate at which $\Delta\sigma_m^{max}$ decreases also diminishes with aperture,

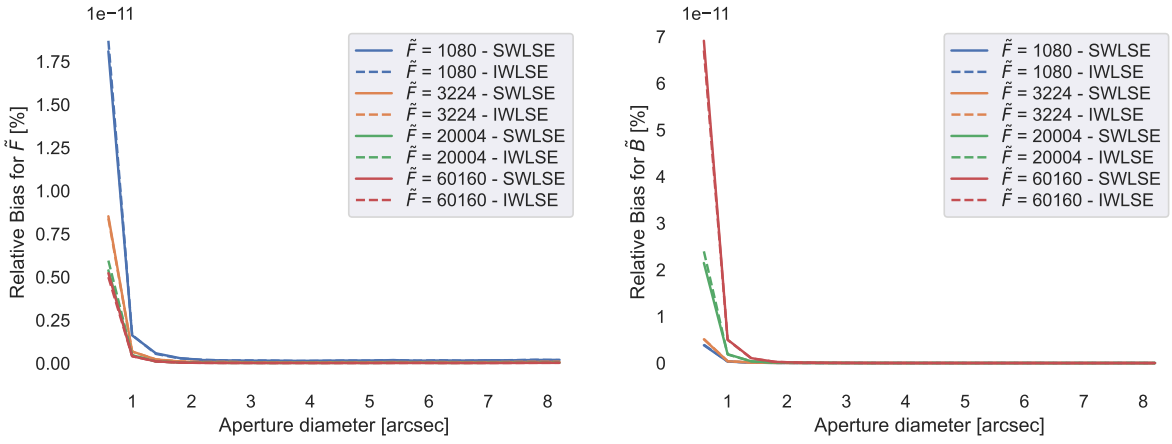

Figure 5.15: Relative biases for different apertures corresponding to the adaptive WLS estimators for different source brightness.

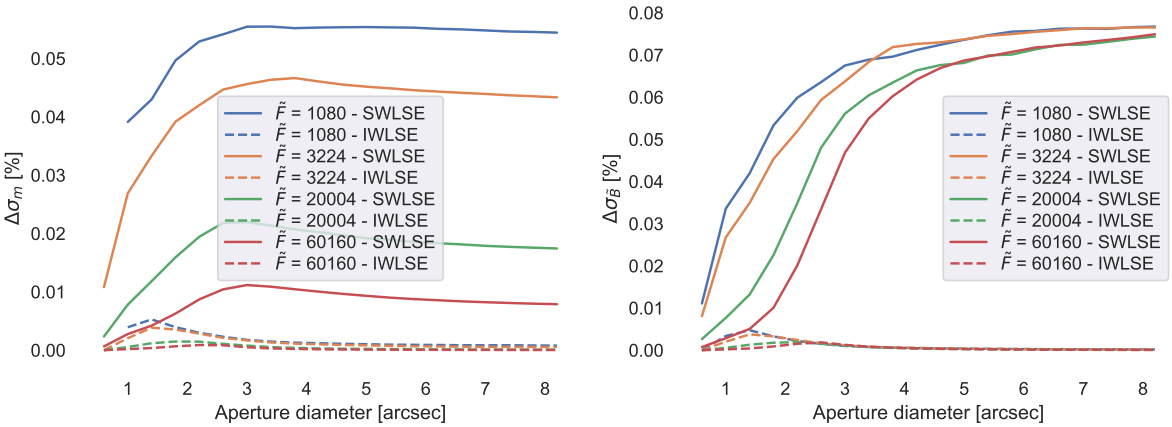

Figure 5.16: Performance discrepancies for different apertures corresponding to the adaptive WLS estimators for different source brightness.

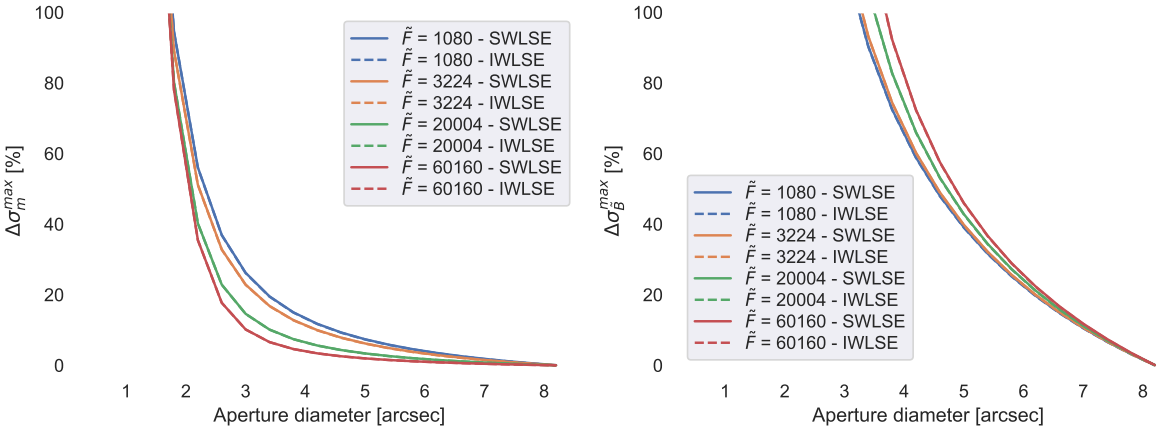

Figure 5.17: Performance discrepancies with respect to $\sigma_{\tilde{m}}^{max}$ (left) and $\sigma_{\tilde{B}}^{max}$ (right) for different apertures corresponding to the adaptive WLS estimators for different source brightness.

specially for brighter sources. Therefore, as the main objective of this joint estimation problem is to characterize the source (*i.e.*, its flux $\tilde{F}$) and the estimation of $\tilde{B}$ takes a secondary role, it may seem reasonable to state that for an aperture diameter of around three to five times[2] the source's FWHM the estimator's precision shall be good enough in most cases. This could be the case if $\hat{\tilde{F}}$ and $\hat{\tilde{B}}$, as random variables, were independent or very weakly correlated. However, this is not the case, as illustrated by Figure 5.18.

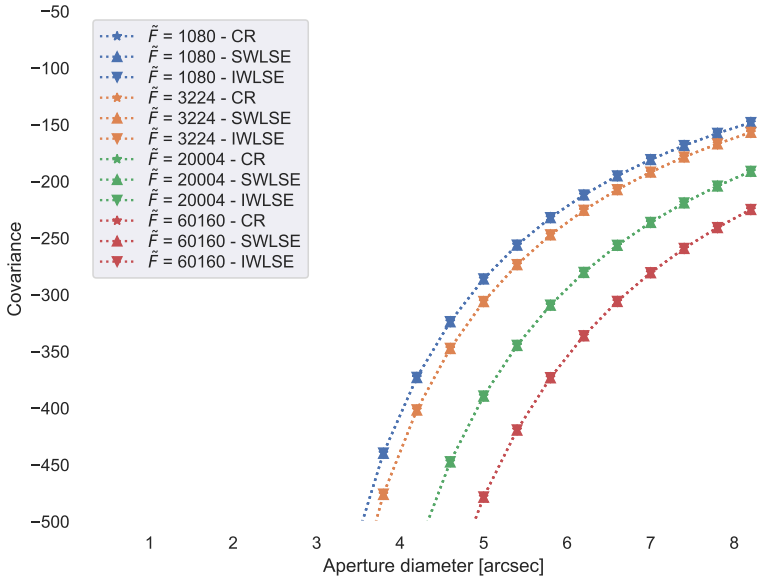

Figure 5.18: Covariances of the SWLS and IWLS estimators and their comparison with their Cramér-Rao counterpart, under different apertures and source brightness.

The decreasing magnitude of the correlation between both estimates $\hat{\tilde{F}}$ and $\hat{\tilde{B}}$ can be statistically interpreted as a reduction in the error of one estimate, as an outcome of the other one's error. In other words, it is expected that as one estimate deviates from its mean value (hopefully the true value), the other one shall do that as well.

Consequently, Figures 5.17 and 5.18 may indicate that as the estimates become less correlated to each other, the errors are less likely to propagate from one to another, and such errors also diminish as aperture increases. This may serve as further justification to adopt larger apertures for joint inference, this time from a practical standpoint.

Furthermore, stepping back to Figure 5.16, we note that for the case of the SWLS flux estimate two phases can be recognized, one where discrepancy slightly increases with aperture, followed by a much smoother steady decrease. This change of phase precisely at around three times the FWHM coincides with a decrease on the rate at which $\Delta\sigma_m^{max}$ approaches 0, suggesting once more the existence of a sufficient, if not minimal, aperture that ensures precision above a desired prescription. This principle seems to be independent of the flux's magnitude, as the ratio between the aperture and the FWHM seems to play a much prominent role, which can be recognized when looking at Figures 5.17, 5.19 and 5.20.

[2]See for example Figures 5.19 and 5.20, which show similar results for sources whose FWHM is 0.5 and 1.5 arcsec, respectively.

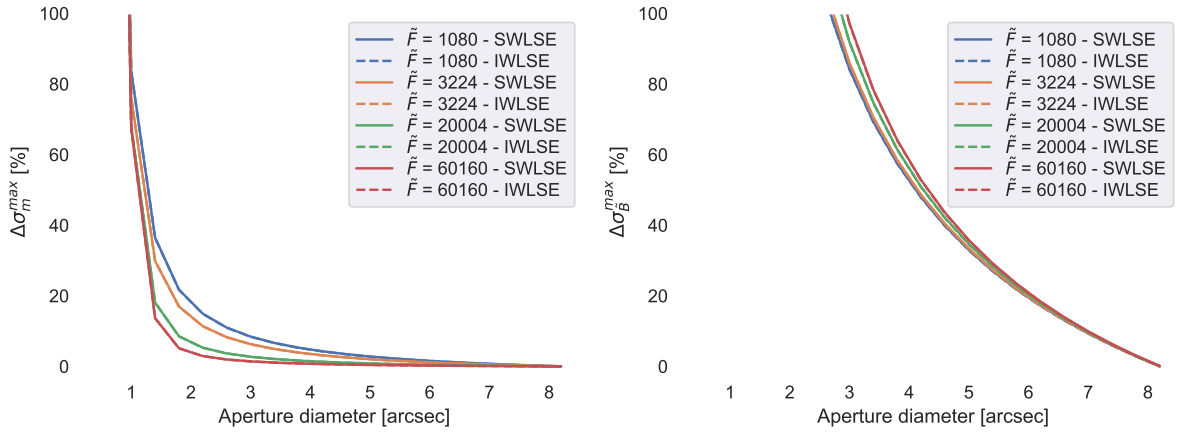

Figure 5.19: Performance discrepancies with respect to σ_m^{max} (left) and $\sigma_{\tilde{B}}^{max}$ (right) for different apertures corresponding to the adaptive WLS estimators for different sources with $FWHM = 0.5$ [arcsec].

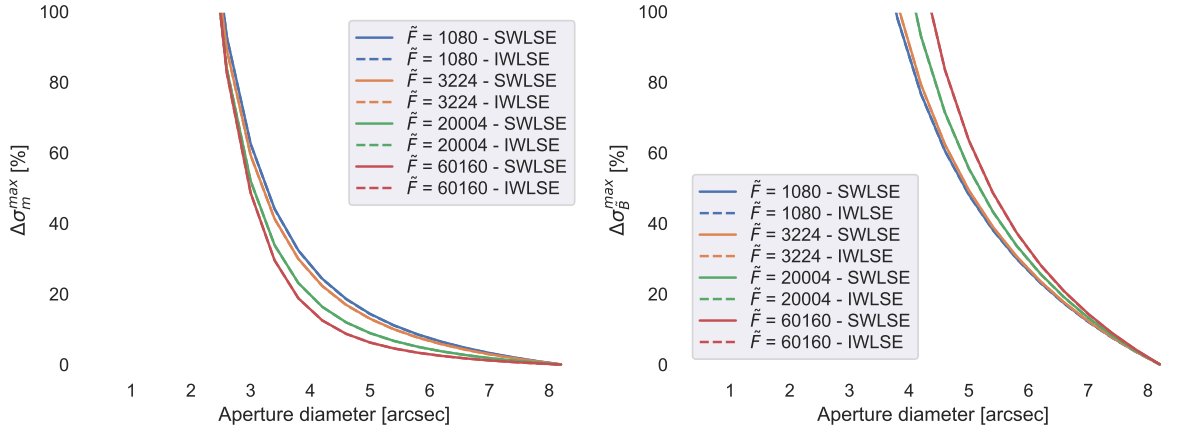

Figure 5.20: Performance discrepancies with respect to σ_m^{max} (left) and $\sigma_{\tilde{B}}^{max}$ (right) for different apertures corresponding to the adaptive WLS estimators for different sources with $FWHM = 1.5$ [arcsec].

5.1.3 Further Remarks

Under the light of the analysis performed so far in this section, we stress on the relevance of the hypothesis of other parameters' knowledge (the shape, position and width of the source's PSF). This feature is of key importance, not only because it is part of the estimator's design (see equation (5.1)) and weight tweaking (see equations (5.11) or (5.15) for example), in any of its studied flavors, but also because it can hinder or mislead the estimator's output, resulting in less precise or even biased results.

As an example of reduced precision lays the case of plain LS estimator, which is the case of not tweaking the weights with any information on shape, mode or width and have demonstrated to show discrepancies to the Cramér-Rao bounds slightly greater than the UWLS estimator and up to two orders of magnitude greater that some more data-driven approaches.

However, erroneous information about the PSF can propagate through weight adjustment and induce bias. From the optimization functional of equation (5.1), we note that information on the luminous profile of the object may or may not be included in w_i, but forms a substantial part of the squared error terms by $g_i(x_c)$, by outlining the shape perceived through $\mathbf{I}$. If improperly set, $g_i(x_c)$ increases the overall error measured when evaluating any set of solutions near the actual parameter vector $\alpha^\star$, leading in fact to biased solutions once the algorithm is performed, despite weight adjustment. To illustrate this effect see Figure 5.21, which shows the relative bias exhibited by the SWLS and IWLS estimators for different sources with narrow PSFs ($FWHM = 0.5$ [arcsec]).

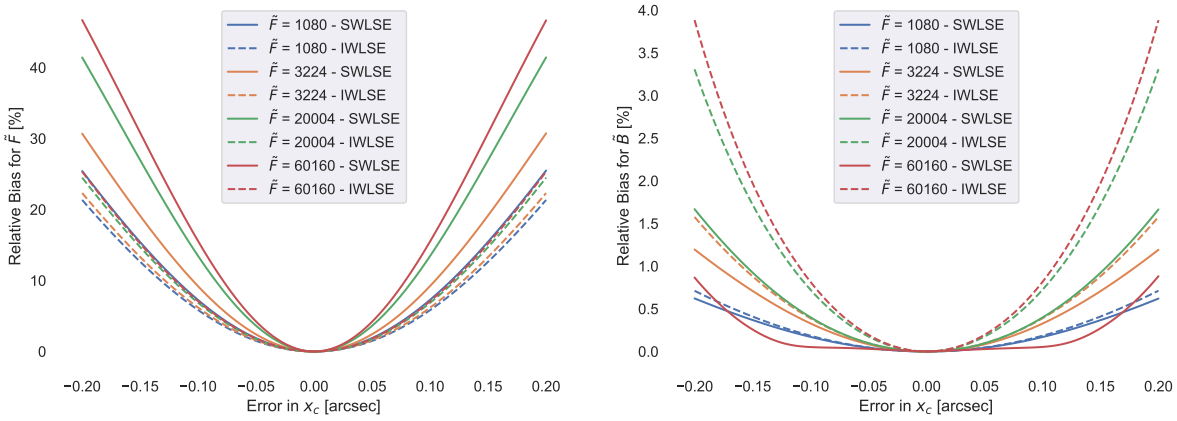

Figure 5.21: Relative biases obtained by adaptive WLS estimators for different sources with $FWHM = 0.5$ [arcsec].

We note that the x-axis varies between -0.2 and 0.2 arcseconds, which corresponds solely to ± 1 pixel. Such an error in the x_c parameter, though relatively large due to the narrow PSF, can lead to a flux bias of at least 20% for fainter sources, cases on which the estimators tend to be more robust. Naturally, as the error in x_c increases, so does the bias, both for flux- and backgroud-estimates.

It can be expected already that this bias effect is less significant the lesser the relative magnitude between the error in x_c and the width of the object's PSF is, as adjacent PRF values $g_i(x_c)$ are more similar for widely spread (Gaussian) light profiles. The results for such scenarios are shown in Figures 5.22 and 5.23. For a given source, the same position error of ± 1 pixel translates into less and less relative bias as the light received from the source spreads wider. This is because the overlap between the light profiles outlined by the measurements $\mathbf{I}$ (or the actual PSF for that matter) and the miss-identified values of $g_i(x_c)$ increases with width, as long as we are provided with accurate values of the FWHM. This overlap helps the estimation process by "masking" the shift on these profiles induced by the error in position.

One last remark on behalf of the role of the PSF's width and the biases induced by a miss-identification of the source's position is the fact that the biases showed by our two forms of adaptive estimators flip as the FWHM of a given source increases. That is, while the IWLS estimator tends to outperform (bias-wise) the SWLS estimator when the light of a given source spreads narrower (see Figure 5.21), the opposite happens when the same brightness is spread along a wider area (see Figure 5.23).

However, what's more relevant to this work is the effect of miss-information on the estimator's variance and its behavior relative to the performance metrics established by the Cramér-Rao

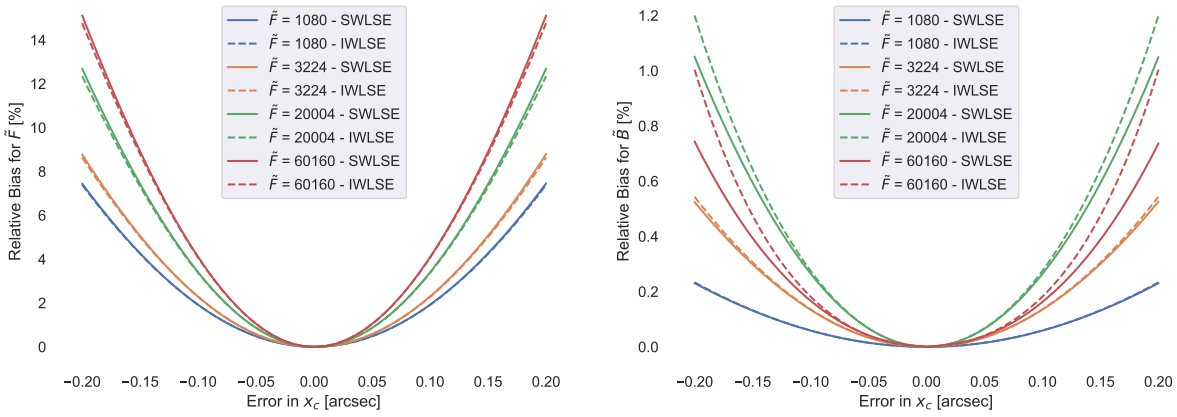

Figure 5.22: Relative biases obtained by adaptive WLS estimators for different sources with $FWHM = 1.0$ [arcsec].

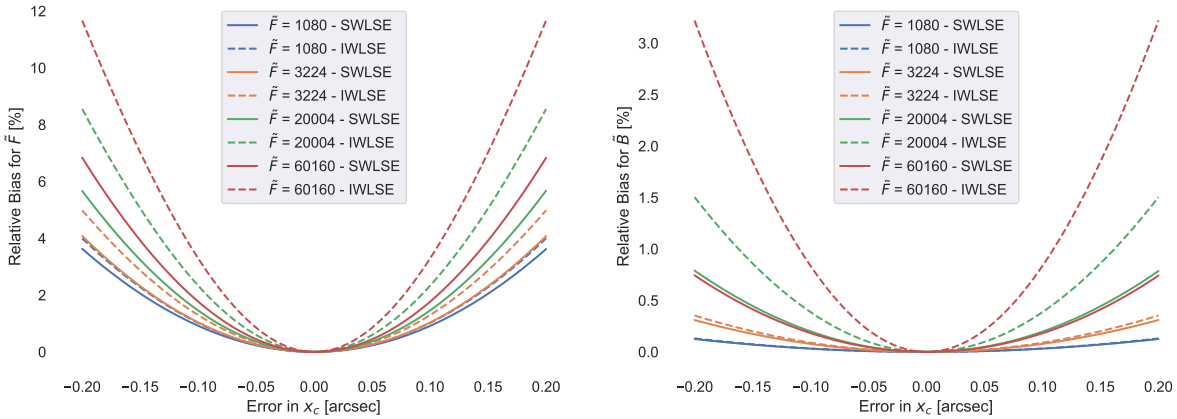

Figure 5.23: Relative biases obtained by adaptive WLS estimators for different sources with $FWHM = 1.5$ [arcsec].

bounds. As bias is induced due to a mismatch between the position provided to the inference algorithm and the actual position of the object, performance comparison with the bounds stated in Theorem 2.1 can not hold anymore.

We illustrate this in Figure 5.24, where it is shown that the performance of $\hat{\tilde{F}}$ is usually better (variance-wise) than that given by the respective CRLB in a wide range of position error. If we refer back to Figure 5.21, we note a clear relation between bias and variance, a trade-off due to the error in the location: the more bias is to be expected, the lower variance the estimate provides.

The case for background estimates is different, nevertheless: the figure shows curves of shapes other than the concave parabolae seen for flux, and though the Cramér-Rao bound still holds, Theorem 2.1 itself doesn't. What's to be kept in mind is the fact that both estimates become biased as a consequence of erroneous information.

This apparent gain in performance is a clear example of the bias-variance trade-off. The study of biased estimation goes beyond the scope of this work and will be not further discussed here. However, there's plenty of literature on this field (see for example Eldar's works such as

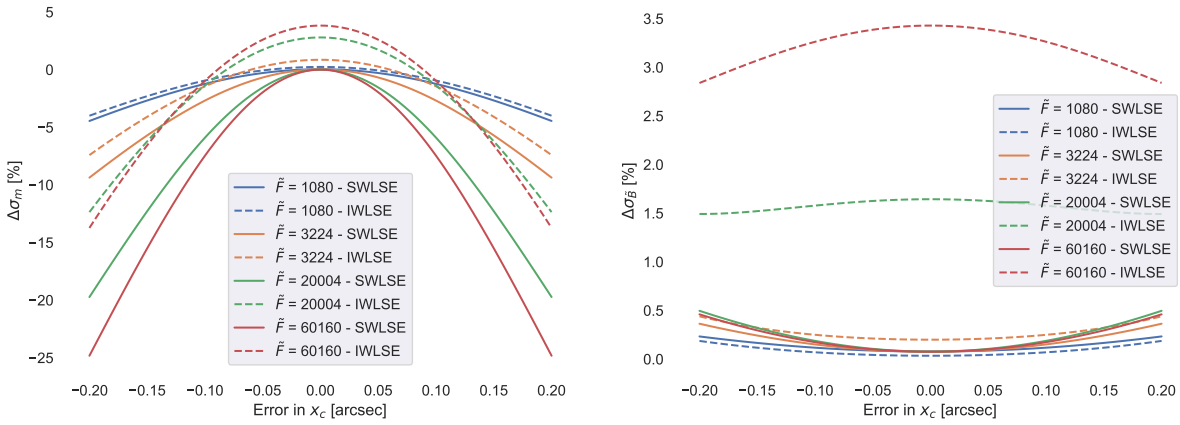

Figure 5.24: Performance discrepancies obtained by adaptive WLS estimators for different sources with $FWHM = 0.5$ [arcsec].

[Kay and Eldar, 2008, Eldar, 2008] and references therein) which could serve as a baseline for future works on the problem of joint estimation of flux and background under this standpoint.

5.2 Bounding the Performance of the SWLS Estimator

The introduction of the Stochastic Weighted Least-Squares (SWLS) estimator serves a second purpose, which is to be studied in this subsection. By replacing its respective set of weigths $\{\hat{w}_i(I_i)\}_{i\in\mathcal{J}}$ into equations (5.1) and (5.3) it is possible to define the correspondent optimization problem and to find its closed-form solution as a non-linear (over the observation space) vector function, *i.e.*,

$$J_{SWLS}(\boldsymbol{\alpha}, \mathbf{I}) = \sum_{i\in\mathcal{J}} \frac{1}{I_i}(I_i - \alpha_1 \cdot g_i(x_c) - \alpha_2)^2, \tag{5.18}$$

$$\begin{aligned}\tau_{SWLS}(\mathbf{I}) &= \underset{\boldsymbol{\alpha}\in\boldsymbol{\Theta}}{\operatorname{argmin}} J_{SWLS}(\boldsymbol{\alpha}, \mathbf{I}) \\ &= \begin{bmatrix} \sum_{i\in\mathcal{J}} \frac{1}{I_i} \cdot g_i^2(x_c) & \sum_{i\in\mathcal{J}} \frac{1}{I_i} \cdot g_i(x_c) \\ \sum_{i\in\mathcal{J}} \frac{1}{I_i} \cdot g_i(x_c) & \sum_{i\in\mathcal{J}} \frac{1}{I_i} \end{bmatrix}^{-1} \cdot \begin{bmatrix} \frac{1}{I_{i_1}} \cdot g_{i_1}(x_c) & \cdots & \frac{1}{I_{i_{|\mathcal{J}|}}} \cdot g_{i_{|\mathcal{J}|}}(x_c) \\ \frac{1}{I_{i_1}} & \cdots & \frac{1}{I_{i_{|\mathcal{J}|}}} \end{bmatrix} \cdot \mathbf{I}.\end{aligned} \tag{5.19}$$

The non-linearity property of $\tau_{SWLS}(\cdot)$ observed in equation (5.19) allows us to approximate the estimates from their Taylor expansion and, consequently, study the bounds given by the formulation presented in Section 3. Indeed, we can guarantee that the actual solution of the optimization problem is available for calculating its performance bounds, and the approximation of the vector $\tau_{SWLS}(\cdot)$ relies on a non-trivial Taylor polynomial, unlike the more standard WLS estimator already analysed. Therefore, the following analysis serves as an experimental validation of the theoretical results deduced earlier in this work.

5.2.1 SWLS as a non-linear Estimator

From the formulation depicted in equations (5.18) and (5.19) the performance bounds of the SWLS estimator can be obtained through a straightforward application of the equations presented in Section 3. For that matter, it suffices to calculate the expressions corresponding to the application of the different ∇^{ij} operators on the cost function $J_{SWLS}(\cdot)$ (the detailed derivation of such expressions can be found in Appendix D). For the case of the two-dimensional arrays $\nabla^{11}J_{SWLS}(\boldsymbol{\alpha},\mathbf{I})$ and $\nabla^{20}J_{SWLS}(\boldsymbol{\alpha},\mathbf{I})$ we have that:

$$\nabla^{11}J_{SWLS}(\boldsymbol{\alpha},\mathbf{I}) = \begin{bmatrix} -\frac{2g_{i_1}(x_c)}{I_{i_1}^2}(\alpha_1 g_{i_1}(x_c)+\alpha_2) & \cdots & -\frac{2g_{i_{|\mathcal{J}|}}(x_c)}{I_{i_{|\mathcal{J}|}}^2}(\alpha_1 g_{i_{|\mathcal{J}|}}(x_c)+\alpha_2) \\ -\frac{2}{I_{i_1}^2}(\alpha_1 g_{i_1}(x_c)+\alpha_2) & \cdots & -\frac{2}{I_{i_{|\mathcal{J}|}}^2}(\alpha_1 g_{i_{|\mathcal{J}|}}(x_c)+\alpha_2) \end{bmatrix}, \tag{5.20}$$

$$\nabla^{20}J_{SWLS}(\boldsymbol{\alpha},\mathbf{I}) = 2\begin{bmatrix} \sum_{i\in\mathcal{J}}\frac{g_i^2(x_c)}{I_i} & \sum_{i\in\mathcal{J}}\frac{g_i(x_c)}{I_i} \\ \sum_{i\in\mathcal{J}}\frac{g_i(x_c)}{I_i} & \sum_{i\in\mathcal{J}}\frac{1}{I_i} \end{bmatrix}. \tag{5.21}$$

Now let's focus our attention on the three-dimensional arrays resulting from applying ∇^{12}, ∇^{21} and ∇^{30}. For the former array, it follows that it can be described as two stacked diagonal matrices, which are

$$\left[\nabla^{12}J_{SWLS}(\boldsymbol{\alpha},\mathbf{I})\right]_{(1,\cdot,\cdot)} = \begin{bmatrix} \frac{4g_{i_1}(x_c)}{I_{i_1}^3}(\alpha_1 g_{i_1}(x_c)+\alpha_2) & & \\ & \ddots & \\ & & \frac{4g_{i_{|\mathcal{J}|}}(x_c)}{I_{i_{|\mathcal{J}|}}^3}(\alpha_1 g_{i_{|\mathcal{J}|}}(x_c)+\alpha_2) \end{bmatrix}, \tag{5.22}$$

and

$$\left[\nabla^{12}J_{SWLS}(\boldsymbol{\alpha},\mathbf{I})\right]_{(2,\cdot,\cdot)} = \begin{bmatrix} \frac{4}{I_{i_1}^3}(\alpha_1 g_{i_1}(x_c)+\alpha_2) & & \\ & \ddots & \\ & & \frac{4}{I_{i_{|\mathcal{J}|}}^3}(\alpha_1 g_{i_{|\mathcal{J}|}}(x_c)+\alpha_2) \end{bmatrix}. \tag{5.23}$$

Then, $\nabla^{21}J_{SWLS}(\boldsymbol{\alpha},I)$ can be written by means of the indices $i\in\mathcal{J}$ as

$$\left[\nabla^{21}J_{SWLS}(\boldsymbol{\alpha},\mathbf{I})\right]_{(\cdot,\cdot,i)} = \begin{bmatrix} -\frac{2g_i^2(x_c)}{I_i^2} & -\frac{2g_i(x_c)}{I_i^2} \\ -\frac{2g_i^2(x_c)}{I_i^2} & -\frac{2}{I_i^2} \end{bmatrix}. \tag{5.24}$$

Lastly, $\nabla^{30}J_{SWLS}(\boldsymbol{\alpha},\mathbf{I})$ corresponds to a $2\times 2\times 2$ zero-valued array, *i.e.*,

$$\nabla^{30} J_{SWLS}(\boldsymbol{\alpha}, \mathbf{I}) = \mathbf{0}. \tag{5.25}$$

With these expressions at hand, the computation of the bias and variance bounds can be straightforwardly performed by plugging them in into the equations presented in Section 3.

5.2.2 Numerical Analysis

As already stated, the aim of this subsection is to experimentally validate to some extent the bounds obtained through the Taylor expansion of a multidimensional estimator defined by some optimization objective shown in Section 3. To do so, we recall on the scenarios studied in Section 4.1, and an additional case corresponding to an extremely faint source in which the total flux corresponds to $F = 500$ ADU while maintaining the rest of the parameters equal to those of the base case.

We start our analysis by reviewing the bias bounds obtained through our methodology, which are shown in Figure 5.25.

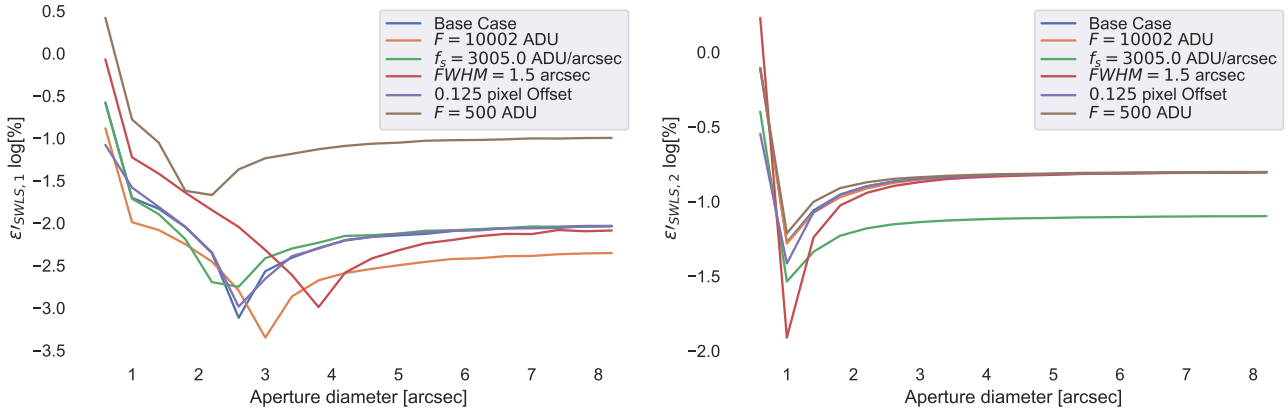

Figure 5.25: Bias bounds for joint source flux (left) and background (right) estimation under different observational scenarios, for an aperture selection scheme.

Though it may appear that some bias is to be expected when performing estimation with this method (as even for large aperture diameters values around 0.2% are achieved), our previous analysis (see Section 5.1) shows evidence that the estimator is unbiased for both parameters. For that matter, the values for $\varepsilon'_{SWLS,1}$ and $\varepsilon'_{SWLS,2}$ displayed in the figure do indeed bound the bias in any of the studied cases, even for the small radii scenario for which the bounds become looser, yet still valid.

Last but not least is the analysis of the variance bounds obtained through our methodology, as they are to some extent the cornerstone of this work. Let us focus briefly on the base case, whose results are displayed in Figure 5.26. The figure shows the corresponding Cramér-Rao bound for both parameters as reference, since it allows to assess the optimality of the estimator; the lower, central and upper values of the interval that defines the variance bounds (see equation (3.8)), and an empirical estimate of the variance obtained from simulated samples. All these values are shown as the squared root of the variance.

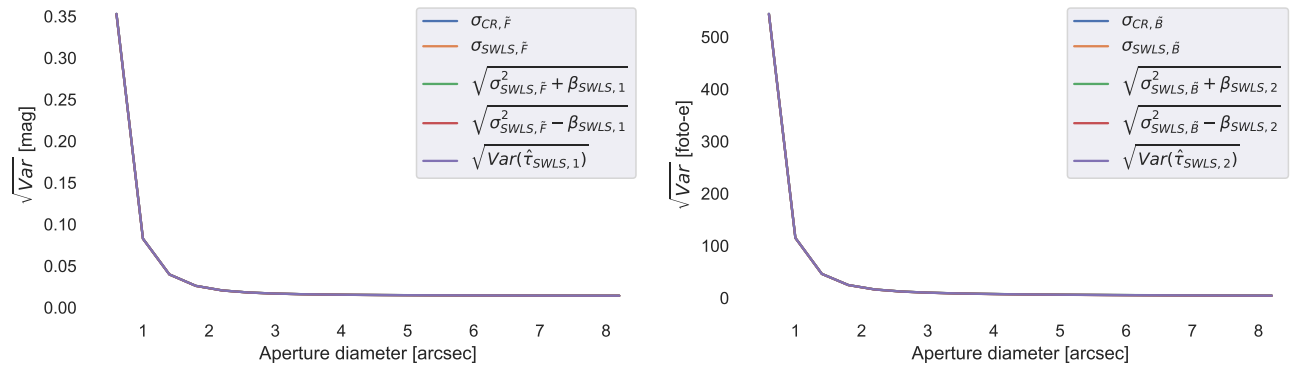

Figure 5.26: Variance bounds for joint source flux (left) and background (right) estimation for the considered base case, under an aperture selection scheme.

As can be seen in the figures, in the scale and units employed for the y axis (mag for $\tilde{F}$ and photo-e$^-$ for $\tilde{B}$) the bounds are tightly close to the CRLB, and so are the central values $\sigma^2_{SWLS,\cdot}$ and the variance's empirical proxy, to the point where the curves become indistinguishable from each other. This overall behavior is a constant in each one of the scenarios studied and is the reason to show the curves correspondent to the base case only. What is to be kept from these results, beyond the relative tightness, is the fact that the curves are monotonous on the aperture, thus recovering the main argument of this work of improving performance by jointly estimating the parameters with increasing aperture, even from our approximation and bounds.

However, the objective of this subsections was to validate experimentally the equations developed in Section 3, for which the scaling of Figure 5.26 is not helpful at all. For that matter, Figure 5.27 shows the same results but in the form of performance discrepancies ($\Delta\sigma_\cdot$) to visualize the bounds and the variance estimate more properly, and incorporates some of the scenarios left behind in the previous analysis.

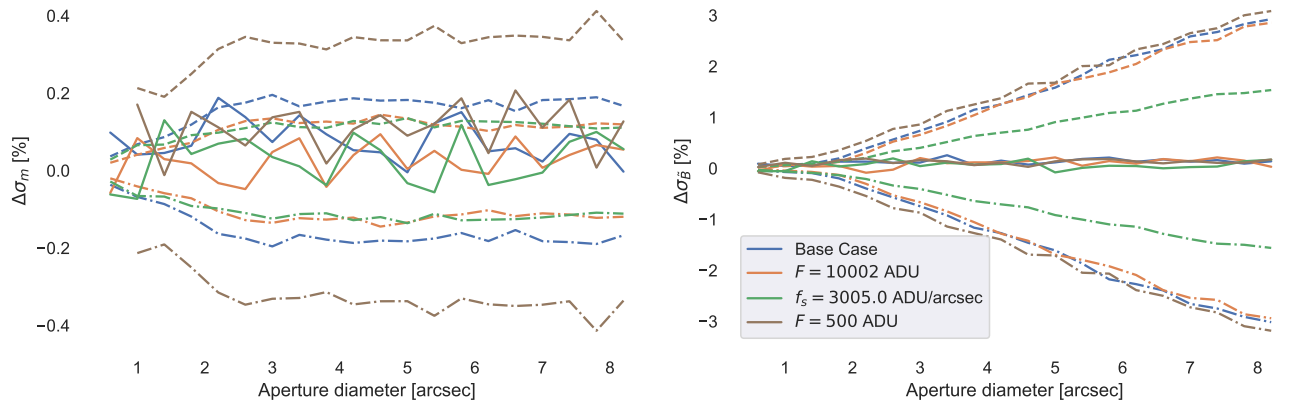

Figure 5.27: Performance discrepancies of the SWLS estimator for joint source flux (left) and background (right) estimation for different observational scenarios, under an aperture selection scheme. Dashed-dotted-, dashed- and solid lines denote the lower bound, the upper bound and the empirical variance estimate, respectively.

As can be seen in the figures, the estimator's variances lie between the upper and lower bounds, both for $\hat{\tilde{F}}$ and $\hat{\tilde{B}}$ and in all case studied (even those not shown).

Interestingly, the bounds corresponding to $\tau_{SWLS,1}(\cdot)$ do not vary much as aperture increases, which suggest some robustness or predictive power of the bounds themselves. On the other hand, the length of the interval in which $Var(\tau_{SWLS,2}(\cdot))$ is expected to lie becomes greater and greater with aperture, almost in a linear regime. Regardless, the empirical estimates tend to be closer to zero, *i.e.* to the fundamental limit of the Cramér-Rao bound itself. This suggest that the predictive power of each bound alone diminishes with aperture, but it seems to be enough evidence to expect a good performance in practice, which could be approximated as the mean of the bounds, or simply by $\sigma^2_{SWLS,2}$.

Lastly, it is interesting to visualize the estimates' distribution and the effect of aperture on it, which is shown in Figure 5.28. The figure is obtained by sampling a set of 25000 frames from the baseline scenario to feed the SWLS estimator using different aperture diameters.

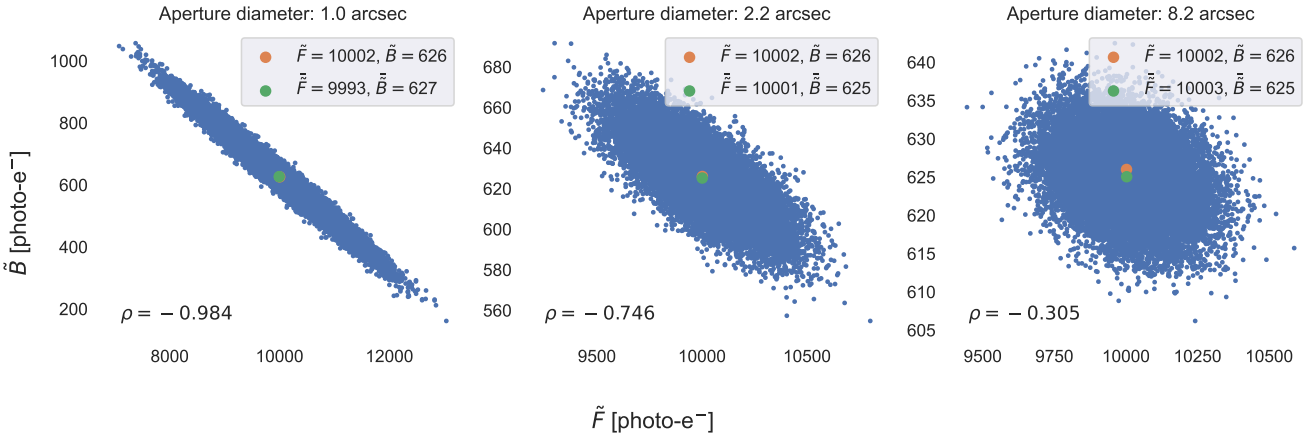

Figure 5.28: SWLS estimates distribution for the baseline scenario using different aperture diameters. Blue markers denote the pairs $(\hat{\tilde{F}}, \hat{\tilde{B}})$, orange marker is used for the ground truth value and green marker denotes the sample means. On the bottom-left corner of each graph the sample Pearson correlation coefficient is displayed. Estimates in each graph are obtained from the same sample set.

We start the analysis of Figure 5.28 by noting its consistency with the previous results shown in the current section: wider apertures lead to simultaneously increasing exactness and precision (less bias and variance, respectively), which is evidenced by the difference between the orange and green markers, and the reduction of scattering along both axes.

Another feature displayed in the figure is the relationship between correlation and aperture. As discussed in Section 4.1, the off-diagonal elements of $\mathcal{I}_\theta^{-1}$ hinted a negative correlation between both estimates and a decrease in its magnitude as more pixels are added in the inference process. In Figure 5.28 this is empirically evidenced by the increase of ρ and how the obtained distributions resemble a bivariate isotropic Gaussian distribution when we compare the graphs from left to right.

The reduction not only of the estimates' variances, but also of their covariance with aperture illustrates how important the information contained in the tails of the PSF about both parameters

when performing joint inference is. The information in that particular region allows to some extent to disambiguate the origin of detected photons across the whole detector. Naturally, this region serves the same purpose of estimating the background and substracting it prior to flux inference in more standard photometry procedures.

In light of these results, the overall outcome of the current section is the validation of the theoretical methodology developed earlier in this work, and to a lesser extent to further stress the gain in performance from increasing aperture in joint estimation.

Chapter 6

ML Estimator for Joint Source Flux and Background Estimation

Another interesting estimator to look after is the case of the Maximum Likelihood (ML) estimator. Given its asymptotic optimality [Kay, 1993] it has been widely used or inspired other works in the astronomy literature [Gai et al., 2017, Lindegren, 2008, Espinosa et al., 2018] and other research fields which face similar image processing problems such as fluorecence microscopy [Abraham et al., 2009, Small and Parthasarathy, 2014].

The likelihood function of some observation vector $\mathbf{I}$ given the source's relative position x_c and some point in the parameter space $\boldsymbol{\alpha} \in \boldsymbol{\Theta}$; and a set of indices $\mathcal{J} \subseteq \{1, \ldots, n\}$, can be rewritten as

$$L(\mathbf{I}; x_c, \boldsymbol{\alpha}) = \prod_{i \in \mathcal{J}} \frac{e^{-(\alpha_1 \cdot g_i(x_c) + \alpha_2)} \cdot (\alpha_1 \cdot g_i(x_c) + \alpha_2)^{I_i}}{I_i!}. \tag{6.1}$$

Therefore, the cost function that implicitly defines the ML estimator $\tau_{ML}(\mathbf{I})$ through a minimization problem can be obtained by taking the negative logarithm of $L(\mathbf{I}; x_c, \boldsymbol{\alpha})$, that is

$$\begin{aligned} J_{ML}(\boldsymbol{\alpha}, \mathbf{I}) &= -\ln L(\mathbf{I}; x_c, \boldsymbol{\alpha}) \\ &= \sum_{i \in \mathcal{J}} \alpha_1 \cdot g_i(x_c) + \alpha_2 - I_i \ln\left(\alpha_1 \cdot g_i(x_c) + \alpha_2\right) + \varpi, \end{aligned} \tag{6.2}$$

where $\varpi \equiv -\sum_{i \in \mathcal{J}} \ln(I_i!)$ is a constant (with respect to $\boldsymbol{\alpha}$). Then,

$$\tau_{ML}(\mathbf{I}) = \underset{\boldsymbol{\alpha} \in \boldsymbol{\Theta}}{\operatorname{argmin}} J_{ML}(\boldsymbol{\alpha}, \mathbf{I}). \tag{6.3}$$

As $\tau_{ML}(\mathbf{I})$ has no closed-form expression, we resort to the results presented in Section 3 to estimate its performance, which allows to assess its optimality relative to the Cramér-Rao bounds

studied in Section 4. Such an analysis relies mostly on computing expressions (3.5) and (3.8). The partial derivatives detailing such procedure can be found in Appendix E.

It is interesting however to note the following with respect to the values $\sigma^2_{ML,\tilde{F}}$ and $\sigma^2_{ML,\tilde{B}}$ defined as in Section 3: **if** we do assume[1] that $\tau(\bar{\mathbf{I}}) = \boldsymbol{\alpha}^\star$ it follows that

$$\nabla^{11} J_{ML}(\tau(\bar{\mathbf{I}}), \bar{\mathbf{I}}) = \begin{bmatrix} \frac{-g_{i_1}(x_c)}{\lambda_{i_1}(x_c,\tilde{F})} & \cdots & \frac{-g_{i_{|\mathcal{J}|}}(x_c)}{\lambda_{i_{|\mathcal{J}|}}(x_c,\tilde{F})} \\ \frac{-1}{\lambda_{i_1}(x_c,\tilde{F})} & \cdots & \frac{-1}{\lambda_{i_{|\mathcal{J}|}}(x_c,\tilde{F})} \end{bmatrix}, \tag{6.4}$$

and

$$\nabla^{20} J_{ML}(\tau(\bar{\mathbf{I}}), \bar{\mathbf{I}}) = \begin{bmatrix} \sum_{i\in\mathcal{J}} \frac{g_i^2(x_c)}{\lambda_i(x_c,\tilde{F})} & \sum_{i\in\mathcal{J}} \frac{g_i(x_c)}{\lambda_i(x_c,\tilde{F})} \\ \sum_{i\in\mathcal{J}} \frac{g_i(x_c)}{\lambda_i(x_c\tilde{F})} & \sum_{i\in\mathcal{J}} \frac{1}{\lambda_i(x_c,\tilde{F})} \end{bmatrix} = \mathcal{I}_{\boldsymbol{\alpha}^\star}, \tag{6.5}$$

from which we recover the same set of matrices which allowed us to show that the WLS estimator achieves optimality in the Cramér-Rao sense given the weights of equation (5.10) (see Appendix C). Consequently

$$\begin{aligned} &\left[\tau'_{ML}(\bar{\mathbf{I}})\right] \cdot Cov(\mathbf{I}) \cdot \left[\tau'_{ML}(\bar{\mathbf{I}})\right]^\intercal = \mathcal{I}_{\boldsymbol{\alpha}^\star} \\ \Rightarrow\ &\sigma^2_{ML,\tilde{F}} = \left[\mathcal{I}^{-1}_{\boldsymbol{\alpha}^\star}\right]_{(1,1)} \ \wedge\ \sigma^2_{ML,\tilde{B}} = \left[\mathcal{I}^{-1}_{\boldsymbol{\alpha}^\star}\right]_{(2,2)}. \end{aligned} \tag{6.6}$$

This last equation translates into that the interval enclosing the variance of the respective ML estimates is centered precisely at the Cramér-Rao bound associated to each of the target parameters.

6.1 Numerical Analysis

In this section we review the behavior of the performance bounds, as developed in Section 3, related to the Maximum Likelihood estimator, as well as its empirical exactness and precision relative to said bounds. For that matter we recall on the different study cases derived from the so called "base case" from previous sections.

6.1.1 Bias Bounds

Unbiasedness is a key feature of any estimator, particularly when taking its precision relative to the Cramér-Rao bound. Let's begin our analysis with the bound for the estimator's absolute bias, described as in equation 3.5. Figure 6.1 assesses the bounds relative to the values of the target

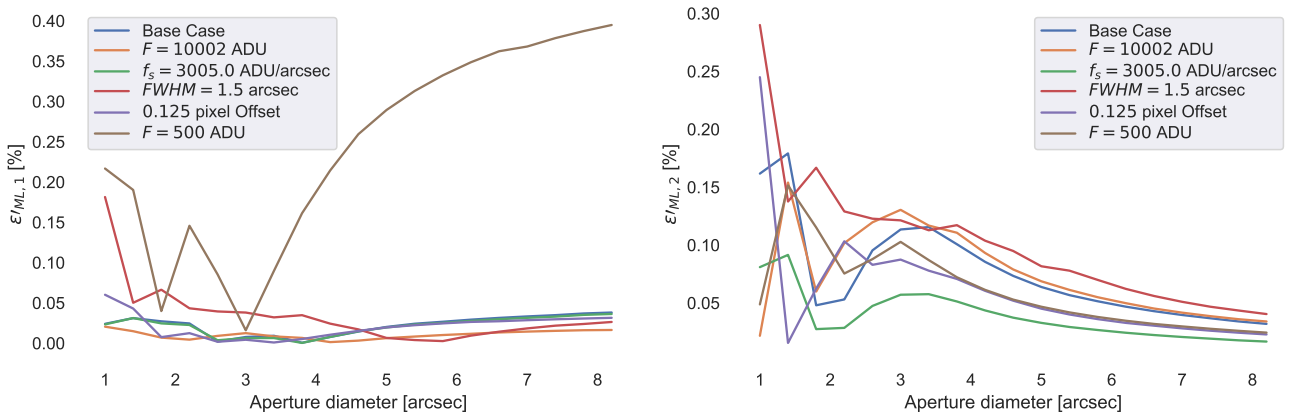

Figure 6.1: Bias bounds for joint source flux (left) and background (right) estimation for different observational scenarios, under an aperture selection scheme.

parameters, i.e. they are measured as $100 \times \frac{\varepsilon'_{ML,1}}{\tilde{F}}$ and $100 \times \frac{\varepsilon'_{ML,2}}{\tilde{B}}$, respectively, under the aperture pixel selection scheme.

As long as (most of) the target's PSF is not covered, the bounds seem to follow an irregular oscillating but overall decreasing behavior, which is then followed by a clear tendency:

- The curve corresponding to the object's flux increases slightly until it stabilizes. We note two apparent exceptions, which correspond to the fainter cases where the source's light is either weaker ($F = 500$ ADU) or more diffuse ($FWHM = 1.5$ arcsec).
- After slightly increasing, the curves related to background monotonically decreases.

Despite the apparent dynamics of the bounds as aperture increases, we note that none of them achieves values higher than a hundredth of a percent. Therefore, the mathematical bounds of Section 3 predict that the joint ML estimator achieves 0 bias and, consequently, measuring its precision against the Cramér-Rao bounds is feasible and meaningful.

6.1.2 Variance Bounds

As the Maximum Likelihood estimator is theoretically unbiased, we now review the two elements that conform the interval depicted in equation (3.8). On one hand we have the central value, $\sigma^2_{ML,j}$ and on the other we have $\beta_{ML,j}$ which defines the length of the interval by $2\beta_{ML,j}$.

For the one-dimensional case, Espinosa et al. [Espinosa et al., 2018] described $\sigma^2_{ML,j}$ as the linear tendency of the estimator's variance. Being the p-dimensional extension very similar (as we are interested mostly on the diagonal components of the estimator's covariance matrix), that interpretation of $\sigma^2_{ML,j}$ is still applicable in our scenario and very useful, particularly when we compare it against the fundamental limits resulting from the posed problem. For that matter, Figure 6.2 shows the relative discrepancy between $\sigma^2_{ML,1}$ and $\sigma^2_{ML,2}$, and the respective Cramér-Rao bounds.

[1]Which we do not do formally in this work beyond this remark, however.

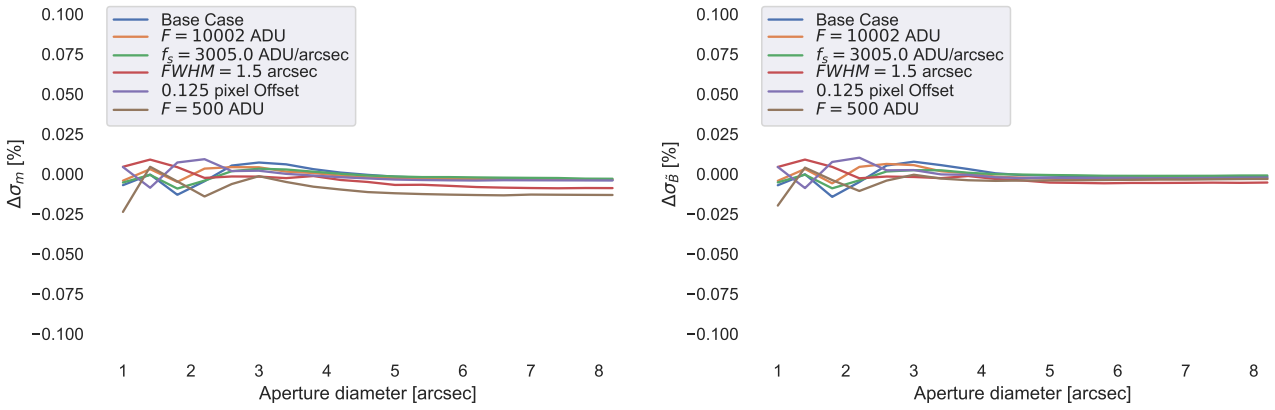

Figure 6.2: Performance discrepancies between $\sigma^2_{ML,\tilde{F}}$ (left), $\sigma^2_{ML,\tilde{B}}$ (right) and their respective Cramér-Rao bounds, for different observational scenarios, under an aperture selection scheme.

We notice some similarities between the overall tendencies of the curves in Figure 6.2 and the behavior of the bounds shown in the previous section, as two phases can be recognized: there is a transient stage that emerges for narrower apertures, followed by a steady smooth stage. Even more, it is shown, again, that the cases corresponding to fainter sources (either weaker or more diffuse) slightly deviate from the tendency of other scenarios.

The more interesting feature in these figures is that all the curves lie in a narrow area around 0%, which indicates that our bounding strategy predicts that the ML estimator is very close to be optimal as long as the values of $\beta_{ML,\tilde{F}}$ and $\beta_{ML,\tilde{B}}$ are small enough. It is also remarkable that both $\sigma^2_{ML,\tilde{F}}$ and $\sigma^2_{ML,\tilde{B}}$ resemble equation (6.6), even if we did not assume $\tau_{ML}(\bar{\mathbf{I}}) = (\tilde{F}, \tilde{B})$. Consequently, for those scenarios for which we have fainter sources and negative values for discrepancy, optimality could still be achieved if the predicted interval is long enough.

The length of the bounding intervals as aperture increases is shown in Figure 6.3. As can be observed, wider exposition areas and information availability allows the predicted intervals to become narrower. Therefore, our methodology foretells that the Maximum Likelihood estimator is capable of extracting both flux and background information from pixels farther from the object's position to allow for better precision. This added to the results obtained in Figure 6.2, indicate that the estimator's performance must become closer and closer to the optimal values dictated by the Cramér-Rao bounds. Using the interpretation of Espinosa et al. [Espinosa et al., 2018], Figure 6.3 shows that the relevance of the non-linear component of the estimator's variance diminishes as more information is incorporated into the inference process, restricting the performance to stick close to the linear one, which in turn lies tightly close to the Cramér-Rao bounds.

Finally, it is interesting to contrast these results with the analysis obtained for the SWLS estimator in Section 5.2.2, which offered performance bounds that became looser with aperture, even though empirical performance was not harmed.

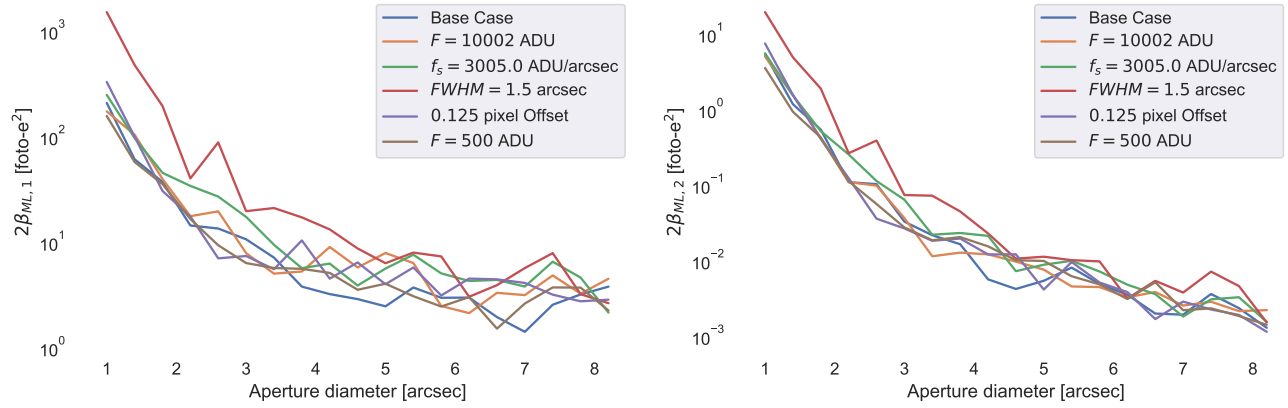

Figure 6.3: Length of the bounding intervals, $2\beta_{ML,j}$ for $j \in \{1, 2\}$ for different observational scenarios, under an aperture selection scheme.

6.1.3 Empirical Performance

Up to this moment, only the promising theoretical behavior of the ML estimator has been discussed, but empirical analysis has not been addressed yet. Here, we compare the estimator's empirical performance both with the bias and variance bounds already discussed.

Starting with the analysis on bias, Figure 6.4 compares the bounds shown in Section 6.1.1, for some of the study cases. The figure displays how the values for $\varepsilon'_{ML,\tilde{F}}$ and $\varepsilon'_{ML,\tilde{B}}$ successfully bound the empirical performance of the ML estimator in terms of bias. These bias bounds are particularly accurate once good coverage of the PSF has been achieved, particularly for background estimates, which offer a consistent margin between the respective curves.

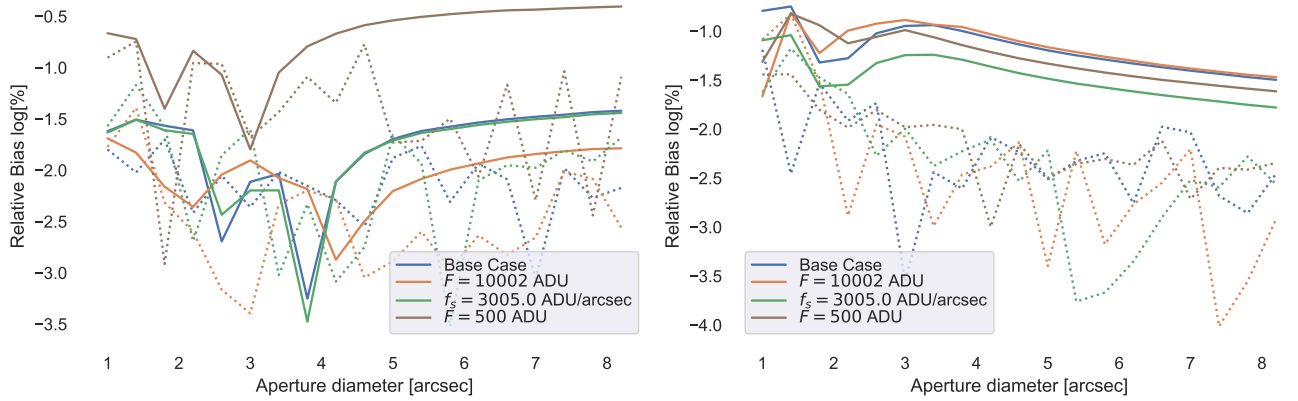

Figure 6.4: Relative biases for joint source flux (left) and background (right) estimation for different observational scenarios, under an aperture selection scheme. Solid lines denote the corresponding bounds as given by equation (3.5) while dotted lines are employed for empirical bias estimates.

In conclusion, as the empirical bias achieved by the ML estimates goes even lower than the tight bounds given by the methodology of Section 3, we can establish that the Maximum Likelihood estimator is, in fact, unbiased for all practical purposes.

Moving into the variance estimator's behavior, Figure 6.5 offers a first look on that behalf. The figure shows that the curves for each one of the studied scenarios are so close to each other that they are indistinguishable from the other, at least when we display the results in units of magnitudes for the source's brightness and photons for the background. These results suggest that the Maximum Likelihood estimators follows the Cramér-Rao limits very closely, just as predicted by the analysis of the linear component of its variance in the previous section.

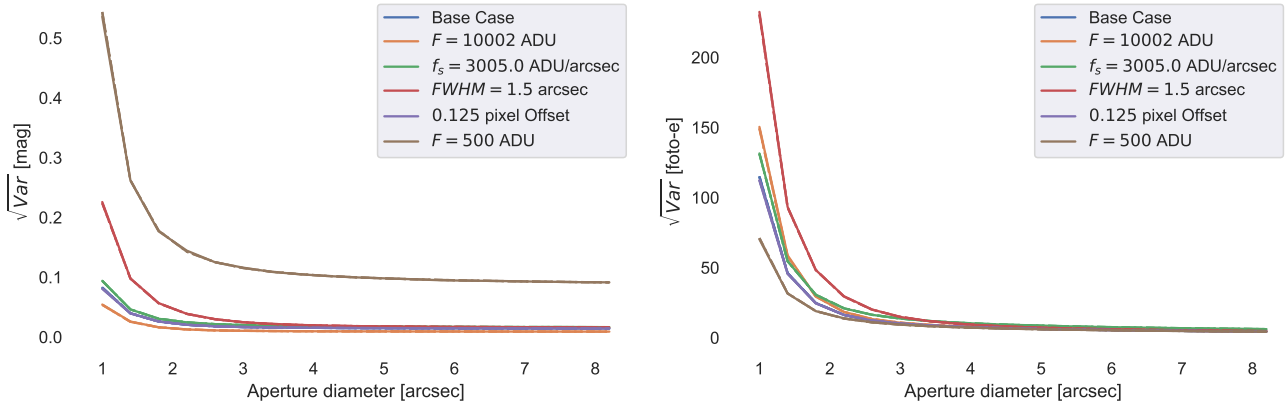

Figure 6.5: Variance bounds of the ML estimator for joint source flux (left) and background (right) estimation for different observational scenarios, under an aperture selection scheme. Dashed-dotted-, dashed- and solid lines denote the lower bound, the upper bound and the empirical variance estimate, respectively.

When we re-scale the curves relative to the CRLBs by taking discrepancies, $\Delta\sigma_m$ and $\Delta\sigma_{\tilde{B}}$, in order to normalize the global tendency given by $\sigma^2_{ML,\cdot}$, we notice how the predicted bounds seem to be unable to encompass the estimator's actual performance within a certain range, as can be observed in Figure 6.6.

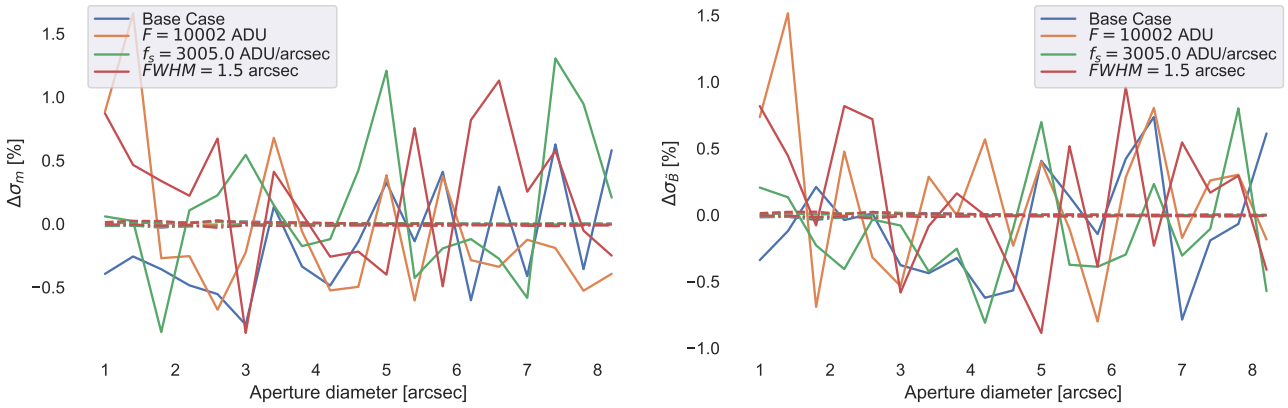

Figure 6.6: Performance discrepancies of the ML estimator for joint source flux (left) and background (right) estimation for different observational scenarios, under an aperture selection scheme. Dashed-dotted-, dashed- and solid lines denote the lower bound, the upper bound and the empirical variance estimate, respectively.

Though this results may seem unfavorable, given the erratic oscillations of the empirical curves

around 0% and their relatively small amplitude, such behavior can be attributed to numerical artifacts resulting from computational limitations such as numerical resolution (which is particularly critical when computing the quantified PSF, $g_i(x_c), i \in \mathcal{J}$), stopping criteria required by the optimization solvers, or the very own rules of the programming languages themselves. Another possible reason to explain this discrepancy may be the optimization over the linear interpolation parameter t, on which the methodology heavily depends (see Section 3). However, for the particular problem studied here it did not seem to have much of an impact on the bounds' calculation.

Overall, the difference in terms of discrepancy tends to be around 0.5% (and from previous evidence already discussed for other estimators such as SWLS), for which it can be established that the proposed methodology is successful at predicting that the joint Maximum Likelihood estimator is very close to be optimal for a wide range of scenarios and apertures.

Just as was done for the SWLS estimator in Section 5.2.2, we now show in Figure 6.7 the distribution of a sample set of estimates obtained with the ML estimator and the effect of aperture diameter on it. In fact, the same sample set used for Figure 5.28 was used here for inference.

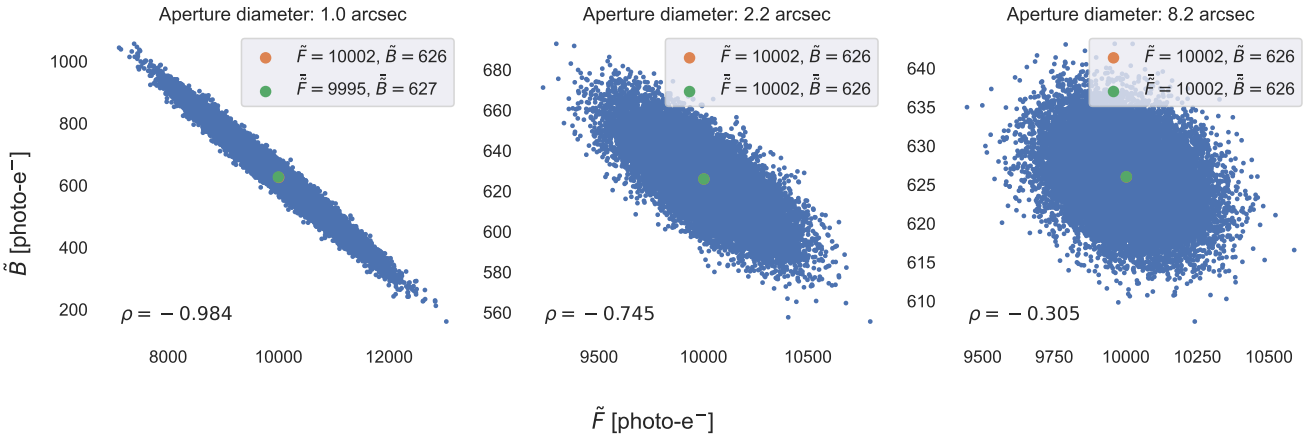

Figure 6.7: ML estimates distribution for the baseline scenario using different aperture diameters. Blue markers denote the pairs $(\hat{\tilde{F}}, \hat{\tilde{B}})$, orange marker is used for the ground truth value and green marker denotes the sample means. On the bottom-left corner of each graph the sample Pearson correlation coefficient is displayed. Estimates in each graph are obtained from the same sample set.

In general, the same analysis and commentaries for the SWLS distributions of Figure 5.28 apply for Figure 6.7, as not only bias and variance decrease with wider apertures (which is consistent with previous results shown in this section), but also correlation does. Furthermore, the corresponding distributions for the SWLS and ML estimators are almost identical, which is expected as both estimators showed empirically to be very close to optimallity in the Cramér-Rao sense (see Figures 5.26 and 6.5 for example) and the difference between the respective calculated correlation coefficient is at most 0.001.

However, the empirical exactness of the ML estimator in Figure 6.7 tends to outperform that of Figure 5.28 as it consistently shows that for all tested apertures the ML estimates' mean is closer to the target values than the SWLS ones, even for apertures of 1.0″ and 2.2″ where there's more scattering over the flux-background space, which suggests that the ML estimator is more efficient

in terms of pixel-information use.

6.2 Using the Bounds as an Implementation-Validation Tool

The results shown previously in this section were developed with the *Stan* probabilistic programming language [Carpenter et al., 2017, Stan Development Team, 2019], particularly its *PyStan* interface [Riddell et al., 2021], using as optimizer the Newton method [Nocedal and Wright, 2006]. However, the *Stan* language offers other quasi-Newton algorithms for optimization. For further comparison, we present in this section the results obtained with a Maximum Likelihood estimator implemented with the *SciPy* [Virtanen et al., 2020] package.

Calculation of the bounds obtained as in the procedure proposed in Section 3 is quite consistent when using different implementations of the same algorithm, that is, by developing different approaches to solve a given optimization functional, whether by employing different solvers or programming languages. For that reason we present an alternative application of the tools developed here, that of testing and validating those implementations of the estimator.

Evidence of the mentioned consistency is presented in Figure 6.8, where the upper bounds for the variances' squared root calculated from different implementations of the ML estimator, considering both the package and the optimization solver implemented, are compared. The displayed bounds correspond to the base scenario previously presented in Section 4, though similar results are found for other study cases.

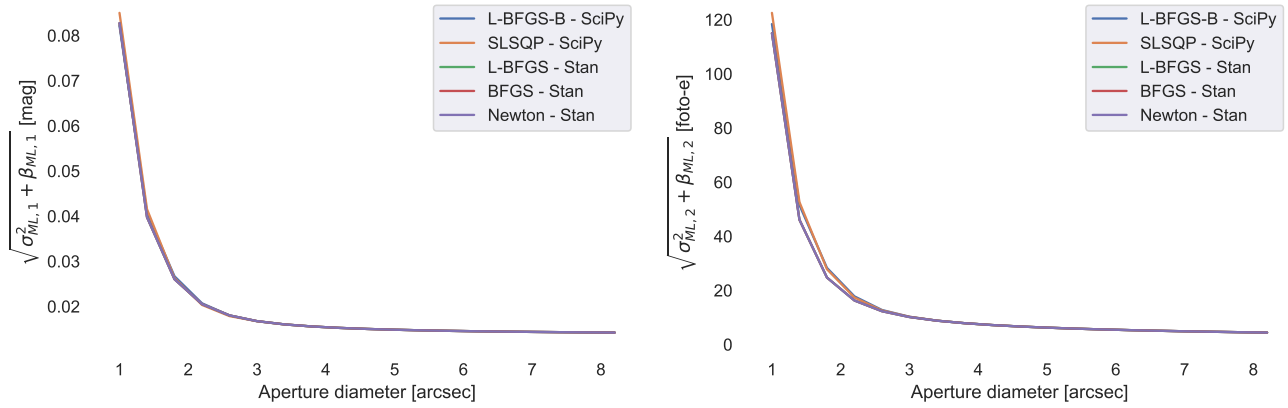

Figure 6.8: Upper bounds for the ML estimates' variances for different implementations of the algorithm.

From the figure, it is interesting to note that for aperture diameters greater than three times the FWHM the difference between the curves for different implementations of the ML estimator diminishes. This trend indicates that the information gain obtained from more pixels translates into more consistent bounds among different implementations of an estimation algorithm. This consistent behavior strengthen the idea of using more pixel inputs when performing joint inference.

However, the fact that the bounds calculated with different implementations take very similar values does not imply that the estimators behave the exact same way in practice.

Having demonstrated that the ML estimator implemented by means of the *Stan*'s Newton optimization algorithm allows for congruent results between the empirical and predicted performances, and that the bounding strategy is itself consistent by obtaining similar bounding values from different languages and optimization algorithms, we can compare solely the empirical performances of the tested ML implementations.

Figure 6.9 displays the empirical standard deviation obtained with the reviewed optimization methods, for our baseline scenario. Therein, we notice how the *Stan*-implemented estimators perform quite the same, attaining discrepancies similar to the ones seen in Section 6.1.3. On the other hand, the estimators programmed with *SciPy* perform poorly[2], even counteracting the prescriptions for information use proposed in this work by showing worsening precision on the object's brightness as aperture increases. As for the background estimates, though the figure shows a gain in precision with aperture, they still perform unsatisfactorily when compared with the CRLB.

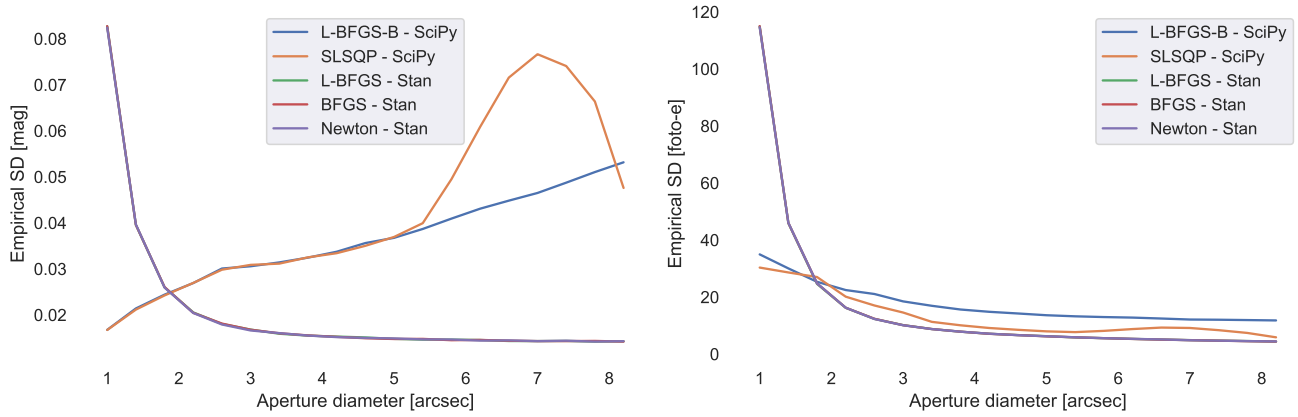

Figure 6.9: Empirical performances for different implementations of the ML estimator.

Through this kind of analysis, the developer or end user could detect the presence of implementation issues and then make decisions such as inspecting the code searching for possible improvements such as: parameter tweaking, better initial guesses for the algorithms; or, as could be the case in this scenario, to straightforwardly discard those that do not match the expected behavior. This way, the bounds developed in Section 3 offer a relevant framework for the development stages as part of the testing and validation processes.

[2]Note however that *SciPy* offers plenty of alternative optimization algorithms which may improve the ones reviewed here.

Chapter 7

Conclusions and Future Work

In this work we studied both theoretical and practical implications of performing simultaneous estimation of the brightness of a targeted point light source and the background flux that source is embedded in. We also explored the effects of incorporating as much pixel information as possible to this joint inference process, which should allow for better precision.

From a theoretical perspective, we show how fundamental precision limits behaves under different increasing-aperture schemes and observational settings. We demonstrate a decreasing trend on the minimal variance, across a wide range of SNR regimes. This supports the idea that there are performance benefits when adopting the principle of joint estimation with wider apertures.

Classic results on parametric inference and sufficient statistics were unable to provide closed-form definitions for an estimator that could guarantee achievability of the Cramér-Rao bounds thoroughly studied. For that matter, we resort to a newly formulated generalization of the results of Fessler [Fessler, 1996] and Espinosa et al. [Espinosa et al., 2018] on implicit estimators to assess practical strategies to approach the posed multidimensional problem of joint inference.

We tested a handful of variants of the Weighted Least-Squares (WLS) estimator to validate both the concept of joint inference and the developed mathematical tools for performance bounding from an experimental standpoint. For the former, the various flavors of the estimator proved to be unbiased and displayed a performance comparable to the fundamental limits, particularly when provided with adaptable weight-choice schemes. For the latter task, our bounding methodology displayed consistency with the linear nature of the plain WLS estimator, posed as a border case. For adaptive versions of the WLS estimator, our methodology successfully bound its performance both bias- and variance-wise, achieving less than 1% discrepancy with respect to the minimal achievable variance bounds.

For the Maximum Likelihood (ML) estimator our bounding strategy successfully predicts its unbiasedness. Regarding the precision forecasts, the developed bounds suggest tight correspondence between the Cramér-Rao bounds and the central value of interval where each of the ML estimates' variances belongs. Furthermore, as pixel information increases, the intervals' length becomes tighter, which implies closeness to the minimal possible variance. Though our bounds weren't capable to precisely determine the ML estimates' variance, the relatively small gap be-

tween empirical results and our lower and upper bound predictions (around 1% with respect to the Cramér-Rao bounds), added to the accurate prediction of the global tendencies leads us to state the consistent near-optimality of the ML scheme.

Finally we tested the developed performance bounding strategy as a way of validating the implementation of an inference algorithm. We showed how different implementations convey similar theoretical bounds, despite their empirical performances can broadly differ, thus allowing to discard non-consistent versions and select those consistent with our predicted bounds.

As future work, we recognize two important branches that may expand the analyses and findings of the current thesis.

Our general multidimensional formulations can be used to increase the dimension of the inference problem by adding the source's relative position as a third unknown parameter. Then we can explore the problem adressed by Gai et al. [Gai et al., 2017]. Furthermore, concurrent PSF inference could be studied, possibly adding multiple degrees of complexity to our problem.

It may be also interesting to tackle the very same problem faced in this work but with a Bayesian perspective. Bayesian inference also offers fundamental limits in the form of Bayesian Cramér-Rao bounds, which could be used to study possible information gains due to prior information. Then, the performance bounding tool proposed in this work, posed for optimization problems may be extended to this framework too, for example for the MAP estimator.

Regarding the bounding strategy adopted in this thesis, further work can be done in order to develop tighter bounds. Finally, on the algorithmic behalf, there's room for studying and improving the optimization methods which allow to calculate the bounds when maximizing over the linear interpolation term $t \in [0, 1]$.

To end this work in a more comprehensive manner, Table 7.1 summarizes the main contributions and key points of each chapter.

Table 7.1: Main conclusions per chapter.

Chapter N°	**Contributions**
3	• Development of generalized bias (eqn. (3.5) and variance (eqns. (3.6) and (3.7)) bounds for multidimensional implicit estimators.
4	• Thorough analysis of the Cramér-Rao Bounds for joint photometry (see eqns. (4.12), (4.13) and (4.14)). • It's proven that as more pixels are available for inference (independent of how they're chosen), the lower the one-dimensional and joint CRLBs become, and the more they resemble each other (see Figures 4.3 and 4.6). • No estimator that achieved the CRLBs could be found (see eqn. (4.24) for example). Therefore, the optimallity of practical estimators must be assessed.
5	• The WLS joint estimates can be unbiased and very precise, depending on weight setting. Adaptive versions of it show to be near-optimal (see Figure 5.17for example). • Results like Figure 5.17 suggest that there exists a *sufficient* aperture rather than an *optimal* one when performing joint photometry. • The methodology of Chapter 3 is validated through the adaptive SWLS estimator (see Figure 5.27).
6	• The ML joint estimates show to be unbiased, near-optimal and less correlated as aperture increases (see Figures 6.4, 6.5 and 6.7). • The bounds of Chapter 3 can also be used as validation tool for different implementations of an algorithm (see Figures 6.8 and 6.9).

Bibliography

[Abraham et al., 2009] Abraham, A. V., Ram, S., Chao, J., Ward, E. S., and Ober, R. J. (2009). Quantitative study of single molecule location estimation techniques. *Opt. Express*, 17(26).

[Bertin, E. and Arnouts, S., 1996] Bertin, E. and Arnouts, S. (1996). SExtractor: Software for source extraction. *Astron. Astrophys. Suppl. Ser.*, 117(2).

[Bickerton and Lupton, 2013] Bickerton, S. J. and Lupton, R. H. (2013). An algorithm for precise aperture photometry of critically sampled images. *Monthly Notices of the Royal Astronomical Society*, 431(2).

[Carpenter et al., 2017] Carpenter, B., Gelman, A., Hoffman, M. D., Lee, D., Goodrich, B., Betancourt, M., Brubaker, M., Guo, J., Li, P., and Riddell, A. (2017). Stan: A probabilistic programming language. *Journal of statistical software*, 76(1).

[Carroll and Ostlie, 2014] Carroll, B. W. and Ostlie, D. A. (2014). *An Introduction to Modern Astrophysics*. Pearson Education, 2nd edition.

[Cover and Thomas, 2006] Cover, T. M. and Thomas, J. A. (2006). *Elements of Information Theory*. John Wiley & Sons, 2nd edition.

[Cramér, 1946] Cramér, H. (1946). A contribution to the theory of statistical estimation. *Scandinavian Actuarial Journal*, 1946(1).

[Diago, 2010] Diago, P. D. (2010). *Asteroseismology and mass loss in Be stars. Study with CoRoT*. Ph.D. dissertation, Universitat de València.

[Eldar, 2008] Eldar, Y. C. (2008). Rethinking biased estimation: Improving maximum likelihood and the cramér–rao bound. *Foundations and Trends® in Signal Processing*, 1(4).

[Espinosa et al., 2018] Espinosa, S., Silva, J. F., Mendez, R. A., Lobos, R., and Orchard, M. (2018). Optimality of the maximum likelihood estimator in astrometry. *Astronomy & Astrophysics*, 616(A95).

[Fessler, 1996] Fessler, J. A. (1996). Mean and variance of implicitly defined biased estimators (such as penalized maximum likelihood): Applications to tomography. *IEEE Transactions on Image Processing*, 5(3).

[Gai et al., 2017] Gai, M., Busonero, D., and Cancelliere, R. (2017). Performance of an algorithm

for estimation of flux, background, and location on one-dimensional signals. *Publications of the Astronomical Society of the Pacific*, 129(975).

[Guglielmetti, 2010] Guglielmetti, F. (2010). *Background–Source separation in astronomical images with Bayesian Probability Theory*. Ph.D. dissertation, Ludwig–Maximilians–Universität.

[Guglielmetti et al., 2009] Guglielmetti, F., Fischer, R., and Dose, V. (2009). Background-source separation in astronomical images with Bayesian probability theory-I. The method. *Monthly Notices of the Royal Astronomical Society*, 396(1).

[Handberg et al., 2021] Handberg, R., Lund, M. N., White, T. R., Hall, O. J., Buzasi, D. L., Pope, B. J. S., Hansen, J. S., von Essen, C., Carboneau, L., Huber, D., Vanderspek, R. K., Fausnaugh, M. M., Tenenbaum, P., and Jenkins, J. M. (2021). TESS data for asteroseismology: Photometry. *The Astronomical Journal*, 162(4).

[Howell, 1989] Howell, S. B. (1989). Two-dimensional aperture photometry: Signal-to-noise ratio of point-source observations and optimal data-extraction techniques. *Publications of the Astronomical Society of the Pacific*, 101(640).

[Howell, 2006] Howell, S. B. (2006). *Handbook of CCD Astronomy*. Cambridge University Press, 2nd edition.

[Janesick, 2001] Janesick, J. R. (2001). *Scientific Charge-Coupled Devices*. SPIE Press, 1st edition.

[Janesick, 2007] Janesick, S. B. (2007). *Photon Transfer*. SPIE Press, 1st edition.

[Johansson et al.,] Johansson, F. et al. mpmath: a Python library for arbitrary-precision floating-point arithmetic (version 1.2.1). `http://mpmath.org/`.

[Kay and Eldar, 2008] Kay, S. and Eldar, Y. C. (2008). Rethinking biased estimation [lecture notes]. *IEEE Signal Processing Magazine*, 25(3).

[Kay, 1993] Kay, S. M. (1993). *Fundamentals of Statistical Signal Processing. Estimation Theory*. Prentice Hall, 1st edition.

[Levy, 2008] Levy, B. C. (2008). *Principles of Signal Detection and Parameter Estimation*. Springer, 1st edition.

[Lindegren, 2008] Lindegren, L. (2008). A general Maximum-Likelihood algorithm for model fitting to CCD sample data. Technical Report GAIA-C3-TN-LU-LL-078-01, Lund Observatory.

[Lobos et al., 2015] Lobos, R. A., Silva, J. F., Mendez, R. A., and Orchard, M. (2015). Performance analysis of the least-squares estimator in astrometry. *Publications of the Astronomical Society of the Pacific*, 127(957).

[McLean, 2008] McLean, I. S. (2008). *Electronic Imaging Astronomy: Detectors and Instrumentation*. Springer, 2nd edition.

[Mendez et al., 2010] Mendez, R. A., Costa, E., Pedreros, M. H., Moyano, M., Altmann, M., and

Gallart, C. (2010). Proper motions of local group dwarfs spheroidal galaxies I: First ground-based results for fornax. *Publications of the Astronomical Society of the Pacific*, 122(893).

[Mendez et al., 2013] Mendez, R. A., Silva, J. F., and Lobos, R. (2013). Analysis and interpretation of the Cramér-Rao lower-bound in astrometry: One-dimensional case. *Publications of the Astronomical Society of the Pacific*, 125(927).

[Mendez et al., 2014] Mendez, R. A., Silva, J. F., Oróstica, R., and Lobos, R. (2014). Analysis of the Cramér-Rao bound in the joint estimation of astrometry and photmetry. *Publications of the Astronomical Society of the Pacific*, 126(942).

[Naylor, 1998] Naylor, T. (1998). An optimal extraction algorithm for imaging photometry. *Monthly Notices of the Royal Astronomical Society*, 296(2).

[Nocedal and Wright, 2006] Nocedal, J. and Wright, S. J. (2006). *Numerical Optimization*. Springer, 2nd edition.

[Perryman et al., 1989] Perryman, M. A. C., Jakobsen, P., Colina, L., Lelièvre, G., Macchetto, F., Nieto, J. L., and di Serego Alighieri, S. (1989). An improved technique for the search for optical emission from radio pulsars, and its application to PSR 0301 + 19, 1919 + 21 and 2303 + 30 ⋆. *Astronomy and Astrophysics*, 215(1).

[Rao, 1945] Rao, C. R. (1945). Information and the accuracy attainable in the estimation of statistical parameters. *Bulletin of the Calcutta Mathematical Society*, 37(3).

[Riddell et al., 2021] Riddell, A., Hartikainen, A., and Carter, M. (2021). Pystan (3.0.0). `https://pypi.org/project/pystan/3.0.0/`.

[Ross, 1996] Ross, S. M. (1996). *Stochastic Processes*. John Wiley & Sons, 2nd edition.

[Small and Parthasarathy, 2014] Small, A. R. and Parthasarathy, R. (2014). Superresolution localization methods. *Annual Review of Physical Chemistry*, 65(1).

[Stan Development Team, 2019] Stan Development Team (2019). Stan modeling language users guide and reference manual, 2.29. `https://mc-stan.org`.

[Virtanen et al., 2020] Virtanen, P., Gommers, R., Oliphant, T. E., Haberland, M., Reddy, T., Cournapeau, D., Burovski, E., Peterson, P., Weckesser, W., Bright, J., van der Walt, S. J., Brett, M., Wilson, J., Millman, K. J., Mayorov, N., Nelson, A. R. J., Jones, E., Kern, R., Larson, E., Carey, C. J., Polat, İ., Feng, Y., Moore, E. W., VanderPlas, J., Laxalde, D., Perktold, J., Cimrman, R., Henriksen, I., Quintero, E. A., Harris, C. R., Archibald, A. M., Ribeiro, A. H., Pedregosa, F., van Mulbregt, P., and SciPy 1.0 Contributors (2020). SciPy 1.0: Fundamental Algorithms for Scientific Computing in Python. *Nature Methods*, 17(3).

[Winick, 1986] Winick, K. A. (1986). Cramér–Rao lower bounds on the performance of charge-coupled-device optical position estimators. *Journal of the Optical Society of America A*, 3(11).

Annex A

Proof: Bounding the Performance of a high-dimensional Implicit Estimator

Let $\boldsymbol{\Theta} \subseteq \mathbb{R}^p$ be some parameter space with $\boldsymbol{\alpha} \in \boldsymbol{\Theta}$ a p-dimensional parameter vector to be estimated from a n-dimensional observation vector $\mathbf{I}$, and let $J : \boldsymbol{\Theta} \times \mathbb{R}^n \to \mathbb{R}$ be the objective function of some optimization problem which defines a decision rule $\tau_J(\cdot)$ as

$$\tau_J(\mathbf{I}) \equiv \underset{\boldsymbol{\alpha} \in \boldsymbol{\Theta}}{\operatorname{argmin}} J(\boldsymbol{\alpha}, \mathbf{I}). \tag{A.1}$$

Let's also make the assumption that the cost function $J(\boldsymbol{\alpha}, \mathbf{I})$ has a unique optimal value at $\boldsymbol{\alpha} = \tau_J(\mathbf{I})$ which also satisfies the following first order condition

$$\begin{aligned} \mathbf{0} = \nabla J(\boldsymbol{\alpha}, \mathbf{I})\Big|_{\boldsymbol{\alpha}=\tau_J(\mathbf{I})} &= [J'(\boldsymbol{\alpha}, \mathbf{I})]^{\mathsf{T}}\Big|_{\boldsymbol{\alpha}=\tau_J(\mathbf{I})} \\ &= \begin{bmatrix} \frac{\partial}{\partial \alpha_1} J(\tau_J(\mathbf{I}), \mathbf{I}) \\ \vdots \\ \frac{\partial}{\partial \alpha_p} J(\tau_J(\mathbf{I}), \mathbf{I}) \end{bmatrix}. \end{aligned} \tag{A.2}$$

Assuming the functional $J(\boldsymbol{\alpha}, \mathbf{I})$ to be (at least) twice differentiable, the estimator's Taylor expansion around the mean vector $\bar{\mathbf{I}}$ is as follows:

$$\tau_J(\mathbf{I}) \approx \tau_J(\bar{\mathbf{I}}) + \tau_J'(\bar{\mathbf{I}}) \cdot (\mathbf{I} - \bar{\mathbf{I}}) + e(\bar{\mathbf{I}}, \mathbf{I} - \bar{\mathbf{I}}), \tag{A.3}$$

where

$$\begin{aligned}\mathbf{e}(\bar{\mathbf{I}}, \mathbf{I}-\bar{\mathbf{I}}) &= \frac{1}{2}\sum_{i=1}^{n}\sum_{h=1}^{n}\frac{\partial^2}{\partial I_i \partial I_h}\tau_J(\bar{\mathbf{I}}+t(\mathbf{I}-\bar{\mathbf{I}}))(I_i-\bar{I}_i)(I_h-\bar{I}_h) \\ &= \frac{1}{2}\sum_{i=1}^{n}\sum_{h=1}^{n}\begin{bmatrix} \frac{\partial^2}{\partial I_i \partial I_h}\tau_{J,1}(\bar{\mathbf{I}}+t(\mathbf{I}-\bar{\mathbf{I}})) \\ \vdots \\ \frac{\partial^2}{\partial I_i \partial I_h}\tau_{J,p}(\bar{\mathbf{I}}+t(\mathbf{I}-\bar{\mathbf{I}})) \end{bmatrix}(I_i-\bar{I}_i)(I_h-\bar{I}_h),\end{aligned} \tag{A.4}$$

for some fixed but unknown value $t \in [0,1]$.

By mere properties of the covariance matrix, the Taylor expansion in equation (A.3) can also be used to approximate the covariance matrix of the estimator τ_J:

$$\begin{aligned}Var(\tau_J(\mathbf{I})) \approx & Var(\tau_J(\bar{\mathbf{I}}) + \tau_J'(\bar{\mathbf{I}})\cdot(\mathbf{I}-\bar{\mathbf{I}}) + e(\bar{\mathbf{I}}, \mathbf{I}-\bar{\mathbf{I}})) \\ = & Var(\tau_J'(\bar{\mathbf{I}})\cdot(\mathbf{I}-\bar{\mathbf{I}}) + e(\bar{\mathbf{I}}, \mathbf{I}-\bar{\mathbf{I}})) \\ = & Var(\tau_J'(\bar{\mathbf{I}})\cdot(\mathbf{I}-\bar{\mathbf{I}})) + Cov(\tau_J'(\bar{\mathbf{I}})\cdot(\mathbf{I}-\bar{\mathbf{I}}), e(\bar{\mathbf{I}}, \mathbf{I}-\bar{\mathbf{I}})) \\ & + Cov(e(\bar{\mathbf{I}}, \mathbf{I}-\bar{\mathbf{I}}), \tau_J'(\bar{\mathbf{I}})\cdot(\mathbf{I}-\bar{\mathbf{I}})) + Var(e(\bar{\mathbf{I}}, \mathbf{I}-\bar{\mathbf{I}})).\end{aligned} \tag{A.5}$$

Noting that

$$\begin{aligned}\mathbb{E}_{\mathbf{I}\sim L(\mathbf{I};\boldsymbol{\alpha}^\star)}\left\{\tau_J'(\bar{\mathbf{I}})\cdot(\mathbf{I}-\bar{\mathbf{I}})\right\} &= \tau_J'(\bar{\mathbf{I}})\cdot\mathbb{E}_{\mathbf{I}\sim L(\mathbf{I};\boldsymbol{\alpha}^\star)}\left\{\mathbf{I}-\bar{\mathbf{I}}\right\} \\ &= \mathbf{0},\end{aligned} \tag{A.6}$$

the first element on the right-hand side of equation (A.5) can be expressed as

$$Var(\tau_J'(\bar{\mathbf{I}})\cdot(\mathbf{I}-\bar{\mathbf{I}})) = \left[\tau_J'(\bar{\mathbf{I}})\right] Cov(\mathbf{I}) \left[\tau_J'(\bar{\mathbf{I}})\right]^\intercal. \tag{A.7}$$

The identity in equation (A.6) also allows to simplify to some extent the $p \times p$ covariance matrices between $\tau_J'(\bar{\mathbf{I}})\cdot(\mathbf{I}-\bar{\mathbf{I}})$ and $e(\bar{\mathbf{I}}, \mathbf{I}-\bar{\mathbf{I}})$:

$$\begin{aligned}Cov(\tau_J'(\bar{\mathbf{I}})\cdot(\mathbf{I}-\bar{\mathbf{I}}), e(\bar{\mathbf{I}}, \mathbf{I}-\bar{\mathbf{I}})) = & \mathbb{E}_{\mathbf{I}\sim L(\mathbf{I};\boldsymbol{\alpha}^\star)}\left\{\left[\tau_J'(\bar{\mathbf{I}})\cdot(\mathbf{I}-\bar{\mathbf{I}})\right]\left[e(\bar{\mathbf{I}}, \mathbf{I}-\bar{\mathbf{I}}) - \mathbb{E}_{\mathbf{I}\sim L(\mathbf{I};\boldsymbol{\alpha}^\star)}\left\{e(\bar{\mathbf{I}}, \mathbf{I}-\bar{\mathbf{I}})\right\}\right]^\intercal\right\} \\ = & \mathbb{E}_{\mathbf{I}\sim L(\mathbf{I};\boldsymbol{\alpha}^\star)}\left\{\left[\tau_J'(\bar{\mathbf{I}})\cdot(\mathbf{I}-\bar{\mathbf{I}})\right] e^\intercal(\bar{\mathbf{I}}, \mathbf{I}-\bar{\mathbf{I}})\right\} \\ & - \mathbb{E}_{\mathbf{I}\sim L(\mathbf{I};\boldsymbol{\alpha}^\star)}\left\{\tau_J'(\bar{\mathbf{I}})\cdot(\mathbf{I}-\bar{\mathbf{I}})\right\}\mathbb{E}_{\mathbf{I}\sim L(\mathbf{I};\boldsymbol{\alpha}^\star)}\left\{e^\intercal(\bar{\mathbf{I}}, \mathbf{I}-\bar{\mathbf{I}})\right\} \\ = & \mathbb{E}_{\mathbf{I}\sim L(\mathbf{I};\boldsymbol{\alpha}^\star)}\left\{\left[\tau_J'(\bar{\mathbf{I}})\cdot(\mathbf{I}-\bar{\mathbf{I}})\right] e^\intercal(\bar{\mathbf{I}}, \mathbf{I}-\bar{\mathbf{I}})\right\},\end{aligned} \tag{A.8}$$

$$Cov(e(\bar{\mathbf{I}}, \mathbf{I}-\bar{\mathbf{I}}), \tau'_J(\bar{\mathbf{I}})\cdot(\mathbf{I}-\bar{\mathbf{I}})) = \left[Cov(\tau'_J(\bar{\mathbf{I}})\cdot(\mathbf{I}-\bar{\mathbf{I}}), e(\bar{\mathbf{I}}, \mathbf{I}-\bar{\mathbf{I}}))\right]^{\intercal}. \tag{A.9}$$

Before continuing on the demonstration of the bounds themselves, it is worth noting the following: since the focus of this work's section is to address the bias and variance of each individual component of the implicit estimator given by τ_J, we are not particularly interested in every component of the matrix $Cov(\tau_J(\mathbf{I}))$, but in its diagonal or, in other words, scalar forms of equation (A.5) resulting from projecting $\tau_J(\mathbf{I})$ onto the p-dimensional canonical vectors, *i.e.* $\tau_{J,j}(\mathbf{I}) = \langle \hat{\imath}_j, \tau_J(\mathbf{I})\rangle$ with $j \in \{1,\ldots,p\}$, where $\hat{\imath}_j$ denotes the canonical vector whose only non-zero component equals 1 at the j-th coordinate. Therefore, it can be readily held that, for $j \in \{1,\ldots,p\}$:

$$\begin{aligned}
\left[Var(\tau_J(\mathbf{I}))\right]_{(j,j)} =& \hat{\imath}_j^{\intercal} Var(\tau_J(\mathbf{I}))\hat{\imath}_j \\
=& Var(\langle \hat{\imath}_j, \tau_J(\mathbf{I})\rangle) \\
\approx& Var(\langle \hat{\imath}_j, \tau_J(\bar{\mathbf{I}}) + \tau'_J(\bar{\mathbf{I}})\cdot(\mathbf{I}-\bar{\mathbf{I}}) + e(\bar{\mathbf{I}}, \mathbf{I}-\bar{\mathbf{I}})\rangle) \\
=& Var\left(\tau_{J,j}(\bar{\mathbf{I}}) + \left[\tau'_J(\bar{\mathbf{I}})\right]_{(j,\cdot)}\cdot(\mathbf{I}-\bar{\mathbf{I}}) + e_j(\bar{\mathbf{I}}, \mathbf{I}-\bar{\mathbf{I}})\right) \\
=& Var\left(\left[\tau'_J(\bar{\mathbf{I}})\right]_{(j,\cdot)}\cdot(\mathbf{I}-\bar{\mathbf{I}}) + e_j(\bar{\mathbf{I}}, \mathbf{I}-\bar{\mathbf{I}})\right) \\
=& \left[\tau'_J(\bar{\mathbf{I}})\right]_{(j,\cdot)} Cov(\mathbf{I}) \left[\tau'_J(\bar{\mathbf{I}})\right]^{\intercal}_{(j,\cdot)} + Cov\left(\left[\tau'_J(\bar{\mathbf{I}})\right]_{(j,\cdot)}\cdot(\mathbf{I}-\bar{\mathbf{I}}), e_j(\bar{\mathbf{I}}, \mathbf{I}-\bar{\mathbf{I}})\right) \\
&+ Cov\left(e_j(\bar{\mathbf{I}}, \mathbf{I}-\bar{\mathbf{I}}), \left[\tau'_J(\bar{\mathbf{I}})\right]_{(j,\cdot)}\cdot(\mathbf{I}-\bar{\mathbf{I}})\right) + Var(e_j(\bar{\mathbf{I}}, \mathbf{I}-\bar{\mathbf{I}})) \\
=& \left[\tau'_J(\bar{\mathbf{I}})\right]_{(j,\cdot)} Cov(\mathbf{I}) \left[\tau'_J(\bar{\mathbf{I}})\right]^{\intercal}_{(j,\cdot)} + Var(e_j(\bar{\mathbf{I}}, \mathbf{I}-\bar{\mathbf{I}})) \\
&+ 2Cov\left(\left[\tau'_J(\bar{\mathbf{I}})\right]_{(j,\cdot)}\cdot(\mathbf{I}-\bar{\mathbf{I}}), e_j(\bar{\mathbf{I}}, \mathbf{I}-\bar{\mathbf{I}})\right).
\end{aligned} \tag{A.10}$$

Note that the last line in equation (A.10) follows from equation (A.9), or simply by properties of the scalar covariance operator.

A.1 Bias Bounds

From the projection of the estimator's Taylor expansion onto the direction of the canonical vector $\hat{\imath}_j$ depicted briefly in equation (A.10) it is possible to bound the magnitude of the bias with respect to the corresponding parameter $\alpha_j^{\star} = \langle \hat{\imath}_j, \boldsymbol{\alpha}^{\star}\rangle$ by applying the properties of the expectation operator and the triangle inequality,

$$
\begin{aligned}
\left|\mathbb{E}_{\mathbf{I}\sim L(\mathbf{I};\boldsymbol{\alpha}^\star)}\left\{\tau_{J,j}(\mathbf{I})\right\} - \alpha_j^\star\right| &\approx \left|\mathbb{E}_{\mathbf{I}\sim L(\mathbf{I};\boldsymbol{\alpha}^\star)}\left\{\tau_{J,j}(\bar{\mathbf{I}}) + \left[\tau'_J(\bar{\mathbf{I}})\right]_{(j,\cdot)} \cdot (\mathbf{I}-\bar{\mathbf{I}}) + e_j(\bar{\mathbf{I}}, \mathbf{I}-\bar{\mathbf{I}})\right\} - \alpha_j^\star\right| \\
&= \left|\tau_{J,j}(\bar{\mathbf{I}}) + \left[\tau'_J(\bar{\mathbf{I}})\right]_{(j,\cdot)} \cdot \mathbb{E}_{\mathbf{I}\sim L(\mathbf{I};\boldsymbol{\alpha}^\star)}\left\{(\mathbf{I}-\bar{\mathbf{I}})\right\} + \mathbb{E}_{\mathbf{I}\sim L(\mathbf{I};\boldsymbol{\alpha}^\star)}\left\{e_j(\bar{\mathbf{I}}, \mathbf{I}-\bar{\mathbf{I}})\right\} - \alpha_j^\star\right| \\
&= \left|\tau_{J,j}(\bar{\mathbf{I}}) + \mathbb{E}_{\mathbf{I}\sim L(\mathbf{I};\boldsymbol{\alpha}^\star)}\left\{e_j(\bar{\mathbf{I}}, \mathbf{I}-\bar{\mathbf{I}})\right\} - \alpha_j^\star\right| \\
&\leq \left|\tau_{J,j}(\bar{\mathbf{I}}) - \alpha_j^\star\right| + \left|\mathbb{E}_{\mathbf{I}\sim L(\mathbf{I};\boldsymbol{\alpha}^\star)}\left\{e_j(\bar{\mathbf{I}}, \mathbf{I}-\bar{\mathbf{I}})\right\}\right| \\
&\leq \left|\tau_{J,j}(\bar{\mathbf{I}}) - \alpha_j^\star\right| + \max_{t\in[0,1]}\left|\mathbb{E}_{\mathbf{I}\sim L(\mathbf{I};\boldsymbol{\alpha}^\star)}\left\{e_j(\bar{\mathbf{I}}, \mathbf{I}-\bar{\mathbf{I}})\right\}\right| \\
&\equiv \left|\tau_{J,j}(\bar{\mathbf{I}}) - \alpha_j^\star\right| + \varepsilon_{J,j},
\end{aligned}
\tag{A.11}
$$

which recovers the relation of equation (3.5).

A.2 Variance Bounds

The expression of equation (A.10) can be decomposed into two main elements:

$$
\begin{aligned}
Var(\tau_{J,j}(\mathbf{I})) &= \left[\tau'_J(\bar{\mathbf{I}})\right]_{(j,\cdot)} Cov(\mathbf{I}) \left[\tau'_J(\bar{\mathbf{I}})\right]^\intercal_{(j,\cdot)} + Var(e_j(\bar{\mathbf{I}}, \mathbf{I}-\bar{\mathbf{I}})) \\
&\quad + 2Cov\left(\left[\tau'_J(\bar{\mathbf{I}})\right]_{(j,\cdot)} \cdot (\mathbf{I}-\bar{\mathbf{I}}), e_j(\bar{\mathbf{I}}, \mathbf{I}-\bar{\mathbf{I}})\right) \\
&\equiv \left[\tau'_J(\bar{\mathbf{I}})\right]_{(j,\cdot)} Cov(\mathbf{I}) \left[\tau'_J(\bar{\mathbf{I}})\right]^\intercal_{(j,\cdot)} + \gamma_{J,j},
\end{aligned}
\tag{A.12}
$$

being $\gamma_{J,j}$ the critical term that shall allow us to find the interval depicted in equation (3.8). From this last equation and the reverse triangle inequality it follows that

$$
\begin{aligned}
Var(\tau_{J,j}(\mathbf{I})) &= \left[\tau'_J(\bar{\mathbf{I}})\right]_{(j,\cdot)} Cov(\mathbf{I}) \left[\tau'_J(\bar{\mathbf{I}})\right]^\intercal_{(j,\cdot)} + \gamma_{J,j} \\
\Rightarrow |\gamma_{J,j}| &= \left|Var(\tau_{J,j}(\mathbf{I})) - \left[\tau'_J(\bar{\mathbf{I}})\right]_{(j,\cdot)} Cov(\mathbf{I}) \left[\tau'_J(\bar{\mathbf{I}})\right]^\intercal_{(j,\cdot)}\right| \\
&\geq \left||Var(\tau_{J,j}(\mathbf{I}))| - \left|\left[\tau'_J(\bar{\mathbf{I}})\right]_{(j,\cdot)} Cov(\mathbf{I}) \left[\tau'_J(\bar{\mathbf{I}})\right]^\intercal_{(j,\cdot)}\right|\right| \\
&= \left|Var(\tau_{J,j}(\mathbf{I})) - \left[\tau'_J(\bar{\mathbf{I}})\right]_{(j,\cdot)} Cov(\mathbf{I}) \left[\tau'_J(\bar{\mathbf{I}})\right]^\intercal_{(j,\cdot)}\right| \\
\Rightarrow Var(\tau_{J,j}(\mathbf{I})) &\in \left[\left[\tau'_J(\bar{\mathbf{I}})\right]_{(j,\cdot)} Cov(\mathbf{I}) \left[\tau'_J(\bar{\mathbf{I}})\right]^\intercal_{(j,\cdot)} - |\gamma_{J,j}|, \left[\tau'_J(\bar{\mathbf{I}})\right]_{(j,\cdot)} Cov(\mathbf{I}) \left[\tau'_J(\bar{\mathbf{I}})\right]^\intercal_{(j,\cdot)} + |\gamma_{J,j}|\right].
\end{aligned}
\tag{A.13}
$$

Note that the line after the triangle inequality application comes from the non-negativity of $Var(\tau_{J,j}(\mathbf{I}))$ and $Cov(\mathbf{I})$ being a positive semidefinite matrix.

The interval shown in equation (A.13) resembles that of equation (3.8), but with one key difference: in Section 3 the bounding interval was stated in terms of $\beta_{J,j}$ from equation (3.7) instead of $\gamma_{J,j}$. In what follows it is proven that

$$|\gamma_{J,j}| \leq \beta_{J,j}. \tag{A.14}$$

Note that this inequality conveys looser bounds for $Var(\tau_{J,j}(\mathbf{I}))$, which comes from $\gamma_{J,j}$ being itself a function of the unknown variable $t \in [0,1]$ and by following similar steps of those proposed by [Espinosa et al., 2018].

For that matter, let's consider each one of the terms that define $\gamma_{J,j}$ independently. Firstly, we have that

$$\begin{aligned} Var(e_j(\bar{\mathbf{I}}, \mathbf{I}-\bar{\mathbf{I}})) &= \mathbb{E}_{\mathbf{I}\sim L(\mathbf{I};\boldsymbol{\alpha}^\star)}\left\{\left(e_j(\bar{\mathbf{I}}, \mathbf{I}-\bar{\mathbf{I}}) - \mathbb{E}_{\mathbf{I}\sim L(\mathbf{I};\boldsymbol{\alpha}^\star)}\left\{e_j(\bar{\mathbf{I}}, \mathbf{I}-\bar{\mathbf{I}})\right\}\right)^2\right\} \\ &\leq \mathbb{E}_{\mathbf{I}\sim L(\mathbf{I};\boldsymbol{\alpha}^\star)}\left\{\left(e_j(\bar{\mathbf{I}}, \mathbf{I}-\bar{\mathbf{I}})\right)^2\right\} \\ &\leq \max_{t\in[0,1]} \mathbb{E}_{\mathbf{I}\sim L(\mathbf{I};\boldsymbol{\alpha}^\star)}\left\{\left(e_j(\bar{\mathbf{I}}, \mathbf{I}-\bar{\mathbf{I}})\right)^2\right\}. \end{aligned} \tag{A.15}$$

On the other hand, by taking absolute value of the second term and considering again equations (A.6) and (A.8), we obtain that

$$\begin{aligned} \left|Cov\left(\left[\tau'_J(\bar{\mathbf{I}})\right]_{(j,\cdot)} \cdot (\mathbf{I}-\bar{\mathbf{I}}), e_j(\bar{\mathbf{I}}, \mathbf{I}-\bar{\mathbf{I}})\right)\right| &= \left|\mathbb{E}_{\mathbf{I}\sim L(\mathbf{I};\boldsymbol{\alpha}^\star)}\left\{\left[\left[\tau'_J(\bar{\mathbf{I}})\right]_{(j,\cdot)} \cdot (\mathbf{I}-\bar{\mathbf{I}})\right] e_j(\bar{\mathbf{I}}, \mathbf{I}-\bar{\mathbf{I}})\right\}\right| \\ &\leq \max_{t\in[0,1]} \left|\mathbb{E}_{\mathbf{I}\sim L(\mathbf{I};\boldsymbol{\alpha}^\star)}\left\{\left[\left[\tau'_J(\bar{\mathbf{I}})\right]_{(j,\cdot)} \cdot (\mathbf{I}-\bar{\mathbf{I}})\right] e_j(\bar{\mathbf{I}}, \mathbf{I}-\bar{\mathbf{I}})\right\}\right|. \end{aligned} \tag{A.16}$$

Finally, combining equations (A.15) and (A.16) both the desired bound and the definition for $\beta_{J,j}$ are recovered, concluding the demonstration.

$$\begin{aligned} |\gamma_{J,j}| &= \left|Var(e_j(\bar{\mathbf{I}}, \mathbf{I}-\bar{\mathbf{I}})) + 2Cov\left(\left[\tau'_J(\bar{\mathbf{I}})\right]_{(j,\cdot)} \cdot (\mathbf{I}-\bar{\mathbf{I}}), e_j(\bar{\mathbf{I}}, \mathbf{I}-\bar{\mathbf{I}})\right)\right| \\ &\leq \left|Var(e_j(\bar{\mathbf{I}}, \mathbf{I}-\bar{\mathbf{I}}))\right| + 2\left|Cov\left(\left[\tau'_J(\bar{\mathbf{I}})\right]_{(j,\cdot)} \cdot (\mathbf{I}-\bar{\mathbf{I}}), e_j(\bar{\mathbf{I}}, \mathbf{I}-\bar{\mathbf{I}})\right)\right| \\ &= Var(e_j(\bar{\mathbf{I}}, \mathbf{I}-\bar{\mathbf{I}})) + 2\left|Cov\left(\left[\tau'_J(\bar{\mathbf{I}})\right]_{(j,\cdot)} \cdot (\mathbf{I}-\bar{\mathbf{I}}), e_j(\bar{\mathbf{I}}, \mathbf{I}-\bar{\mathbf{I}})\right)\right| \\ &\leq \max_{t\in[0,1]} \mathbb{E}_{\mathbf{I}\sim L(\mathbf{I};\boldsymbol{\alpha}^\star)}\left\{\left(e_j(\bar{\mathbf{I}}, \mathbf{I}-\bar{\mathbf{I}})\right)^2\right\} + 2\max_{t\in[0,1]}\left|\mathbb{E}_{\mathbf{I}\sim L(\mathbf{I};\boldsymbol{\alpha}^\star)}\left\{\left[\left[\tau'_J(\bar{\mathbf{I}})\right]_{(j,\cdot)} \cdot (\mathbf{I}-\bar{\mathbf{I}})\right] e_j(\bar{\mathbf{I}}, \mathbf{I}-\bar{\mathbf{I}})\right\}\right| \\ &\equiv \beta_{J,j} \\ \Rightarrow Var(\tau_{J,j}(\mathbf{I})) &\in \left[\left[\tau'_J(\bar{\mathbf{I}})\right]_{(j,\cdot)} Cov(\mathbf{I}) \left[\tau'_J(\bar{\mathbf{I}})\right]^\intercal_{(j,\cdot)} - |\beta_{J,j}|, \left[\tau'_J(\bar{\mathbf{I}})\right]_{(j,\cdot)} Cov(\mathbf{I}) \left[\tau'_J(\bar{\mathbf{I}})\right]^\intercal_{(j,\cdot)} + |\beta_{J,j}|\right]. \end{aligned} \tag{A.17}$$

A.3 First- and Second-Order Derivatives for τ_J

The condition in equation (A.2) can be represented as a function $\Psi : \mathbb{R}^n \to \mathbb{R}^p$

$$\Psi(\mathbf{I}) = \begin{bmatrix} \frac{\partial}{\partial \alpha_1} J(\tau_J(\mathbf{I}), \mathbf{I}) \\ \vdots \\ \frac{\partial}{\partial \alpha_p} J(\tau_J(\mathbf{I}), \mathbf{I}) \end{bmatrix}, \tag{A.18}$$

whose zero is $\boldsymbol{\alpha} = \tau_J(\mathbf{I})$.

In order to find the Taylor expansion depicted in equations (3.3) and (3.4) one can draw upon the chain rule to take the partial derivative $\frac{\partial}{\partial I_i}$ on both sides of equation (A.2), resulting in one of the n sets of p equations on p unknowns of the form

$$\begin{aligned} \mathbf{0} &= \frac{\partial}{\partial I_i} \Psi(\mathbf{I}) \\ &= \begin{bmatrix} \sum_{k=1}^{p} \frac{\partial^2}{\partial \alpha_1 \partial \alpha_k} J(\tau_J(\mathbf{I}), \mathbf{I}) \cdot \frac{\partial}{\partial I_i} \tau_{J,k}(\mathbf{I}) + \frac{\partial^2}{\partial \alpha_1 \partial I_i} J(\tau_J(\mathbf{I}), \mathbf{I}) \\ \vdots \\ \sum_{k=1}^{p} \frac{\partial^2}{\partial \alpha_p \partial \alpha_k} J(\tau_J(\mathbf{I}), \mathbf{I}) \cdot \frac{\partial}{\partial I_i} \tau_{J,k}(\mathbf{I}) + \frac{\partial^2}{\partial \alpha_p \partial I_i} J(\tau_J(\mathbf{I}), \mathbf{I}) \end{bmatrix}. \end{aligned} \tag{A.19}$$

For ease of notation, this last expression can be rewritten in matrix form as follows

$$\begin{aligned} \mathbf{0} &= \begin{bmatrix} \frac{\partial^2}{\partial \alpha_1 \partial \alpha_1} J(\tau_J(\mathbf{I}), \mathbf{I}) & \dots & \frac{\partial^2}{\partial \alpha_1 \partial \alpha_p} J(\tau_J(\mathbf{I}), \mathbf{I}) \\ \vdots & \ddots & \vdots \\ \frac{\partial^2}{\partial \alpha_p \partial \alpha_1} J(\tau_J(\mathbf{I}), \mathbf{I}) & \dots & \frac{\partial^2}{\partial \alpha_p \partial \alpha_p} J(\tau_J(\mathbf{I}), \mathbf{I}) \end{bmatrix} \begin{bmatrix} \frac{\partial}{\partial I_i} \tau_{J,1}(\mathbf{I}) \\ \vdots \\ \frac{\partial}{\partial I_i} \tau_{J,p}(\mathbf{I}) \end{bmatrix} + \begin{bmatrix} \frac{\partial^2}{\partial \alpha_1 \partial I_i} J(\tau_J(\mathbf{I}), \mathbf{I}) \\ \vdots \\ \frac{\partial^2}{\partial \alpha_p \partial I_i} J(\tau_J(\mathbf{I}), \mathbf{I}) \end{bmatrix} \\ &= \left[\nabla^{20} J(\tau_J(\mathbf{I}), \mathbf{I})\right] \begin{bmatrix} \frac{\partial}{\partial I_i} \tau_{J,1}(\mathbf{I}) \\ \vdots \\ \frac{\partial}{\partial I_i} \tau_{J,p}(\mathbf{I}) \end{bmatrix} + \left[\nabla^{11} J(\tau_J(\mathbf{I}), \mathbf{I})\right]_{(\cdot,i)}. \end{aligned} \tag{A.20}$$

Noting that the total derivatives of Ψ and τ_J can be written, respectively, as

$$\Psi'(\mathbf{I}) = \begin{bmatrix} \frac{\partial}{\partial I_1}\Psi(\mathbf{I}) & \dots & \frac{\partial}{\partial I_n}\Psi(\mathbf{I}) \end{bmatrix} \in \mathbb{R}^{p\times n}, \tag{A.21}$$

$$\tau_J'(\mathbf{I}) = \begin{bmatrix} \frac{\partial}{\partial I_1}\tau_{J,1}(\mathbf{I}) & \dots & \frac{\partial}{\partial I_n}\tau_{J,1}(\mathbf{I}) \\ \vdots & \ddots & \vdots \\ \frac{\partial}{\partial I_1}\tau_{J,p}(\mathbf{I}) & \dots & \frac{\partial}{\partial I_n}\tau_{J,p}(\mathbf{I}) \end{bmatrix} \in \mathbb{R}^{p\times n}, \tag{A.22}$$

the n sets of linear systems depicted in equation (A.20) can be merged into[1]

$$\begin{aligned} \mathbf{0} &= \Psi'(\mathbf{I}) \\ &= \left[\nabla^{20}J(\tau_J(\mathbf{I}),\mathbf{I})\right] \begin{bmatrix} \frac{\partial}{\partial I_1}\tau_{J,1}(\mathbf{I}) & \dots & \frac{\partial}{\partial I_n}\tau_{J,1}(\mathbf{I}) \\ \vdots & \ddots & \vdots \\ \frac{\partial}{\partial I_1}\tau_{J,p}(\mathbf{I}) & \dots & \frac{\partial}{\partial I_n}\tau_{J,p}(\mathbf{I}) \end{bmatrix} + \left[\nabla^{11}J(\tau_J(\mathbf{I}),\mathbf{I})\right] \\ &= \left[\nabla^{20}J(\tau_J(\mathbf{I}),\mathbf{I})\right]\tau_J'(\mathbf{I}) + \left[\nabla^{11}J(\tau_J(\mathbf{I}),\mathbf{I})\right]. \end{aligned} \tag{A.23}$$

Finally, equation (3.11) is recovered, conditional on $\nabla^{20}J(\tau_J(\mathbf{I}),\mathbf{I})$ being an invertible matrix.

$$\tau_J'(\mathbf{I}) = -\left[\nabla^{20}J(\tau_J(\mathbf{I}),\mathbf{I})\right]^{-1}\left[\nabla^{11}J(\tau_J(\mathbf{I}),\mathbf{I})\right]. \tag{A.24}$$

Employing the chain rule once again to take the partial derivative $\frac{\partial}{\partial I_h}$ on both sides of equation (A.19) (more precisely on each one of the components of said equation), Fessler's equation (15) [Fessler, 1996] is recovered for each $j \in \{1,\dots,p\}$:

[1]Note the abuse of notation, where the left-hand side of equation (A.23) represents a $p \times n$ null matrix.

$$
\begin{aligned}
0 = &\sum_{k=1}^{p}\left[\left(\sum_{l=1}^{p}\left[\frac{\partial^3}{\partial\alpha_j\partial\alpha_k\partial\alpha_l}J(\tau_J(\mathbf{I}),\mathbf{I})\cdot\frac{\partial}{\partial I_h}\tau_{J,l}(\mathbf{I})\right]+\frac{\partial^3}{\partial\alpha_j\partial\alpha_k\partial I_h}J(\tau_J(\mathbf{I}),\mathbf{I})\right)\cdot\frac{\partial}{\partial I_i}\tau_{J,k}(\mathbf{I})\right] \\
&+\sum_{k=1}^{p}\left[\frac{\partial^2}{\partial\alpha_j\partial\alpha_k}J(\tau_J(\mathbf{I}),\mathbf{I})\cdot\frac{\partial^2}{\partial I_h\partial I_i}\tau_{J,k}(\mathbf{I})\right] \\
&+\sum_{k=1}^{p}\left[\frac{\partial^3}{\partial\alpha_j\partial\alpha_k\partial I_i}J(\tau_J(\mathbf{I}),\mathbf{I})\cdot\frac{\partial}{\partial I_h}\tau_{J,k}(\mathbf{I})\right]+\frac{\partial^3}{\partial\alpha_j\partial I_h\partial I_i}J(\tau_J(\mathbf{I}),\mathbf{I}).
\end{aligned}
\tag{A.25}
$$

Let us then denote the following

$$
P_{J,j}^{i,h}(\mathbf{I}) = \sum_{k=1}^{p}\left[\left(\sum_{l=1}^{p}\left[\frac{\partial^3}{\partial\alpha_j\partial\alpha_k\partial\alpha_l}J(\tau_J(\mathbf{I}),\mathbf{I})\cdot\frac{\partial}{\partial I_h}\tau_{J,l}(\mathbf{I})\right]+\frac{\partial^3}{\partial\alpha_j\partial\alpha_k\partial I_h}J(\tau_J(\mathbf{I}),\mathbf{I})\right)\cdot\frac{\partial}{\partial I_i}\tau_{J,k}(\mathbf{I})\right],
\tag{A.26}
$$

$$
Q_{J,j}^{i,h}(\mathbf{I}) = \sum_{k=1}^{p}\left[\frac{\partial^3}{\partial\alpha_j\partial\alpha_k\partial I_i}J(\tau_J(\mathbf{I}),\mathbf{I})\cdot\frac{\partial}{\partial I_h}\tau_{J,k}(\mathbf{I})\right]+\frac{\partial^3}{\partial\alpha_j\partial I_h\partial I_i}J(\tau_J(\mathbf{I}),\mathbf{I}).
\tag{A.27}
$$

Therefore, equation (A.25) can be rewritten as

$$
\begin{aligned}
0 &= P_{J,j}^{i,h}(\mathbf{I})+\sum_{k=1}^{p}\left[\frac{\partial^2}{\partial\alpha_j\partial\alpha_k}J(\tau_J(\mathbf{I}),\mathbf{I})\cdot\frac{\partial^2}{\partial I_h\partial I_i}\tau_{J,k}(\mathbf{I})\right]+Q_{J,j}^{i,h}(\mathbf{I}) \\
&= P_{J,j}^{i,h}(\mathbf{I})+\left[\nabla^{20}J(\tau_J(\mathbf{I}),\mathbf{I})\right]_{(j,\cdot)}\cdot\left[\frac{\partial^2}{\partial I_i\partial I_h}\tau_{J,1}(\mathbf{I})\quad\dots\quad\frac{\partial^2}{\partial I_i\partial I_h}\tau_{J,p}(\mathbf{I})\right]^{\intercal}+Q_{J,j}^{i,h}(\mathbf{I}) \\
&= P_{J,j}^{i,h}(\mathbf{I})+\left[\nabla^{20}J(\tau_J(\mathbf{I}),\mathbf{I})\right]_{(j,\cdot)}\cdot\frac{\partial^2}{\partial I_i\partial I_h}\tau_J(\mathbf{I})+Q_{J,j}^{i,h}(\mathbf{I}).
\end{aligned}
\tag{A.28}
$$

Written in that form, we can stack the p equations and get the matrix form that allows to find equation (3.13):

$$
\begin{aligned}
\mathbf{0} &= \begin{bmatrix} P^{i,h}_{J,1}(\mathbf{I}) \\ \vdots \\ P^{i,h}_{J,p}(\mathbf{I}) \end{bmatrix} + \begin{bmatrix} [\nabla^{20} J(\tau_J(\mathbf{I}), \mathbf{I})]_{(1,\cdot)} \\ \vdots \\ [\nabla^{20} J(\tau_J(\mathbf{I}), \mathbf{I})]_{(p,\cdot)} \end{bmatrix} \cdot \frac{\partial^2}{\partial I_i \partial I_h} \tau_J(\mathbf{I}) + \begin{bmatrix} Q^{i,h}_{J,1}(\mathbf{I}) \\ \vdots \\ Q^{i,h}_{J,p}(\mathbf{I}) \end{bmatrix} \\
&\equiv P^{i,h}_J(\mathbf{I}) + \nabla^{20} J(\tau_J(\mathbf{I}), \mathbf{I}) \cdot \frac{\partial^2}{\partial I_i \partial I_h} \tau_J(\mathbf{I}) + Q^{i,h}_J(\mathbf{I}) \\
\Rightarrow \frac{\partial^2}{\partial I_i \partial I_h} \tau_J(\mathbf{I}) &= - \left[\nabla^{20} J(\tau_J(\mathbf{I}), \mathbf{I})\right]^{-1} \left[P^{i,h}_J(\mathbf{I}) + Q^{i,h}_J(\mathbf{I})\right].
\end{aligned}
\tag{A.29}
$$

In order to complete the demonstration, it suffices to describe $P^{i,h}(\mathbf{I})$ and $Q^{i,h}(\mathbf{I})$ as in equations (3.14) and (3.15), respectively. For that matter it serves to treat said vectors' individual components, depicted in equations (A.26) and (A.27). Let's take then the latter, which can be easily rewritten as:

$$
\begin{aligned}
Q^{i,h}_{J,j}(\mathbf{I}) &= \sum_{k=1}^{p} \left[\frac{\partial^3}{\partial \alpha_j \partial \alpha_k \partial I_i} J(\tau_J(\mathbf{I}), \mathbf{I}) \cdot \frac{\partial}{\partial I_h} \tau_{J,k}(\mathbf{I}) \right] + \frac{\partial^3}{\partial \alpha_j \partial I_h \partial I_i} J(\tau_J(\mathbf{I}), \mathbf{I}) \\
&= \begin{bmatrix} \frac{\partial^3}{\partial \alpha_j \partial \alpha_1 \partial I_i} J(\tau_J(\mathbf{I}), \mathbf{I}) & \dots & \frac{\partial^3}{\partial \alpha_j \partial \alpha_p \partial I_i} J(\tau_J(\mathbf{I}), \mathbf{I}) \end{bmatrix} \begin{bmatrix} \frac{\partial}{\partial I_h} \tau_{J,1}(\mathbf{I}) \\ \vdots \\ \frac{\partial}{\partial I_h} \tau_{J,p}(\mathbf{I}) \end{bmatrix} + \left[\nabla^{12} J(\tau_J(\mathbf{I}), \mathbf{I})\right]_{(j,i,h)} \\
&= \left[\nabla^{21} J(\tau_J(\mathbf{I}), \mathbf{I})\right]_{(j,\cdot,i)} \left[\tau'_J(\mathbf{I})\right]_{(\cdot,h)} + \left[\nabla^{12} J(\tau_J(\mathbf{I}), \mathbf{I})\right]_{(j,i,h)}.
\end{aligned}
\tag{A.30}
$$

Following similar steps, *i.e.* identifying matrix forms, operations and considering the notation introduced by (3.9), equation (3.14) can be recovered:

$$
\begin{aligned}
P^{i,h}_{J,j}(\mathbf{I}) =& \sum_{k=1}^{p}\left[\left(\sum_{l=1}^{p}\left[\frac{\partial^3}{\partial\alpha_j\partial\alpha_k\partial\alpha_l}J(\tau_J(\mathbf{I}),\mathbf{I})\cdot\frac{\partial}{\partial I_h}\tau_{J,l}(\mathbf{I})\right]+\frac{\partial^3}{\partial\alpha_j\partial\alpha_k\partial I_h}J(\tau_J(\mathbf{I}),\mathbf{I})\right)\cdot\frac{\partial}{\partial I_i}\tau_{J,k}(\mathbf{I})\right] \\
=& \sum_{k=1}^{p}\left[\sum_{l=1}^{p}\left[\frac{\partial^3}{\partial\alpha_j\partial\alpha_k\partial\alpha_l}J(\tau_J(\mathbf{I}),\mathbf{I})\cdot\frac{\partial}{\partial I_h}\tau_{J,l}(\mathbf{I})\cdot\frac{\partial}{\partial I_i}\tau_{J,k}(\mathbf{I})\right]\right] \\
&+\sum_{k=1}^{p}\left[\frac{\partial^3}{\partial\alpha_j\partial\alpha_k\partial I_h}J(\tau_J(\mathbf{I}),\mathbf{I})\cdot\frac{\partial}{\partial I_i}\tau_{J,k}(\mathbf{I})\right] \\
=& \begin{bmatrix}\frac{\partial}{\partial I_i}\tau_{J,1}(\mathbf{I}) & \dots & \frac{\partial}{\partial I_i}\tau_{J,p}(\mathbf{I})\end{bmatrix}\begin{bmatrix}\frac{\partial^3}{\partial\alpha_j\partial\alpha_1\partial\alpha_1}J(\tau_J(\mathbf{I}),\mathbf{I}) & \cdots & \frac{\partial^3}{\partial\alpha_j\partial\alpha_1\partial\alpha_p}J(\tau_J(\mathbf{I}),\mathbf{I}) \\ \vdots & \ddots & \vdots \\ \frac{\partial^3}{\partial\alpha_j\partial\alpha_p\partial\alpha_1}J(\tau_J(\mathbf{I}),\mathbf{I}) & \cdots & \frac{\partial^3}{\partial\alpha_j\partial\alpha_p\partial\alpha_p}J(\tau_J(\mathbf{I}),\mathbf{I})\end{bmatrix}\begin{bmatrix}\frac{\partial}{\partial I_h}\tau_{J,1}(\mathbf{I}) \\ \vdots \\ \frac{\partial}{\partial I_h}\tau_{J,p}(\mathbf{I})\end{bmatrix} \\
&+\begin{bmatrix}\frac{\partial^3}{\partial\alpha_j\partial\alpha_1\partial I_h}J(\tau_J(\mathbf{I}),\mathbf{I}) & \dots & \frac{\partial^3}{\partial\alpha_j\partial\alpha_p\partial I_h}J(\tau_J(\mathbf{I}),\mathbf{I})\end{bmatrix}\begin{bmatrix}\frac{\partial}{\partial I_i}\tau_{J,1}(\mathbf{I}) \\ \vdots \\ \frac{\partial}{\partial I_i}\tau_{J,p}(\mathbf{I})\end{bmatrix} \\
=& \left[\tau'_J(\mathbf{I})\right]^{\intercal}_{(\cdot,i)}\left[\nabla^{30}J(\tau_J(\mathbf{I}),\mathbf{I})\right]_{(j,\cdot,\cdot)}\left[\tau'_J(\mathbf{I})\right]_{(\cdot,h)}+\left[\nabla^{21}J(\tau_J(\mathbf{I}),\mathbf{I})\right]_{(j,\cdot,h)}\left[\tau'_J(\mathbf{I})\right]_{(\cdot,i)},
\end{aligned}
\tag{A.31}
$$

which concludes the demonstration.

Annex B

Proof: Cramér-Rao Lower Bounds for the Joint Estimation Problem of Flux and Background

For ease of notation, since the source's relative position is assumed to be known and fixed we'll simply denote the likelihood function of equation (2.7) as $L(\mathbf{I}; \tilde{F}, \tilde{B})$. This is done solely to emphasize that $\tilde{F}$ and $\tilde{B}$ are the parameters of interest posed in this problem.

As stated in Theorem 2.1, the first necessary step to characterize the fundamental precision limits of the joint estimation problem is to check the regularity condition in equation (2.10) for each of the target parameters. This is verified as follows:

$$
\begin{aligned}
\mathbb{E}_{\mathbf{I}\sim L(\mathbf{I};\tilde{F},\tilde{B})}\left\{\frac{\partial}{\partial\tilde{F}}\ln L(\mathbf{I};\tilde{F},\tilde{B})\right\} &= \mathbb{E}_{\mathbf{I}\sim L(\mathbf{I};\tilde{F},\tilde{B})}\left\{\frac{\partial}{\partial\tilde{F}}\sum_{i\in\mathcal{J}} I_i \ln\lambda_i(x_c,\tilde{F}) - \lambda_i(x_c,\tilde{F}) - \ln I_i!\right\} \\
&= \mathbb{E}_{\mathbf{I}\sim L(\mathbf{I};\tilde{F},\tilde{B})}\left\{\sum_{i\in\mathcal{J}} I_i\frac{\partial}{\partial\tilde{F}}\ln\lambda_i(x_c,\tilde{F}) - \frac{\partial}{\partial\tilde{F}}\lambda_i(x_c,\tilde{F})\right\} \\
&= \mathbb{E}_{\mathbf{I}\sim L(\mathbf{I};\tilde{F},\tilde{B})}\left\{\sum_{i\in\mathcal{J}} I_i\frac{g_i(x_c)}{\lambda_i(x_c,\tilde{F})} - g_i(x_c)\right\} \\
&= \sum_{i\in\mathcal{J}} \mathbb{E}_{\mathbf{I}\sim L(\mathbf{I};\tilde{F},\tilde{B})}\left\{I_i\right\}\frac{g_i(x_c)}{\lambda_i(x_c,\tilde{F})} - g_i(x_c) \\
&= \sum_{i\in\mathcal{J}} \lambda_i(x_c,\tilde{F})\frac{g_i(x_c)}{\lambda_i(x_c,\tilde{F})} - g_i(x_c) \\
&= 0,
\end{aligned}
\tag{B.1}
$$

$$
\begin{aligned}
\mathbb{E}_{\mathbf{I}\sim L(\mathbf{I};\tilde{F},\tilde{B})}\left\{\frac{\partial}{\partial\tilde{B}}\ln L(\mathbf{I};\tilde{F},\tilde{B})\right\} &= \mathbb{E}_{\mathbf{I}\sim L(\mathbf{I};\tilde{F},\tilde{B})}\left\{\sum_{i\in\mathcal{J}} I_i\frac{\partial}{\partial\tilde{B}}\ln\lambda_i(x_c,\tilde{F}) - \frac{\partial}{\partial\tilde{B}}\lambda_i(x_c,\tilde{F})\right\}\\
&= \mathbb{E}_{\mathbf{I}\sim L(\mathbf{I};\tilde{F},\tilde{B})}\left\{\sum_{i\in\mathcal{J}} I_i\frac{1}{\lambda_i(x_c,\tilde{F})} - 1\right\}\\
&= \sum_{i\in\mathcal{J}}\mathbb{E}_{\mathbf{I}\sim L(\mathbf{I};\tilde{F},\tilde{B})}\left\{I_i\right\}\frac{1}{\lambda_i(x_c,\tilde{F})} - 1\\
&= \sum_{i\in\mathcal{J}}\lambda_i(x_c,\tilde{F})\frac{1}{\lambda_i(x_c,\tilde{F})} - 1\\
&= 0.
\end{aligned}
\tag{B.2}
$$

Therefore, the necessary conditions stated in Theorem 2.1 are satisfied. The second step is to find the Fisher Information Matrix by taking the negative of the expectation on the second derivatives, as in equation (2.12). In what follows, the different components of said matrix are calculated:

$$
\begin{aligned}
\mathcal{I}_{1,1} &\equiv \left[\mathcal{I}_{\boldsymbol{\theta}}\right]_{(1,1)}\\
&= -\mathbb{E}_{\mathbf{I}\sim L(\mathbf{I};\tilde{F},\tilde{B})}\left\{\frac{\partial^2}{\partial\tilde{F}^2}\ln L(\mathbf{I};\tilde{F},\tilde{B})\right\}\\
&= -\mathbb{E}_{\mathbf{I}\sim L(\mathbf{I};\tilde{F},\tilde{B})}\left\{\frac{\partial}{\partial\tilde{F}}\left(\sum_{i\in\mathcal{J}} I_i\frac{g_i(x_c)}{\lambda_i(x_c,\tilde{F})} - g_i(x_c)\right)\right\}\\
&= -\mathbb{E}_{\mathbf{I}\sim L(\mathbf{I};\tilde{F},\tilde{B})}\left\{\sum_{i\in\mathcal{J}} I_i g_i(x_c)\frac{\partial}{\partial\tilde{F}}\frac{1}{\lambda_i(x_c,\tilde{F})}\right\}\\
&= -\mathbb{E}_{\mathbf{I}\sim L(\mathbf{I};\tilde{F},\tilde{B})}\left\{\sum_{i\in\mathcal{J}} I_i g_i(x_c)\cdot\frac{-g_i(x_c)}{\lambda_i^2(x_c,\tilde{F})}\right\}\\
&= \sum_{i\in\mathcal{J}}\mathbb{E}_{\mathbf{I}\sim L(\mathbf{I};\tilde{F},\tilde{B})}\left\{I_i\right\}\frac{g_i^2(x_c)}{\lambda_i^2(x_c,\tilde{F})}\\
&= \sum_{i\in\mathcal{J}}\frac{g_i^2(x_c)}{\lambda_i(x_c,\tilde{F})},
\end{aligned}
\tag{B.3}
$$

$$
\begin{aligned}
\mathcal{I}_{2,1} &\equiv [\mathcal{I}_{\boldsymbol{\theta}}]_{(2,1)} \\
&= -\mathbb{E}_{\mathbf{I}\sim L(\mathbf{I};\tilde{F},\tilde{B})}\left\{\frac{\partial^2}{\partial\tilde{B}\partial\tilde{F}}\ln L(\mathbf{I};\tilde{F},\tilde{B})\right\} \\
&= -\mathbb{E}_{\mathbf{I}\sim L(\mathbf{I};\tilde{F},\tilde{B})}\left\{\frac{\partial}{\partial\tilde{B}}\left(\sum_{i\in\mathcal{J}} I_i\frac{g_i(x_c)}{\lambda_i(x_c,\tilde{F})} - g_i(x_c)\right)\right\} \\
&= -\mathbb{E}_{\mathbf{I}\sim L(\mathbf{I};\tilde{F},\tilde{B})}\left\{\sum_{i\in\mathcal{J}} I_i g_i(x_c)\frac{\partial}{\partial\tilde{B}}\frac{1}{\lambda_i(x_c,\tilde{F})}\right\} \\
&= -\mathbb{E}_{\mathbf{I}\sim L(\mathbf{I};\tilde{F},\tilde{B})}\left\{\sum_{i\in\mathcal{J}} I_i g_i(x_c)\cdot\frac{-1}{\lambda_i^2(x_c,\tilde{F})}\right\} \\
&= \sum_{i\in\mathcal{J}}\mathbb{E}_{\mathbf{I}\sim L(\mathbf{I};\tilde{F},\tilde{B})}\left\{I_i\right\}\frac{g_i(x_c)}{\lambda_i^2(x_c,\tilde{F})} \\
&= \sum_{i\in\mathcal{J}}\frac{g_i(x_c)}{\lambda_i(x_c,\tilde{F})},
\end{aligned}
\tag{B.4}
$$

$$
\begin{aligned}
\mathcal{I}_{1,2} &\equiv [\mathcal{I}_{\boldsymbol{\theta}}]_{(1,2)} \\
&= -\mathbb{E}_{\mathbf{I}\sim L(\mathbf{I};\tilde{F},\tilde{B})}\left\{\frac{\partial^2}{\partial\tilde{F}\partial\tilde{B}}\ln L(\mathbf{I};\tilde{F},\tilde{B})\right\} \\
&= -\mathbb{E}_{\mathbf{I}\sim L(\mathbf{I};\tilde{F},\tilde{B})}\left\{\frac{\partial}{\partial\tilde{F}}\left(\sum_{i\in\mathcal{J}} I_i\frac{1}{\lambda_i(x_c,\tilde{F})} - 1\right)\right\} \\
&= -\mathbb{E}_{\mathbf{I}\sim L(\mathbf{I};\tilde{F},\tilde{B})}\left\{\sum_{i\in\mathcal{J}} I_i\frac{\partial}{\partial\tilde{F}}\frac{1}{\lambda_i(x_c,\tilde{F})}\right\} \\
&= -\mathbb{E}_{\mathbf{I}\sim L(\mathbf{I};\tilde{F},\tilde{B})}\left\{\sum_{i\in\mathcal{J}} I_i\cdot\frac{-g_i(x_c)}{\lambda_i^2(x_c,\tilde{F})}\right\} \\
&= \sum_{i\in\mathcal{J}}\mathbb{E}_{\mathbf{I}\sim L(\mathbf{I};\tilde{F},\tilde{B})}\left\{I_i\right\}\frac{g_i(x_c)}{\lambda_i^2(x_c,\tilde{F})} \\
&= \sum_{i\in\mathcal{J}}\frac{g_i(x_c)}{\lambda_i(x_c,\tilde{F})},
\end{aligned}
\tag{B.5}
$$

$$
\begin{aligned}
\mathcal{I}_{2,2} &\equiv [\mathcal{I}_{\boldsymbol{\theta}}]_{(2,2)} \\
&= -\mathbb{E}_{\mathbf{I}\sim L(\mathbf{I};\tilde{F},\tilde{B})}\left\{\frac{\partial^2}{\partial \tilde{B}^2}\ln L(\mathbf{I};\tilde{F},\tilde{B})\right\} \\
&= -\mathbb{E}_{\mathbf{I}\sim L(\mathbf{I};\tilde{F},\tilde{B})}\left\{\frac{\partial}{\partial \tilde{B}}\left(\sum_{i\in\mathcal{J}} I_i \frac{1}{\lambda_i(x_c,\tilde{F})} - 1\right)\right\} \\
&= -\mathbb{E}_{\mathbf{I}\sim L(\mathbf{I};\tilde{F},\tilde{B})}\left\{\sum_{i\in\mathcal{J}} I_i \frac{\partial}{\partial \tilde{B}}\frac{1}{\lambda_i(x_c,\tilde{F})}\right\} \\
&= -\mathbb{E}_{\mathbf{I}\sim L(\mathbf{I};\tilde{F},\tilde{B})}\left\{\sum_{i\in\mathcal{J}} I_i \cdot \frac{-1}{\lambda_i^2(x_c,\tilde{F})}\right\} \\
&= \sum_{i\in\mathcal{J}} \mathbb{E}_{\mathbf{I}\sim L(\mathbf{I};\tilde{F},\tilde{B})}\left\{I_i\right\}\frac{1}{\lambda_i^2(x_c,\tilde{F})} \\
&= \sum_{i\in\mathcal{J}} \frac{1}{\lambda_i(x_c,\tilde{F})}.
\end{aligned}
\tag{B.6}
$$

These equations recover the Fisher Matrix of described in equation (4.12) and, as a consequence of Theorem 2.1, also imply the bounds of (4.13) and (4.14).

It is also worth noting, but not surprising, that the identity $\mathcal{I}_{1,2} = \mathcal{I}_{2,1}$ is verified, *i.e.* $\mathcal{I}_{\boldsymbol{\theta}}$ is symmetric.

Annex C

Proof: WLS Estimator for the Joint Estimation Problem of Flux and Background

As stated in Section 5, the Weighted Least-Squares (WLS) estimator for the posed joint estimation problem is the solution of an optimization problem

$$\tau_{WLS}(\mathbf{I}) = \underset{\boldsymbol{\alpha}\in\boldsymbol{\Theta}}{\operatorname{argmin}} J_{WLS}(\boldsymbol{\alpha}, \mathbf{I}), \tag{C.1}$$

where

$$J_{WLS}(\boldsymbol{\alpha}, \mathbf{I}) = \sum_{i\in\mathcal{J}} w_i (I_i - \alpha_1 \cdot g_i(x_c) - \alpha_2)^2, \tag{C.2}$$

and $\{w_i\}_{i\in\mathcal{J}}$ is a predefined set of weights. This estimator can be described in a closed (linear) form. In order to show that, it is first required to demonstrate the convexity of $J_{WLS}(\cdot)$ over $\boldsymbol{\Theta}$.

Let's consider then, for some fixed $\mathbf{I}$ and a real value $t \in [0, 1]$, two vectors on the parameter space $\boldsymbol{\alpha}_A = (\alpha_1, \alpha_2), \boldsymbol{\alpha}_B = (\alpha_1', \alpha_2') \in \boldsymbol{\Theta}$. Under this setup it follows that

$$
\begin{aligned}
J_{WLS}(t\boldsymbol{\alpha}_A + (1-t)\boldsymbol{\alpha}_B, \mathbf{I}) &= \sum_{i\in\mathcal{J}} w_i \left(I_i - (t\alpha_1 + (1-t)\alpha_1') \cdot g_i(x_c) - (t\alpha_2 + (1-t)\alpha_2')\right)^2 \\
&= \sum_{i\in\mathcal{J}} w_i \left(I_i - t(\alpha_1 \cdot g_{i(x_c)} + \alpha_2) - (1-t)(\alpha_1' \cdot g_{i(x_c)} + \alpha_2')\right)^2 \\
&= \sum_{i\in\mathcal{J}} w_i \left(t(I_i - \alpha_1 \cdot g_{i(x_c)} - \alpha_2) + (1-t)(I_i - \alpha_1' \cdot g_{i(x_c)} - \alpha_2')\right)^2 \\
&\leq \sum_{i\in\mathcal{J}} w_i \left(t\left(I_i - \alpha_1 \cdot g_{i(x_c)} - \alpha_2\right)^2 + (1-t)\left(I_i - \alpha_1' \cdot g_{i(x_c)} - \alpha_2'\right)^2\right) \\
&= t\sum_{i\in\mathcal{J}} w_i \left(I_i - \alpha_1 \cdot g_{i(x_c)} - \alpha_2\right)^2 + (1-t)\sum_{i\in\mathcal{J}} w_i \left(I_i - \alpha_1' \cdot g_{i(x_c)} - \alpha_2'\right)^2 \\
&= tJ_{WLS}(\boldsymbol{\alpha}_A, \mathbf{I}) + (1-t)J_{WLS}(\boldsymbol{\alpha}_B, \mathbf{I})\blacksquare
\end{aligned}
\tag{C.3}
$$

Since the cost function J_{WLS} is convex on $\boldsymbol{\Theta}$ given an observation vector $\mathbf{I}$, the same first order condition of equation (3.2) is assumed, from which the closed form of the estimator can be found, that is

$$\left.\begin{bmatrix} \frac{\partial}{\partial \alpha_1} J_{WLS}(\boldsymbol{\alpha}, \mathbf{I}) \\ \\ \frac{\partial}{\partial \alpha_2} J_{WLS}(\boldsymbol{\alpha}, \mathbf{I}) \end{bmatrix}\right|_{\boldsymbol{\alpha}=\tau_{WLS}(\mathbf{I})} = \mathbf{0}$$

$$\Rightarrow \left.\begin{bmatrix} -2\sum_{i\in\mathcal{J}} w_i g_i(x_c)\left(I_i - \alpha_1 g_i(x_c) - \alpha_2\right) \\ \\ -2\sum_{i\in\mathcal{J}} w_i \left(I_i - \alpha_1 g_i(x_c) - \alpha_2\right) \end{bmatrix}\right|_{\boldsymbol{\alpha}=\tau_{WLS}(\mathbf{I})} = \mathbf{0}$$

$$\Rightarrow \left.\begin{bmatrix} \sum_{i\in\mathcal{J}} w_i g_i(x_c)\left(\alpha_1 g_i(x_c) + \alpha_2\right) \\ \\ \sum_{i\in\mathcal{J}} w_i \left(\alpha_1 g_i(x_c) + \alpha_2\right) \end{bmatrix}\right|_{\boldsymbol{\alpha}=\tau_{WLS}(\mathbf{I})} = \begin{bmatrix} \sum_{i\in\mathcal{J}} w_i g_i(x_c) I_i \\ \\ \sum_{i\in\mathcal{J}} w_i I_i \end{bmatrix}$$

$$\Rightarrow \begin{bmatrix} w_{i_1} g_{i_1}(x_c) & \dots & w_{i_{|\mathcal{J}|}} g_{i_{|\mathcal{J}|}}(x_c) \\ \\ w_{i_1} & \dots & w_{i_{|\mathcal{J}|}} \end{bmatrix} \begin{bmatrix} g_{i_1}(x_c) & 1 \\ \\ \vdots & \vdots \\ \\ g_{i_{|\mathcal{J}|}}(x_c) & 1 \end{bmatrix} \left.\begin{bmatrix} \alpha_1 \\ \\ \alpha_2 \end{bmatrix}\right|_{\boldsymbol{\alpha}=\tau_{WLS}(\mathbf{I})} = \begin{bmatrix} \sum_{i\in\mathcal{J}} w_i g_i(x_c) I_i \\ \\ \sum_{i\in\mathcal{J}} w_i I_i \end{bmatrix}$$

$$\Rightarrow \begin{bmatrix} \sum_{i\in\mathcal{J}} w_i g_i^2(x_c) & \sum_{i\in\mathcal{J}} w_i g_i(x_c) \\ \\ \sum_{i\in\mathcal{J}} w_i g_i(x_c) & \sum_{i\in\mathcal{J}} w_i \end{bmatrix} \left.\begin{bmatrix} \alpha_1 \\ \\ \alpha_2 \end{bmatrix}\right|_{\boldsymbol{\alpha}=\tau_{WLS}(\mathbf{I})} = \begin{bmatrix} w_{i_1} g_{i_1}(x_c) & \dots & w_{i_{|\mathcal{J}|}} g_{i_{|\mathcal{J}|}}(x_c) \\ \\ w_{i_1} & \dots & w_{i_{|\mathcal{J}|}} \end{bmatrix} \cdot \begin{bmatrix} I_1 \\ \\ \vdots \\ \\ I_n \end{bmatrix}$$

$$\Rightarrow \begin{bmatrix} \sum_{i\in\mathcal{J}} w_i g_i^2(x_c) & \sum_{i\in\mathcal{J}} w_i g_i(x_c) \\ \\ \sum_{i\in\mathcal{J}} w_i g_i(x_c) & \sum_{i\in\mathcal{J}} w_i \end{bmatrix} \tau_{WLS}(\mathbf{I}) = \begin{bmatrix} w_{i_1} g_{i_1}(x_c) & \dots & w_{i_{|\mathcal{J}|}} g_{i_{|\mathcal{J}|}}(x_c) \\ \\ w_{i_1} & \dots & w_{i_{|\mathcal{J}|}} \end{bmatrix} \cdot \mathbf{I}. \tag{C.4}$$

Finally, assuming that the square matrix at the left-hand side of this equation is invertible, the estimator presented in Section 5 is recovered:

$$\tau_{WLS}(\mathbf{I}) = \begin{bmatrix} \sum_{i\in\mathcal{J}} w_i \cdot g_i^2(x_c) & \sum_{i\in\mathcal{J}} w_i \cdot g_i(x_c) \\ \sum_{i\in\mathcal{J}} w_i \cdot g_i(x_c) & \sum_{i\in\mathcal{J}} w_i \end{bmatrix}^{-1} \cdot \begin{bmatrix} w_{i_1} \cdot g_{i_1}(x_c) & \dots & w_{i_{|\mathcal{J}|}} \cdot g_{i_{|\mathcal{J}|}}(x_c) \\ w_{i_1} & \dots & w_{i_{|\mathcal{J}|}} \end{bmatrix} \cdot \mathbf{I}. \quad \text{(C.5)}$$

Note, however, that the matrix inverted in this last step is in fact invertible since it can be recognized that

$$\nabla^{20} J_{WLS}(\tau_{WLS}(\mathbf{I}), \mathbf{I}) = 2 \begin{bmatrix} \sum_{i\in\mathcal{J}} w_i \cdot g_i^2(x_c) & \sum_{i\in\mathcal{J}} w_i \cdot g_i(x_c) \\ \sum_{i\in\mathcal{J}} w_i \cdot g_i(x_c) & \sum_{i\in\mathcal{J}} w_i \end{bmatrix}, \quad \text{(C.6)}$$

and the invertibility of $\nabla^{20} J_{WLS}(\tau_{WLS}(\mathbf{I}), \mathbf{I})$ comes from $J_{WLS}(\cdot, \mathbf{I})$ being convex on $\boldsymbol{\Theta}$. Furthermore, it can also be recognized that

$$\nabla^{11} J_{WLS}(\tau_{WLS}(\mathbf{I}), \mathbf{I}) = -2 \begin{bmatrix} w_{i_1} \cdot g_{i_1}(x_c) & \dots & w_{i_{|\mathcal{J}|}} \cdot g_{i_{|\mathcal{J}|}}(x_c) \\ w_{i_1} & \dots & w_{i_{|\mathcal{J}|}} \end{bmatrix}. \quad \text{(C.7)}$$

Therefore, $\tau_{WLS}(\mathbf{I})$ can be noted just as in the second line of equation (5.3). Even more, from the linearity of the estimator and $-[\nabla^{20} J_{WLS}(\tau_{WLS}(\bar{\mathbf{I}}), \bar{\mathbf{I}})]^{-1} \cdot \nabla^{11} J_{WLS}(\tau_{WLS}(\bar{\mathbf{I}}), \bar{\mathbf{I}})$ being a constant matrix with respect to $\mathbf{I}$, $\tau_{WLS}(\mathbf{I})$ can be further reduced into

$$\tau_{WLS}(\mathbf{I}) = \tau'_{WLS}(\mathbf{I}) \cdot \mathbf{I}. \quad \text{(C.8)}$$

It may be interesting to note that the same form for $\tau_{WLS}(\cdot)$ can be found by means of the methodology of Section 3. Briefly put, it can be verified that the third-order derivatives that comprise $\nabla^{12} J_{WLS}(\boldsymbol{\alpha}, \mathbf{I})$, $\nabla^{21} J_{WLS}(\boldsymbol{\alpha}, \mathbf{I})$ and $\nabla^{30} J_{WLS}(\boldsymbol{\alpha}, \mathbf{I})$ are equal to zero, *i.e.* $\forall j,k,l \in \{1,2\}, \forall i,h \in \mathcal{J}$

$$\frac{\partial^3}{\partial\alpha_j \partial I_i \partial I_h} J_{WLS}(\boldsymbol{\alpha}, \mathbf{I}) = 0, \quad \frac{\partial^3}{\partial\alpha_j \partial\alpha_k \partial I_h} J_{WLS}(\boldsymbol{\alpha}, \mathbf{I}) = 0, \quad \frac{\partial^3}{\partial\alpha_j \partial\alpha_k \partial\alpha_l} J_{WLS}(\boldsymbol{\alpha}, \mathbf{I}) = 0, \quad \text{(C.9)}$$

which implies, from equations (3.13), (3.14) and (3.15) that $\tau''_{WLS}(\mathbf{I}) = \mathbf{0}$ and, consequently, $\mathbf{e}(\bar{\mathbf{I}}, \mathbf{I} - \bar{\mathbf{I}}) = \mathbf{0}$. On that account, the corresponding Taylor approximation around $\bar{\mathbf{I}}$ reduces to

$$\begin{aligned}\tau_{WLS}(\bar{\mathbf{I}}) + \tau'_{WLS}(\bar{\mathbf{I}}) \cdot (\mathbf{I} - \bar{\mathbf{I}}) &= \tau'_{WLS}(\bar{\mathbf{I}}) \cdot \mathbf{I} + \tau_{WLS}(\bar{\mathbf{I}}) - \tau'_{WLS}(\bar{\mathbf{I}}) \cdot \bar{\mathbf{I}} \\ &= \tau'_{WLS}(\bar{\mathbf{I}}) \cdot \mathbf{I} + \tau'_{WLS}(\bar{\mathbf{I}}) \cdot \bar{\mathbf{I}} - \tau'_{WLS}(\bar{\mathbf{I}}) \cdot \bar{\mathbf{I}} \\ &= \tau'_{WLS}(\bar{\mathbf{I}}) \cdot \mathbf{I} \\ &= \tau_{WLS}(\mathbf{I}).\end{aligned} \tag{C.10}$$

This equivalence between τ_{WLS} and its Taylor expansion is indeed evident from the linear nature of τ_{WLS}, but the importance of this analysis is to show some level of consistency between this particular case and the general estimator studied in Section 3.

For the sake of completeness, recalling that $\tau'_{WLS}(\mathbf{I}) = -[\nabla^{20} J_{WLS}(\tau_{WLS}(\mathbf{I}), \mathbf{I})]^{-1} \cdot \nabla^{11} J_{WLS}(\tau_{WLS}(\mathbf{I}), \mathbf{I})$ is a constant matrix given a set of weights $\{w_i\}_{i \in \mathcal{J}}$, we now show that the weight selection given by equation (5.10), *i.e.*

$$w_i = \frac{K}{\lambda_i(x_c, \tilde{F})}, \quad \forall i \in \{1, \ldots, n\}, \quad K > 0, \tag{C.11}$$

allows the WLS estimator to achieve optimality in the Cramér-Rao sense.

For that matter, it suffices to evaluate said weight set in $\tau'_{WLS}(\mathbf{I})$:

$$\begin{aligned}\tau'_{WLS}(\mathbf{I}) &= \frac{1}{K} \begin{bmatrix} \sum_{i \in \mathcal{J}} \frac{g_i^2(x_c)}{\lambda_i(x_c, \tilde{F})} & \sum_{i \in \mathcal{J}} \frac{g_i(x_c)}{\lambda_i(x_c, \tilde{F})} \\ \sum_{i \in \mathcal{J}} \frac{g_i(x_c)}{\lambda_i(x_c, \tilde{F})} & \sum_{i \in \mathcal{J}} \frac{1}{\lambda_i(x_c, \tilde{F})} \end{bmatrix}^{-1} \cdot K \begin{bmatrix} \frac{g_{i_1}(x_c)}{\lambda_{i_1}(x_c, \tilde{F})} & \cdots & \frac{g_{i_{|\mathcal{J}|}}(x_c)}{\lambda_{i_{|\mathcal{J}|}}(x_c, \tilde{F})} \\ \frac{1}{\lambda_{i_1}(x_c, \tilde{F})} & \cdots & \frac{1}{\lambda_{i_{|\mathcal{J}|}}(x_c, \tilde{F})} \end{bmatrix} \\ &= \mathcal{I}_{\boldsymbol{\alpha}^\star}^{-1} \cdot \begin{bmatrix} \frac{g_{i_1}(x_c)}{\lambda_{i_1}(x_c, \tilde{F})} & \cdots & \frac{g_{i_{|\mathcal{J}|}}(x_c)}{\lambda_{i_{|\mathcal{J}|}}(x_c, \tilde{F})} \\ \frac{1}{\lambda_{i_1}(x_c, \tilde{F})} & \cdots & \frac{1}{\lambda_{i_{|\mathcal{J}|}}(x_c, \tilde{F})} \end{bmatrix},\end{aligned} \tag{C.12}$$

where the structure of the estimation problem's Fisher matrix can be identified. Therefore,

$$
\begin{aligned}
Var(\tau_{WLS}(\mathbf{I})) &= \tau'_{WLS}(\mathbf{I}) \cdot Cov(\mathbf{I}) \cdot \tau'_{WLS}(\mathbf{I})^{\intercal} \\
&= \mathcal{I}_{\boldsymbol{\alpha}^\star}^{-1} \cdot \begin{bmatrix} \frac{g_{i_1}(x_c)}{\lambda_{i_1}(x_c,\tilde{F})} & \cdots & \frac{g_{i_{|\mathcal{J}|}}(x_c)}{\lambda_{i_{|\mathcal{J}|}}(x_c,\tilde{F})} \\ \\ \frac{1}{\lambda_{i_1}(x_c,\tilde{F})} & \cdots & \frac{1}{\lambda_{i_{|\mathcal{J}|}}(x_c,\tilde{F})} \end{bmatrix} \cdot Cov(\mathbf{I}) \cdot \begin{bmatrix} \frac{g_{i_1}(x_c)}{\lambda_{i_1}(x_c,\tilde{F})} & \frac{1}{\lambda_{i_1}(x_c,\tilde{F})} \\ \\ \vdots & \vdots \\ \\ \frac{g_{i_{|\mathcal{J}|}}(x_c)}{\lambda_{i_{|\mathcal{J}|}}(x_c,\tilde{F})} & \frac{1}{\lambda_{i_{|\mathcal{J}|}}(x_c,\tilde{F})} \end{bmatrix} \cdot \mathcal{I}_{\boldsymbol{\alpha}^\star}^{-1} \\
&= \mathcal{I}_{\boldsymbol{\alpha}^\star}^{-1} \cdot \begin{bmatrix} \frac{g_{i_1}(x_c)}{\lambda_{i_1}(x_c,\tilde{F})} & \cdots & \frac{g_{i_{|\mathcal{J}|}}(x_c)}{\lambda_{i_{|\mathcal{J}|}}(x_c,\tilde{F})} \\ \\ \frac{1}{\lambda_{i_1}(x_c,\tilde{F})} & \cdots & \frac{1}{\lambda_{i_{|\mathcal{J}|}}(x_c,\tilde{F})} \end{bmatrix} \cdot \begin{bmatrix} g_{i_1}(x_c) & 1 \\ \\ \vdots & \vdots \\ \\ g_{i_{|\mathcal{J}|}}(x_c) & 1 \end{bmatrix} \cdot \mathcal{I}_{\boldsymbol{\alpha}^\star}^{-1} \\
&= \mathcal{I}_{\boldsymbol{\alpha}^\star}^{-1} \cdot \begin{bmatrix} \sum_{i\in\mathcal{J}} \frac{g_i^2(x_c)}{\lambda_i(x_c,\tilde{F})} & \sum_{i\in\mathcal{J}} \frac{g_i(x_c)}{\lambda_i(x_c,\tilde{F})} \\ \\ \sum_{i\in\mathcal{J}} \frac{g_i(x_c)}{\lambda_i(x_c,\tilde{F})} & \sum_{i\in\mathcal{J}} \frac{1}{\lambda_i(x_c,\tilde{F})} \end{bmatrix} \cdot \mathcal{I}_{\boldsymbol{\alpha}^\star}^{-1} \\
&= \mathcal{I}_{\boldsymbol{\alpha}^\star}^{-1} \cdot \mathcal{I}_{\boldsymbol{\alpha}^\star} \cdot \mathcal{I}_{\boldsymbol{\alpha}^\star}^{-1} \\
&= \mathcal{I}_{\boldsymbol{\alpha}^\star}^{-1},
\end{aligned}
\tag{C.13}
$$

which concludes the result. However, it is worth noting again that this estimator's configuration requires to know $\boldsymbol{\alpha}^\star$ beforehand, which contradicts the aim and very essence of the posed problem.

Annex D

Proof: Theoretic Bounds for the SWLS Estimator in the Joint Estimation of Flux and Background

Let $\mathcal{J} \subseteq \{1, \ldots, n\}$ be a set of indices which defines a cost function given by

$$J_{SWLS}(\boldsymbol{\alpha}, \mathbf{I}) = \sum_{i \in \mathcal{J}} \frac{1}{I_i} (I_i - \alpha_1 \cdot g_i(x_c) - \alpha_2)^2, \tag{D.1}$$

where $\boldsymbol{\alpha} \in \boldsymbol{\Theta}$. Such function defines the so-called Stochastic Weighted Least-Squares (SWLS) estimator $\tau_{SWLS}(\mathbf{I})$ as an optimization problem just like equation (3.1), *i.e.*,

$$\tau_{SWLS}(\mathbf{I}) = \underset{\boldsymbol{\alpha} \in \boldsymbol{\Theta}}{\operatorname{argmin}} J_{SWLS}(\boldsymbol{\alpha}, \mathbf{I}). \tag{D.2}$$

Just as the general WLS estimator, the optimization problem posed in equation (D.2) has a closed-form, though non-linear on $\mathbf{I}$, solution; which can be readily[1] formulated as

$$\tau_{SWLS}(\mathbf{I}) = \begin{bmatrix} \sum_{i \in \mathcal{J}} \frac{1}{I_i} \cdot g_i^2(x_c) & \sum_{i \in \mathcal{J}} \frac{1}{I_i} \cdot g_i(x_c) \\ \sum_{i \in \mathcal{J}} \frac{1}{I_i} \cdot g_i(x_c) & \sum_{i \in \mathcal{J}} \frac{1}{I_i} \end{bmatrix}^{-1} \cdot \begin{bmatrix} \frac{1}{I_{i_1}} \cdot g_{i_1}(x_c) & \cdots & \frac{1}{I_{i_{|\mathcal{J}|}}} \cdot g_{i_{|\mathcal{J}|}}(x_c) \\ \frac{1}{I_{i_1}} & \cdots & \frac{1}{I_{i_{|\mathcal{J}|}}} \end{bmatrix} \cdot \mathbf{I}. \tag{D.3}$$

In order to evaluate the performance bounds developed in Section 3 for this particular formulation, let's consider firstly the derivatives of $J_{SWLS}(\boldsymbol{\alpha}, \mathbf{I})$ with respect to $\boldsymbol{\alpha}$, which define the

[1]Note that this new optimization problem is also convex on $\boldsymbol{\Theta}$, which can be easily demonstrated by simply replacing w_i with $\frac{1}{I_i}$ into equation (C.3). Such evaluation can be carried further into the derivation of the closed-form expression for the WLS estimator.

first-order condition of equation (3.2):

$$\frac{\partial}{\partial \alpha_1} J_{SWLS}(\boldsymbol{\alpha}, \mathbf{I}) = \sum_{i \in \mathcal{J}} \frac{-2 g_i(x_c)}{I_i} \left(I_i - \alpha_1 g_i(x_c) - \alpha_2 \right), \tag{D.4}$$

$$\frac{\partial}{\partial \alpha_2} J_{SWLS}(\boldsymbol{\alpha}, \mathbf{I}) = \sum_{i \in \mathcal{J}} \frac{-2}{I_i} \left(I_i - \alpha_1 g_i(x_c) - \alpha_2 \right). \tag{D.5}$$

Taking derivatives of these expressions with respect to $\boldsymbol{\alpha}$ and I_i for some $i \in \mathcal{J}$ leads into the elements of $\nabla^{20} J_{SWLS}(\boldsymbol{\alpha}, \mathbf{I})$ and $\nabla^{11} J_{SWLS}(\boldsymbol{\alpha}, \mathbf{I})$, respectively. The former second-order derivative corresponds to

$$\begin{aligned}
\nabla^{20} J_{SWLS}(\boldsymbol{\alpha}, \mathbf{I}) &= \begin{bmatrix} \frac{\partial^2}{\partial \alpha_1^2} J_{SWLS}(\boldsymbol{\alpha}, \mathbf{I}) & \frac{\partial^2}{\partial \alpha_1 \partial \alpha_2} J_{SWLS}(\boldsymbol{\alpha}, \mathbf{I}) \\ \frac{\partial^2}{\partial \alpha_2 \partial \alpha_1} J_{SWLS}(\boldsymbol{\alpha}, \mathbf{I}) & \frac{\partial^2}{\partial \alpha_2^2} J_{SWLS}(\boldsymbol{\alpha}, \mathbf{I}) \end{bmatrix} \\
&= \begin{bmatrix} \sum_{i \in \mathcal{J}} \frac{2 g_i^2(x_c)}{I_i} & \sum_{i \in \mathcal{J}} \frac{2 g_i(x_c)}{I_i} \\ \sum_{i \in \mathcal{J}} \frac{2 g_i(x_c)}{I_i} & \sum_{i \in \mathcal{J}} \frac{2}{I_i} \end{bmatrix} \\
&= 2 \begin{bmatrix} \sum_{i \in \mathcal{J}} \frac{g_i^2(x_c)}{I_i} & \sum_{i \in \mathcal{J}} \frac{g_i(x_c)}{I_i} \\ \sum_{i \in \mathcal{J}} \frac{g_i(x_c)}{I_i} & \sum_{i \in \mathcal{J}} \frac{1}{I_i} \end{bmatrix}.
\end{aligned} \tag{D.6}$$

From this last line, it stands out that $\nabla^{20} J_{SWLS}(\boldsymbol{\alpha}, \mathbf{I})$ and $\nabla^{20} J_{WLS}(\boldsymbol{\alpha}, \mathbf{I})$ (see equation (C.6)) share the same structure, which is evident by emphasizing the fact that the difference between both cost functions falls solely to the evaluation of $w_i = \frac{1}{I_i}$ for $i \in \mathcal{J}$.

However, what's more interesting is the fact that precisely this weight configuration conveys to (apparently) different structures after applying the ∇^{11} operator, as w_i is also derivable with respect to I_i, not just its adjacent squared-error term. Then,

$$\begin{aligned}
\frac{\partial^2}{\partial \alpha_1 \partial I_i} J_{SWLS}(\boldsymbol{\alpha}, \mathbf{I}) &= \frac{\partial}{\partial I_i} \left(\sum_{i \in \mathcal{J}} \frac{-2 g_i(x_c)}{I_i} \left(I_i - \alpha_1 g_i(x_c) - \alpha_2 \right) \right) \\
&= \frac{-2 g_i(x_c)}{I_i^2} \left(\alpha_1 g_i(x_c) + \alpha_2 \right),
\end{aligned} \tag{D.7}$$

$$\begin{aligned}\frac{\partial^2}{\partial\alpha_2\partial I_i}J_{SWLS}(\boldsymbol{\alpha},\mathbf{I}) &= \frac{\partial}{\partial I_i}\left(\sum_{i\in\mathcal{J}}\frac{-2}{I_i}\left(I_i-\alpha_1 g_i(x_c)-\alpha_2\right)\right)\\ &= \frac{-2}{I_i^2}\left(\alpha_1 g_i(x_c)+\alpha_2\right),\end{aligned} \tag{D.8}$$

$$\begin{aligned}\Rightarrow \nabla^{11}J_{SWLS}(\boldsymbol{\alpha},\mathbf{I}) &= \begin{bmatrix} \frac{\partial^2}{\partial\alpha_1\partial I_{i_1}}J_{SWLS}(\boldsymbol{\alpha},\mathbf{I}) & \cdots & \frac{\partial^2}{\partial\alpha_1\partial I_{i_{|\mathcal{J}|}}}J_{SWLS}(\boldsymbol{\alpha},\mathbf{I}) \\ \frac{\partial^2}{\partial\alpha_2\partial I_{i_1}}J_{SWLS}(\boldsymbol{\alpha},\mathbf{I}) & \cdots & \frac{\partial^2}{\partial\alpha_2\partial I_{i_{|\mathcal{J}|}}}J_{SWLS}(\boldsymbol{\alpha},\mathbf{I}) \end{bmatrix}\\ &= \begin{bmatrix} -\frac{2g_{i_1}(x_c)}{I_{i_1}^2}(\alpha_1 g_{i_1}(x_c)+\alpha_2) & \cdots & -\frac{2g_{i_{|\mathcal{J}|}}(x_c)}{I_{i_{|\mathcal{J}|}}^2}(\alpha_1 g_{i_{|\mathcal{J}|}}(x_c)+\alpha_2) \\ -\frac{2}{I_{i_1}^2}(\alpha_1 g_{i_1}(x_c)+\alpha_2) & \cdots & -\frac{2}{I_{i_{|\mathcal{J}|}}^2}(\alpha_1 g_{i_{|\mathcal{J}|}}(x_c)+\alpha_2) \end{bmatrix}.\end{aligned} \tag{D.9}$$

At first glance, it may appear that the expressions for $\nabla^{11}J_{SWLS}(\boldsymbol{\alpha},\mathbf{I})$ and $\nabla^{11}J_{WLS}(\boldsymbol{\alpha},\mathbf{I})$ (see equation (C.7), for example) do not share much of a structure in common, there's however a regimen where both equations become similar under the assumption that the SWLS estimator achieves zero error when evaluated at $\bar{\mathbf{I}}$ and the standard WLS estimator is equipped with the optimal set of weights (see Appendix C), that is $\tau_{SWLS}(\bar{\mathbf{I}}) = \boldsymbol{\alpha}^{\star 2}$ and $w_i = \frac{1}{\lambda_i(x_c,\tilde{F})}$. Under such circumstances it follows that:

[2]Which is in fact a consequence of the convexity of $J_{SWLS}(\cdot,\mathbf{I})$ over $\boldsymbol{\Theta}$ when fixing $\mathbf{I}=\bar{\mathbf{I}}$.

$$
\begin{aligned}
\nabla^{11} J_{SWLS}(\boldsymbol{\alpha}^\star, \bar{\mathbf{I}}) &= -2 \begin{bmatrix} \frac{g_{i_1}(x_c)}{\lambda^2_{i_1}(x_c,\tilde{F})} \left(\alpha_1^\star g_{i_1}(x_c) + \alpha_2^\star\right) & \dots & \frac{g_{i_{|\mathcal{J}|}}(x_c)}{\lambda^2_{i_{|\mathcal{J}|}}(x_c,\tilde{F})} \left(\alpha_1^\star g_{i_{|\mathcal{J}|}}(x_c) + \alpha_2^\star\right) \\ \frac{1}{\lambda^2_{i_1}(x_c,\tilde{F})} \left(\alpha_1^\star g_{i_1}(x_c) + \alpha_2^\star\right) & \dots & \frac{1}{\lambda^2_{i_{|\mathcal{J}|}}(x_c,\tilde{F})} \left(\alpha_1^\star g_{i_{|\mathcal{J}|}}(x_c) + \alpha_2^\star\right) \end{bmatrix} \\
&= -2 \begin{bmatrix} \frac{g_{i_1}(x_c)}{\lambda^2_{i_1}(x_c,\tilde{F})} \lambda_{i_1}(x_c,\tilde{F}) & \dots & \frac{g_{i_{|\mathcal{J}|}}(x_c)}{\lambda^2_{i_{|\mathcal{J}|}}(x_c,\tilde{F})} \lambda_{i_{|\mathcal{J}|}}(x_c,\tilde{F}) \\ \frac{1}{\lambda^2_{i_1}(x_c,\tilde{F})} \lambda_{i_1}(x_c,\tilde{F}) & \dots & \frac{1}{\lambda^2_{i_{|\mathcal{J}|}}(x_c,\tilde{F})} \lambda_{i_{|\mathcal{J}|}}(x_c,\tilde{F}) \end{bmatrix} \\
&= -2 \begin{bmatrix} \frac{g_{i_1}(x_c)}{\lambda_{i_1}(x_c,\tilde{F})} & \dots & \frac{g_{i_{|\mathcal{J}|}}(x_c)}{\lambda_{i_{|\mathcal{J}|}}(x_c,\tilde{F})} \\ \frac{1}{\lambda_{i_1}(x_c,\tilde{F})} & \dots & \frac{1}{\lambda_{i_{|\mathcal{J}|}}(x_c,\tilde{F})} \end{bmatrix} \\
&= -2 \begin{bmatrix} w_{i_1} \cdot g_{i_1}(x_c) & \dots & w_{i_{|\mathcal{J}|}} \cdot g_{i_{|\mathcal{J}|}}(x_c) \\ w_{i_1} & \dots & w_{i_{|\mathcal{J}|}} \end{bmatrix} \\
&= \nabla^{11} J_{WLS}(\cdot, \bar{\mathbf{I}}).
\end{aligned}
\tag{D.10}
$$

Having the expressions for $\nabla^{11} J_{SWLS}(\boldsymbol{\alpha}, \mathbf{I})$ and $\nabla^{20} J_{SWLS}(\boldsymbol{\alpha}, \mathbf{I})$ at hand, the first-order derivative of the estimator, $\tau'_{SWLS}(\mathbf{I})$, can be straightforwarly computed just as depicted in equation (3.11):

$$
\tau'_{SWLS}(\mathbf{I}) = -\left[\nabla^{20} J_{SWLS}(\tau_{SWLS}(\mathbf{I}), \mathbf{I})\right]^{-1} \left[\nabla^{11} J_{SWLS}(\tau_{SWLS}(\mathbf{I}), \mathbf{I})\right]. \tag{D.11}
$$

The next step towards finding the bounds on the estimator's performance is to elaborate on the expressions for the third-order derivatives of $J_{SWLS}(\boldsymbol{\alpha}, \mathbf{I})$. On this task, the simplest of these arrays corresponds to the application of the ∇^{30} operator since it can be readily verified (from equation (D.6)) that, $\forall j, k, l \in \{1, 2\}$, and for any pair $(\boldsymbol{\alpha}, \mathbf{I})$ on the parameter-observation space,

$$
\frac{\partial^3}{\partial \alpha_j \partial \alpha_k \partial \alpha_l} J_{SWLS}(\boldsymbol{\alpha}, \mathbf{I}) = 0. \tag{D.12}
$$

Therefore, the full $2 \times 2 \times 2$ array $\nabla^{30} J_{SWLS}(\boldsymbol{\alpha}, \mathbf{I})$ corresponds to a null-array, *i.e.*,

$$
\nabla^{30} J_{SWLS}(\boldsymbol{\alpha}, \mathbf{I}) = \mathbf{0}. \tag{D.13}
$$

Recalling on equations (D.7) and (D.8) we can develop on the applications of the ∇^{21} and ∇^{12} operators. For the former case, considering an arbitrary index $i \in \mathcal{J}$ we can take derivatives of said equations with respect to $\boldsymbol{\alpha}$, which leads to:

$$\begin{aligned}\frac{\partial^3}{\partial\alpha_1^2\partial I_i}J_{SWLS}(\boldsymbol{\alpha},\mathbf{I}) &= \frac{\partial}{\partial\alpha_1}\left(\frac{-2g_i(x_c)}{I_i^2}\left(\alpha_1 g_i(x_c)+\alpha_2\right)\right)\\ &= -\frac{2g_i^2(x_c)}{I_i^2},\end{aligned} \tag{D.14}$$

$$\begin{aligned}\frac{\partial}{\partial\alpha_1\partial\alpha_2\partial I_i}J_{SWLS}(\boldsymbol{\alpha},\mathbf{I}) = \frac{\partial}{\partial\alpha_2\partial\alpha_1\partial I_i}J_{SWLS}(\boldsymbol{\alpha},\mathbf{I}) &= \frac{\partial}{\partial\alpha_2}\left(\frac{-2g_i(x_c)}{I_i^2}\left(\alpha_1 g_i(x_c)+\alpha_2\right)\right)\\ &= -\frac{2g_i(x_c)}{I_i^2},\end{aligned} \tag{D.15}$$

$$\begin{aligned}\frac{\partial^3}{\partial\alpha_2^2\partial I_i}J_{SWLS}(\boldsymbol{\alpha},\mathbf{I}) &= \frac{\partial}{\partial\alpha_2}\left(\frac{-2}{I_i^2}\left(\alpha_1 g_i(x_c)+\alpha_2\right)\right)\\ &= -\frac{2}{I_i^2}.\end{aligned} \tag{D.16}$$

Combining these last three equations the full $2\times2\times|\mathcal{J}|$ array $\nabla^{21}J_{SWLS}(\boldsymbol{\alpha},\mathbf{I})$ can be summarized as

$$\left[\nabla^{21}J_{SWLS}(\boldsymbol{\alpha},\mathbf{I})\right]_{(\cdot,\cdot,i)} = \begin{bmatrix} -\frac{2g_i^2(x_c)}{I_i^2} & -\frac{2g_i(x_c)}{I_i^2} \\ -\frac{2g_i^2(x_c)}{I_i^2} & -\frac{2}{I_i^2} \end{bmatrix}. \tag{D.17}$$

On the other hand, taking derivatives of equations (D.7) and (D.8) with respect to some $I_h, h \in \mathcal{J}$ it follows that both respective expressions become case-dependent, in other words, both third-order derivatives take different values depending on whether $i = h$ or not. For that matter:

$$\frac{\partial^3}{\partial\alpha_1\partial I_i\partial I_h}J_{SWLS}(\boldsymbol{\alpha},\mathbf{I}) = \begin{cases}\frac{4g_i(x_c)}{I_i^3}\left(\alpha_1 g_i(x_c)+\alpha_2\right), & h=i\\ 0, & h\neq i\end{cases}, \tag{D.18}$$

$$\frac{\partial^3}{\partial\alpha_2\partial I_i\partial I_h}J_{SWLS}(\boldsymbol{\alpha},\mathbf{I}) = \begin{cases}\frac{4}{I_i^3}\left(\alpha_1 g_i(x_c)+\alpha_2\right), & h=i\\ 0, & h\neq i\end{cases}. \tag{D.19}$$

Consequently, the full $2 \times |\mathcal{J}| \times |\mathcal{J}|$ array $\nabla^{12} J_{SWLS}(\boldsymbol{\alpha}, \mathbf{I})$ can be interpreted as two $|\mathcal{J}| \times |\mathcal{J}|$ stacked diagonal matrices, which can be expressed, respectively, as follows:

$$\left[\nabla^{12} J_{SWLS}(\boldsymbol{\alpha}, \mathbf{I})\right]_{(1,\cdot,\cdot)} = \begin{bmatrix} \frac{4g_{i_1}(x_c)}{I_{i_1}^3}(\alpha_1 g_{i_1}(x_c) + \alpha_2) & & \\ & \ddots & \\ & & \frac{4g_{i_{|\mathcal{J}|}}(x_c)}{I_{i_{|\mathcal{J}|}}^3}(\alpha_1 g_{i_{|\mathcal{J}|}}(x_c) + \alpha_2) \end{bmatrix}, \tag{D.20}$$

$$\left[\nabla^{12} J_{SWLS}(\boldsymbol{\alpha}, \mathbf{I})\right]_{(2,\cdot,\cdot)} = \begin{bmatrix} \frac{4}{I_{i_1}^3}(\alpha_1 g_{i_1}(x_c) + \alpha_2) & & \\ & \ddots & \\ & & \frac{4}{I_{i_{|\mathcal{J}|}}^3}(\alpha_1 g_{i_{|\mathcal{J}|}}(x_c) + \alpha_2) \end{bmatrix}. \tag{D.21}$$

Finally, we can draw upon equations (3.14), (3.15) and (3.13) to ensemble the last building blocks to formulate the second-order derivatives of $\tau_{SWLS}(\mathbf{I})$ and to subsequently applying the bounds depicted in Section 3.

$$P_{SWLS}^{i,h}(\mathbf{I}) = \left[\left[\nabla^{21} J_{SWLS}(\tau_{SWLS}(\mathbf{I}), \mathbf{I})\right]_{(j,\cdot,h)} \left[\tau'_{SWLS}(\mathbf{I})\right]_{(\cdot,i)}\right]_{j=1}^{2}, \tag{D.22}$$

$$Q_{SWLS}^{i,h}(\mathbf{I}) = \left[\left[\nabla^{21} J_{SWLS}(\tau_{SWLS}(\mathbf{I}), \mathbf{I})\right]_{(j,\cdot,i)} \left[\tau'_{SWLS}(\mathbf{I})\right]_{(\cdot,h)} + \left[\nabla^{12} J_{SWLS}(\tau_{SWLS}(\mathbf{I}), \mathbf{I})\right]_{(j,i,h)}\right]_{j=1}^{2}, \tag{D.23}$$

$$\frac{\partial^2}{\partial I_i \partial I_h} \tau_{SWLS}(\mathbf{I}) = -\left[\nabla^{20} J_{SWLS}(\tau_{ML}(\mathbf{I}), \mathbf{I})\right]^{-1} \left[P_{SWLS}^{i,h}(\mathbf{I}) + Q_{SWLS}^{i,h}(\mathbf{I})\right]. \tag{D.24}$$

The expressions derived so far represent the cornerstone from which the performance bounds for the SWLS estimator are formulated and straightforward implemented, concluding the proof.

Annex E

Proof: Theoretic Bounds for the ML Estimator in the Joint Estimation of Flux and Background

As previously stated, the different derivatives required to bound both the bias and variance of the components of the estimator $\tau_{ML}(\mathbf{I})$ for the joint estimation of flux and background presented in equation (6.3) are here specified. Remind that, for some set of indices $\mathcal{J} \subseteq \{1, \ldots, n\}$, we define the cost function associated to the Maximum Likelihood (ML) estimator as

$$J_{ML}(\boldsymbol{\alpha}, \mathbf{I}) = \sum_{i \in \mathcal{J}} \alpha_1 \cdot g_i(x_c) + \alpha_2 - I_i \ln\left(\alpha_1 \cdot g_i(x_c) + \alpha_2\right), \tag{E.1}$$

where $\boldsymbol{\alpha} = (\alpha_1, \alpha_2) \in \boldsymbol{\Theta}$. Such function implicitly defines $\tau_{ML}(\mathbf{I})$ as an optimization problem just like equation (3.1), *i.e.*,

$$\tau_{ML}(\mathbf{I}) = \underset{\boldsymbol{\alpha} \in \boldsymbol{\Theta}}{\operatorname{argmin}} J_{ML}(\boldsymbol{\alpha}, \mathbf{I}). \tag{E.2}$$

In order to apply the methodology proposed in Section 3, we must show before that the ML functional has a unique optimal solution. To do so, we study its convexity. Let $\boldsymbol{\alpha}_A = (\alpha_1, \alpha_2), \boldsymbol{\alpha}_B = (\alpha_1', \alpha_2') \in \boldsymbol{\Theta}$ two vectors on the parameter space and $t \in [0, 1]$. For some fixed observation vector $\mathbf{I}$ we have that

$$
\begin{aligned}
J_{ML}(t\boldsymbol{\alpha}_A + (1-t)\boldsymbol{\alpha}_B, \mathbf{I}) &= \sum_{i\in\mathcal{J}} (t\alpha_1 + (1-t)\alpha_1') \cdot g_i(x_c) + (t\alpha_2 + (1-t)\alpha_2') \\
&\qquad - I_i \ln\left((t\alpha_1 + (1-t)\alpha_1') \cdot g_i(x_c) + (t\alpha_2 + (1-t)\alpha_2')\right) \\
&= \sum_{i\in\mathcal{J}} t\left(\alpha_1 \cdot g_i(x_c) + \alpha_2\right) + (1-t)\left(\alpha_1' \cdot g_i(x_c) + \alpha_2'\right) \\
&\qquad - I_i \ln\left(t\left(\alpha_1 \cdot g_i(x_c) + \alpha_2\right) + (1-t)\left(\alpha_1' \cdot g_i(x_c) + \alpha_2'\right)\right) \\
&\leq \sum_{i\in\mathcal{J}} t\left(\alpha_1 \cdot g_i(x_c) + \alpha_2\right) + (1-t)\left(\alpha_1' \cdot g_i(x_c) + \alpha_2'\right) \\
&\qquad - I_i \left[t \ln\left(\alpha_1 \cdot g_i(x_c) + \alpha_2\right) + (1-t)\ln\left(\alpha_1' \cdot g_i(x_c) + \alpha_2'\right)\right] \qquad \text{(E.3)} \\
&= \sum_{i\in\mathcal{J}} t\left(\alpha_1 \cdot g_i(x_c) + \alpha_2 - I_i \ln\left(\alpha_1 \cdot g_i(x_c) + \alpha_2\right)\right) \\
&\qquad + (1-t)\left(\alpha_1' \cdot g_i(x_c) + \alpha_2' - I_i \ln\left(\alpha_1' \cdot g_i(x_c) + \alpha_2'\right)\right) \\
&= t \sum_{i\in\mathcal{J}} \alpha_1 \cdot g_i(x_c) + \alpha_2 - I_i \ln\left(\alpha_1 \cdot g_i(x_c) + \alpha_2\right) \\
&\quad + (1-t) \sum_{i\in\mathcal{J}} \alpha_1' \cdot g_i(x_c) + \alpha_2' - I_i \ln\left(\alpha_1' \cdot g_i(x_c) + \alpha_2'\right) \\
&= tJ_{ML}(\boldsymbol{\alpha}_A, \mathbf{I}) + (1-t)J_{ML}(\boldsymbol{\alpha}_B, \mathbf{I}) \blacksquare
\end{aligned}
$$

where the inequality appears as a consequence of the concavity of the natural logarithm.

Since $J_{ML}(\boldsymbol{\alpha}, \mathbf{I})$ is convex on $\boldsymbol{\Theta}$ when $\mathbf{I}$ is fixed, we can proceed with the formulation of the bounds.

As a starting point, let's consider firstly the derivatives of $J_{ML}(\boldsymbol{\alpha}, \mathbf{I})$ with respect to $\boldsymbol{\alpha}$, which define the first-order condition of equation (3.2):

$$
\frac{\partial}{\partial \alpha_1} J_{ML}(\boldsymbol{\alpha}, \mathbf{I}) = \sum_{i\in\mathcal{J}} g_i(x_c) - \frac{I_i g_i(x_c)}{\alpha_1 g_i(x_c) + \alpha_2}, \qquad \text{(E.4)}
$$

$$
\frac{\partial}{\partial \alpha_2} J_{ML}(\boldsymbol{\alpha}, \mathbf{I}) = \sum_{i\in\mathcal{J}} 1 - \frac{I_i}{\alpha_1 g_i(x_c) + \alpha_2}. \qquad \text{(E.5)}
$$

Taking derivatives of these expressions with respect to $\boldsymbol{\alpha}$ and I_i for some $i \in \mathcal{J}$ results in the elements of $\nabla^{20} J_{ML}(\boldsymbol{\alpha}, \mathbf{I})$ and $\nabla^{11} J_{ML}(\boldsymbol{\alpha}, \mathbf{I})$, respectively. For the former matrix that is

$$\nabla^{20} J_{ML}(\boldsymbol{\alpha}, \mathbf{I}) = \begin{bmatrix} \frac{\partial^2}{\partial \alpha_1^2} J_{ML}(\boldsymbol{\alpha}, \mathbf{I}) & \frac{\partial^2}{\partial \alpha_1 \partial \alpha_2} J_{ML}(\boldsymbol{\alpha}, \mathbf{I}) \\ \frac{\partial^2}{\partial \alpha_2 \partial \alpha_1} J_{ML}(\boldsymbol{\alpha}, \mathbf{I}) & \frac{\partial^2}{\partial \alpha_2^2} J_{ML}(\boldsymbol{\alpha}, \mathbf{I}) \end{bmatrix} = \begin{bmatrix} \sum_{i \in \mathcal{J}} \frac{I_i g_i^2(x_c)}{(\alpha_1 g_i(x_c) + \alpha_2)^2} & \sum_{i \in \mathcal{J}} \frac{I_i g_i(x_c)}{(\alpha_1 g_i(x_c) + \alpha_2)^2} \\ \sum_{i \in \mathcal{J}} \frac{I_i g_i(x_c)}{(\alpha_1 g_i(x_c) + \alpha_2)^2} & \sum_{i \in \mathcal{J}} \frac{I_i}{(\alpha_1 g_i(x_c) + \alpha_2)^2} \end{bmatrix}. \tag{E.6}$$

It may be interesting to note that $\nabla^{20} J_{ML}(\boldsymbol{\alpha}, \mathbf{I})$ heavily resembles the structure of the Fisher matrix depicted in equation (4.12), which is natural from the very definition of the Fisher Information Matrix and the Maximum Likelihood estimator.

On the other hand, the elements of the latter matrix $\nabla^{11} J_{ML}(\boldsymbol{\alpha}, \mathbf{I})$, take the following forms:

$$\frac{\partial^2}{\partial \alpha_1 \partial I_i} J_{ML}(\boldsymbol{\alpha}, \mathbf{I}) = \frac{-g_i(x_c)}{\alpha_1 g_i(x_c) + \alpha_2}, \tag{E.7}$$

$$\frac{\partial^2}{\partial \alpha_2 \partial I_i} J_{ML}(\boldsymbol{\alpha}, \mathbf{I}) = \frac{-1}{\alpha_1 g_i(x_c) + \alpha_2}, \tag{E.8}$$

where $i \in \mathcal{J}$. Therefore, applying the ∇^{11} operator on the ML cost function results in

$$\nabla^{11} J_{ML}(\boldsymbol{\alpha}, \mathbf{I}) = \begin{bmatrix} \frac{\partial^2}{\partial \alpha_1 \partial I_{i_1}} J_{ML}(\boldsymbol{\alpha}, \mathbf{I}) & \cdots & \frac{\partial^2}{\partial \alpha_1 \partial I_{i_{|\mathcal{J}|}}} J_{ML}(\boldsymbol{\alpha}, \mathbf{I}) \\ \frac{\partial^2}{\partial \alpha_2 \partial I_{i_1}} J_{ML}(\boldsymbol{\alpha}, \mathbf{I}) & \cdots & \frac{\partial^2}{\partial \alpha_2 \partial I_{i_{|\mathcal{J}|}}} J_{ML}(\boldsymbol{\alpha}, \mathbf{I}) \end{bmatrix} = \begin{bmatrix} \frac{-g_{i_1}(x_c)}{\alpha_1 g_{i_1}(x_c) + \alpha_2} & \cdots & \frac{-g_{i_{|\mathcal{J}|}}(x_c)}{\alpha_1 g_{i_{|\mathcal{J}|}}(x_c) + \alpha_2} \\ \frac{-1}{\alpha_1 g_{i_1}(x_c) + \alpha_2} & \cdots & \frac{-1}{\alpha_1 g_{i_{|\mathcal{J}|}}(x_c) + \alpha_2} \end{bmatrix}. \tag{E.9}$$

With both these matrices, the first-order derivative of $\tau_{ML}(\mathbf{I})$ is directly obtained from equation (3.11) as

$$\tau'_{ML}(\mathbf{I}) = -\left[\nabla^{20} J_{ML}(\tau_{ML}(\mathbf{I}), \mathbf{I})\right]^{-1} \left[\nabla^{11} J_{ML}(\tau_{ML}(\mathbf{I}), \mathbf{I})\right]. \tag{E.10}$$

In a similar fashion, the estimator's second-order derivative can be determined by means of evaluating equations (3.14), (3.15) and (3.13). In order to do so, it suffices to calculate the application of third-order operators ∇^{12}, ∇^{21} and ∇^{30} on $J_{ML}(\boldsymbol{\alpha}, \mathbf{I})$ and then evaluating the resulting expressions on $\boldsymbol{\alpha} = \tau_{ML}(\mathbf{I})$.

For that matter, let $i, h \in \mathcal{J}$ be two indices, not necessarily distinct. Then:

$$\begin{aligned}\left[\nabla^{12} J_{ML}(\boldsymbol{\alpha}, \mathbf{I})\right]_{(1,h,i)} &= \frac{\partial}{\partial I_h}\left(\frac{\partial^2}{\partial \alpha_1 \partial I_i} J_{ML}(\boldsymbol{\alpha}, \mathbf{I})\right) \\ &= \frac{\partial}{\partial I_h}\left(\frac{-g_i(x_c)}{\alpha_1 g_i(x_c) + \alpha_2}\right) \\ &= 0,\end{aligned} \tag{E.11}$$

$$\begin{aligned}\left[\nabla^{12} J_{ML}(\boldsymbol{\alpha}, \mathbf{I})\right]_{(2,h,i)} &= \frac{\partial}{\partial I_h}\left(\frac{\partial^2}{\partial \alpha_2 \partial I_i} J_{ML}(\boldsymbol{\alpha}, \mathbf{I})\right) \\ &= \frac{\partial}{\partial I_h}\left(\frac{-1}{\alpha_1 g_i(x_c) + \alpha_2}\right) \\ &= 0.\end{aligned} \tag{E.12}$$

Therefore,

$$\nabla^{12} J_{ML}(\boldsymbol{\alpha}, \mathbf{I}) = \mathbf{0}, \tag{E.13}$$

remarking once again the abuse of notation, where $\mathbf{0}$ denotes a null array.

On the other hand, the i-th "slice" of $\nabla^{21} J_{ML}(\boldsymbol{\alpha}, \mathbf{I})$ is readily calculated as

$$\begin{aligned}\left[\nabla^{21} J_{ML}(\boldsymbol{\alpha}, \mathbf{I})\right]_{(\cdot,\cdot,i)} &= \begin{bmatrix} \frac{\partial}{\partial I_i}\left(\frac{\partial^2}{\partial \alpha_1^2} J_{ML}(\boldsymbol{\alpha}, \mathbf{I})\right) & \frac{\partial}{\partial I_i}\left(\frac{\partial^2}{\partial \alpha_1 \partial \alpha_2} J_{ML}(\boldsymbol{\alpha}, \mathbf{I})\right) \\ \frac{\partial}{\partial I_i}\left(\frac{\partial^2}{\partial \alpha_2 \partial \alpha_1} J_{ML}(\boldsymbol{\alpha}, \mathbf{I})\right) & \frac{\partial}{\partial I_i}\left(\frac{\partial^2}{\partial \alpha_2^2} J_{ML}(\boldsymbol{\alpha}, \mathbf{I})\right) \end{bmatrix} \\ &= \begin{bmatrix} \frac{\partial}{\partial I_i}\left(\sum_{j \in \mathcal{J}} \frac{I_i g_i^2(x_c)}{(\alpha_1 g_i(x_c) + \alpha_2)^2}\right) & \frac{\partial}{\partial I_i}\left(\sum_{j \in \mathcal{J}} \frac{I_i g_i(x_c)}{(\alpha_1 g_i(x_c) + \alpha_2)^2}\right) \\ \frac{\partial}{\partial I_i}\left(\sum_{j \in \mathcal{J}} \frac{I_i g_i(x_c)}{(\alpha_1 g_i(x_c) + \alpha_2)^2}\right) & \frac{\partial}{\partial I_i}\left(\sum_{j \in \mathcal{J}} \frac{I_i}{(\alpha_1 g_i(x_c) + \alpha_2)^2}\right) \end{bmatrix} \\ &= \begin{bmatrix} \frac{g_i^2(x_c)}{(\alpha_1 g_i(x_c) + \alpha_2)^2} & \frac{g_i(x_c)}{(\alpha_1 g_i(x_c) + \alpha_2)^2} \\ \frac{g_i(x_c)}{(\alpha_1 g_i(x_c) + \alpha_2)^2} & \frac{1}{(\alpha_1 g_i(x_c) + \alpha_2)^2} \end{bmatrix}.\end{aligned} \tag{E.14}$$

Lastly, for $\nabla^{30} J_{ML}(\boldsymbol{\alpha}, \mathbf{I})$ it follows that:

$$\begin{aligned}
\left[\nabla^{30} J_{ML}(\boldsymbol{\alpha}, \mathbf{I})\right]_{(1,\cdot,\cdot)} &= \begin{bmatrix} \frac{\partial}{\partial \alpha_1}\left(\frac{\partial^2}{\partial \alpha_1^2} J_{ML}(\boldsymbol{\alpha}, \mathbf{I})\right) & \frac{\partial}{\partial \alpha_1}\left(\frac{\partial^2}{\partial \alpha_1 \partial \alpha_2} J_{ML}(\boldsymbol{\alpha}, \mathbf{I})\right) \\ \frac{\partial}{\partial \alpha_1}\left(\frac{\partial^2}{\partial \alpha_2 \partial \alpha_1} J_{ML}(\boldsymbol{\alpha}, \mathbf{I})\right) & \frac{\partial}{\partial \alpha_1}\left(\frac{\partial^2}{\partial \alpha_2^2} J_{ML}(\boldsymbol{\alpha}, \mathbf{I})\right) \end{bmatrix} \\
&= \begin{bmatrix} \frac{\partial}{\partial \alpha_1}\left(\sum_{j \in \mathcal{J}} \frac{I_i g_i^2(x_c)}{(\alpha_1 g_i(x_c) + \alpha_2)^2}\right) & \frac{\partial}{\partial \alpha_1}\left(\sum_{j \in \mathcal{J}} \frac{I_i g_i(x_c)}{(\alpha_1 g_i(x_c) + \alpha_2)^2}\right) \\ \frac{\partial}{\partial \alpha_1}\left(\sum_{j \in \mathcal{J}} \frac{I_i g_i(x_c)}{(\alpha_1 g_i(x_c) + \alpha_2)^2}\right) & \frac{\partial}{\partial \alpha_1}\left(\sum_{j \in \mathcal{J}} \frac{I_i}{(\alpha_1 g_i(x_c) + \alpha_2)^2}\right) \end{bmatrix} \\
&= \begin{bmatrix} \sum_{i \in \mathcal{J}} \frac{-2 I_i g_i^3(x_c)}{(\alpha_1 g_i(x_c) + \alpha_2)^3} & \sum_{i \in \mathcal{J}} \frac{-2 I_i g_i^2(x_c)}{(\alpha_1 g_i(x_c) + \alpha_2)^3} \\ \sum_{i \in \mathcal{J}} \frac{-2 I_i g_i^2(x_c)}{(\alpha_1 g_i(x_c) + \alpha_2)^3} & \sum_{i \in \mathcal{J}} \frac{-2 I_i g_i(x_c)}{(\alpha_1 g_i(x_c) + \alpha_2)^3} \end{bmatrix},
\end{aligned} \tag{E.15}$$

$$\begin{aligned}
\left[\nabla^{30} J_{ML}(\boldsymbol{\alpha}, \mathbf{I})\right]_{(2,\cdot,\cdot)} &= \begin{bmatrix} \frac{\partial}{\partial \alpha_2}\left(\frac{\partial^2}{\partial \alpha_1^2} J_{ML}(\boldsymbol{\alpha}, \mathbf{I})\right) & \frac{\partial}{\partial \alpha_2}\left(\frac{\partial^2}{\partial \alpha_1 \partial \alpha_2} J_{ML}(\boldsymbol{\alpha}, \mathbf{I})\right) \\ \frac{\partial}{\partial \alpha_2}\left(\frac{\partial^2}{\partial \alpha_2 \partial \alpha_1} J_{ML}(\boldsymbol{\alpha}, \mathbf{I})\right) & \frac{\partial}{\partial \alpha_2}\left(\frac{\partial^2}{\partial \alpha_2^2} J_{ML}(\boldsymbol{\alpha}, \mathbf{I})\right) \end{bmatrix} \\
&= \begin{bmatrix} \frac{\partial}{\partial \alpha_2}\left(\sum_{j \in \mathcal{J}} \frac{I_i g_i^2(x_c)}{(\alpha_1 g_i(x_c) + \alpha_2)^2}\right) & \frac{\partial}{\partial \alpha_2}\left(\sum_{j \in \mathcal{J}} \frac{I_i g_i(x_c)}{(\alpha_1 g_i(x_c) + \alpha_2)^2}\right) \\ \frac{\partial}{\partial \alpha_2}\left(\sum_{j \in \mathcal{J}} \frac{I_i g_i(x_c)}{(\alpha_1 g_i(x_c) + \alpha_2)^2}\right) & \frac{\partial}{\partial \alpha_2}\left(\sum_{j \in \mathcal{J}} \frac{I_i}{(\alpha_1 g_i(x_c) + \alpha_2)^2}\right) \end{bmatrix} \\
&= \begin{bmatrix} \sum_{i \in \mathcal{J}} \frac{-2 I_i g_i^2(x_c)}{(\alpha_1 g_i(x_c) + \alpha_2)^3} & \sum_{i \in \mathcal{J}} \frac{-2 I_i g_i(x_c)}{(\alpha_1 g_i(x_c) + \alpha_2)^3} \\ \sum_{i \in \mathcal{J}} \frac{-2 I_i g_i(x_c)}{(\alpha_1 g_i(x_c) + \alpha_2)^3} & \sum_{i \in \mathcal{J}} \frac{-2 I_i}{(\alpha_1 g_i(x_c) + \alpha_2)^3} \end{bmatrix}.
\end{aligned} \tag{E.16}$$

Having these three tensors at hand and considering the matrices previously calculated (*i.e.*, $\nabla^{20} J_{ML}(\tau_{ML}(\mathbf{I}), \mathbf{I})$ and $\tau'_{ML}(\mathbf{I})$), equations (3.14), (3.15) and (3.13) can be directly applied to, finally, get the second-order derivative $\tau''_{ML}(\mathbf{I})$. In other words:

$$P_{ML}^{i,h}(\mathbf{I}) = \left[[\tau'_{ML}(\mathbf{I})]^{\intercal}_{(\cdot,i)} \left[\nabla^{30} J_{ML}(\tau_{ML}(\mathbf{I}), \mathbf{I})\right]_{(j,\cdot,\cdot)} [\tau'_{ML}(\mathbf{I})]_{(\cdot,h)} + \left[\nabla^{21} J_{ML}(\tau_{ML}(\mathbf{I}), \mathbf{I})\right]_{(j,\cdot,h)} [\tau'_{ML}(\mathbf{I})]_{(\cdot,i)} \right]_{j=1}^{2}, \tag{E.17}$$

$$
\begin{aligned}
Q_{ML}^{i,h}(\mathbf{I}) &= \left[\left[\nabla^{21} J_{ML}(\tau_{ML}(\mathbf{I}), \mathbf{I}) \right]_{(j,\cdot,i)} \left[\tau'_{ML}(\mathbf{I}) \right]_{(\cdot,h)} + \left[\nabla^{12} J_{ML}(\tau_{ML}(\mathbf{I}), \mathbf{I}) \right]_{(j,i,h)} \right]_{j=1}^{2} \\
&= \left[\left[\nabla^{21} J_{ML}(\tau_{ML}(\mathbf{I}), \mathbf{I}) \right]_{(j,\cdot,i)} \left[\tau'_{ML}(\mathbf{I}) \right]_{(\cdot,h)} \right]_{j=1}^{2},
\end{aligned}
\tag{E.18}
$$

$$
\frac{\partial^2}{\partial I_i \partial I_h} \tau_{ML}(\mathbf{I}) = - \left[\nabla^{20} J_{ML}(\tau_{ML}(\mathbf{I}), \mathbf{I}) \right]^{-1} \left[P_{ML}^{i,h}(\mathbf{I}) + Q_{ML}^{i,h}(\mathbf{I}) \right]. \tag{E.19}
$$

The expressions derived so far represent the cornerstone from which the performance bounds for the ML estimator are formulated and straightforward implemented, concluding the proof.